DESIGN OF A RECONFIGURABLE METAMATERIAL WITH THE USE OF BAYESIAN OPTIMIZATION AND MACHINE LEARNING

Delft University of Technology

DESIGN OF A RECONFIGURABLE METAMATERIAL WITH THE USE OF BAYESIAN OPTIMIZATION AND MACHINE LEARNING

by

Szymon Jan KASPRZYK

Thesis

submitted in partial fulfilment of the requirements for the degree of

Master of Science

in the department of

Cognitive Robotics

at the Faculty of Mechanical, Maritime and Materials Engineering of
Delft University of Technology

to be defended publicly on Thursday December 17 2020 at 15:00

Thesis supervisor:
Dr. M.A. Bessa — Faculty 3mE, TU Delft

Thesis advisor:
Dr. M. Dias Castilho — TU Eindhoven/UMC Utrecht

Committee members:
Dr. M. Sluiter — Faculty 3mE, TU Delft
Dr. M. Wiertlewski — Faculty 3mE, TU Delft

Student Number: 4811836
Date: December 7, 2020

An electronic version of this dissertation is available at:
https://repository.tudelft.nl

At the very outset of this report I would like to express gratitude to my supervisor Miguel Bessa who made my final step of education at the Delft University of Technology so meaningful. I am incredibly grateful for the shared knowledge, words of encouragement and support at all times. Thank you for believing in me, introducing me into the world of machine learning and changing my view on this field of Science.

I would also like to thank Miguel Dias Castilho for all the effort put into this project and for eagerness to share and discuss ideas during our meetings. Your input gave a new purpose to this work and helped me learn about subjects I did not expect to encounter but ones I deeply enjoyed.

My sincere gratitude goes to my parents Joanna and Zygmunt who have always supported me and made my incredible international adventure possible. I would also like to appreciate my friends and everyone involved for their help and being patient with me throughout my studies.

ABSTRACT

Metamaterials are a relatively new group of materials whose behaviour strongly depends on the design of their internal structure. They can be employed in a wide range of applications, one of which is presented in this thesis. As cardiovascular diseases account for around 30% of deaths worldwide the research done in the field of Materials Science may find a real life use in the form of a magnetically activated heart assisting device. Such a structure was designed on the basis of a newly developed magnetostrictive material with the use of finite element simulations and machine learning based analyses.

The computational approach enabled the investigation of the structure's deformation and determination of the influence of parameters, which define the metamaterial's geometry, before commencing prototyping and experiments. Geometry, which resulted from multiple iterations necessary to match the heart's shape and deformation patterns, was parametrized and simulated in each configuration to create a database. Regression was performed on it with Artificial Neural Networks and Sparse Gaussian Process Regression in order to predict possible bounds and importance of specific parameters. At the subsequent stage the structure was optimized, with the aim of matching the deformation of a healthy myocardium, which concluded the project.

Obtained sections of the design space allowed for qualitative as well as quantitative description of the device's capabilities. It was established that most of the behaviour in all directions, longitudinal, radial and rotational, is determined by position of the main active element within the structure as well as its size and the size of vertical elements encompassing the myocardium. Optimization process confirmed the predictions and led to the first magnetically activated, metamaterial based design of a heart assisting device.

CONTENTS

1

INTRODUCTION

THIS thesis commenced as a continuation of work on a supercompressible metamaterial and was transformed into development of a heart assisting structure based on its geometry. The first design of such a device is proposed on the basis of analysis performed with finite element simulations and machine learning. The optimized geometrical configuration which can be magnetically activated shows potential to be a new remedy to myocardium sicknesses.

Cardiovascular diseases which hamper the heart's operation are a major issue which contributes to a significant percentage of deaths worldwide. Some of them can be treated either temporarily or continuously with heart - assisting devices. There is a significant number of these available on the market in the form of pulsatile and continuous flow appliances and a few novel ideas in research. Most of them, however, pose as an inconvenience to the patient due to the mode of activation which is transcutaneous. Additional threats of bleeding or infection are another disadvantages of currently utilized devices. The ones which minimize the cons are usually simple and do not offer enough tailorability to patients' needs. Also, few of them assist the heart in all directions of its motion - longitudinally, radially and rotationally. This creates a scope for design of a safe, reconfigurable structure, which closely follows the myocardial deformations and could aid people on their way to recovery.

The relatively new type of materials which prove to be suitable for such applications are called metamaterials. They are superior to the substances which they consist of due to the arrangement of their internal structure. One can represent them in cellular form or as a unit cell like the geometry described in this thesis. Manufacturing of such materials poses a challenge to typical manufacturing processes but is feasible with additive manufacturing techniques like 3D printing.

Discovery or design of new materials depends strongly on finding trends in their properties based on varied parameters like percentage of doping agents or attributes of microstructure. A similar approach is presented in this work but on a macroscale with the

use of machine learning. The novel design of the previously developed metamaterial is adjusted to the heart's shape, parametrized and analysed in thousands of configurations. Outcomes are regressed in a multidimensional space in order to derive trends defining influence of parameters on the quantities of interest. Finally, the geometry is optimized with respect to the set parameters and within bounds investigated in the data-driven analysis.

The thesis starts with description of available knowledge and determination of scope for improvement in the form of literature review presented in Chapter 2. Description of the framework used along with the results of the data-driven analysis follow right after in Chapter 3. Bayesian optimization module as well as the optimization results are presented in Chapter 4. Conclusions regarding the outcomes and recommendations for development of the project appear in Chapter 5.

2

LITERATURE REVIEW

THE research conducted for this thesis required not only computational analysis but also a relevant theoretical preparation based on previous work done in this field. The literature review done as a part of it starts with Section 2.1 which identifies the potential improvement in the field of heart assisting devices and lays out the motivation behind this project. Section 2.2 is a summary of currently available metamaterials, explanation of what they are, their classification and reasons behind choosing them for the given application. Section 2.3 provides information about substances considered as potentially useful in making the metamaterial active. The last Section 2.4 gives a brief overview of the utilized computational methods from the field of machine learning.

2.1. MOTIVATION

World Health Organisation classifies the cardiovascular diseases (CVD) as the main cause of death as around 31 % of all deaths globally in 2016 were due to CVDs [159]. Roth et al. describe CVDs as a significant obstruction to human development due to their prevalence and mortality [120]. Although patients' life expectancy and quality of life can be extended with medication [120], intervention with artificial appliances or a heart transplantation are often required. For these reasons the main motivation behind this project is the design of a novel heart assisting structure, which could reduce the issues inherent to currently available devices.

Cardiovascular diseases are illnesses of the heart muscle (coronary heart diseases) and blood vessels. They can be inborn (congenital diseases) or acquired [120]. Some illnesses cause the left ventricle to deform to a lesser extent like in the case of ischemic cardiomyopathy, therefore reducing the blood flow [21, 135]. Ischemic heart disease was the main CVD causing heart - related health issues globally between 1990 and 2015 [120]. Hence, the scope for patients' life improvement is the greatest if the right treatment technology, capable of restoring heart's pumping capacity, is developed.

2.1.1. HEART DEFORMATION AND VENTRICULAR ASSIST DEVICES

DESCRIPTION OF HEART'S MOTION

Healthy myocardium shortens and twists in a complicated manner due to the complex shape of the muscle tissue as described by Buckberg et al. [25] and visible in Figure 2.2. Such a muscle shape allows simultaneous compressive and twisting motions [25]. For the purpose of this project the motion is simplified into the global longitudinal strain (GLS), global radial strain (GRS), global circumferential strain (GCS) and a twist between the heart's base and apex [135, 165, 167] as shown in Figure 2.1.

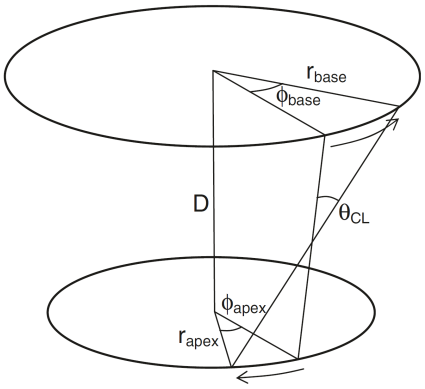

Figure 2.1: Heart's twisting motion [167]

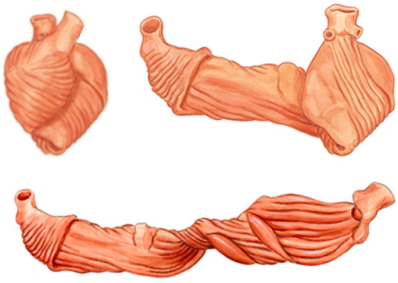

Figure 2.2: Torrent-Guasp's myocardium model adapted from [25]

Typical values for each of the strain components can be found in Table 2.1 and are well described in literature [106, 135, 165]. The twist is measured at the base of the heart with mean of 5.1° and at the apex with a mean of 11° as depicted in Figure 2.1 which in a simplified manner results in a total of $16 \pm 3°$ of rotation between the base and apex [25].

Table 2.1: Typical myocardium strain components [165]

Property	Minimum	Maximum
GLS [%]	15.9	22.1
GRS [%]	35.1	59.0
GCS [%]	20.9	27.8

SUMMARY OF VENTRICULAR ASSIST DEVICES

Currently the heart assist devices assume one of the two forms - pulsatile [40] or continuous flow appliances [126]. Positive displacement pumps used in the former ones cause a pulsating action alike the one of the heart itself, while the latter devices with centrifugal or axial flow pumps create a continuous blood flow through the heart [46, 88, 126]. The pulsatile ventricular assist devices can be used as a temporary therapy to ease the work of the heart and let it heal. The continuous - flow ones aimed at long - term use can be utilized in a destination therapy where it is used for the rest of patient's life or as a bridge to transplantation [18, 126].

Despite the benefit of saving human lives, the use of ventricular assist devices (VAD) always poses some risks to the patient, the most common of which are bleeding and infections [47, 126]. Additionally, the prolonged use of continuous flow devices can result in reduction of aortic wall thickness and appears to increase the risk of gastrointestinal bleeding. The pulsatile devices seem to be more useful in heart recuperation periods as their use preserves the pressure-volume curves better for the left ventricle [88]. The last but very crucial difference is the probability of survival which decreases more over time for the pulsatile VADs in comparison to the ones with continuous flow [88]. This shows that there is no perfect solution to the problem of a sick myocardium yet.

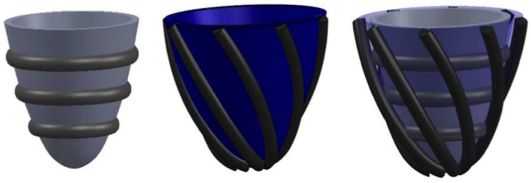

Figure 2.3: Pneumatic artificial muscle based VAD, designed by Roche et al. [118], with circular elements that induce circumferential and radial strain and diagonal ones which cause longitudinal contraction and rotation

Previous work done in this field in order to develop a superior technology without some of the described flaws includes the use of pneumatic artificial muscles (PAM) to create an active scaffolding for a device encapsulating the myocardium in a flexible sleeve (Figure 2.3) [118, 119]. Such a pneumatic material consists of an internal pliable bag which extends when pressurized and an external non-extensible mesh which shortens the structure when it expands sideways upon pressurization [29]. A significant benefit of the pneumatic actuation is the twofold behaviour of the artificial muscle - contraction at pressurization and expansion at the application of vacuum. This results in a more responsive activation mechanism of the VAD [118].

The device presented by Roche et al. [118] is capable of supporting longitudinal, twisting and circumferential motions of the myocardium simultaneously. The extent to which it reinforces heart's work can be adjusted with the pressure inside the PAMs. The soft sleeve used in the design allows for an adaptation of the device to the shape and mechanics of myocardial tissue and for a twist of up to around 11°. While it is hard to extract the exact

longitudinal strain from the latest work, the previous design [119] proved to be capable of around 16% strain in that direction.

Some of the other proposed solutions include passive [130] or active [149] Nitinol based devices which assist the heart by squeezing it in all directions. There are also designs which are focused on only one type of strain like the rotation inducing appliance developed by Trumble et al. [150] (Figure 2.4). Such a device was proven to leave no damage to the heart tissue as well as cause no arrhythmias even at rotations reaching 120° [150]. All of such external devices have a primary advantage of less interference with internal myocardial tissue, which in the case of standard VADs can cause clogging [130]. Shahinpoor [130] underlines the potential and need for general compression devices in heart disease treatment.

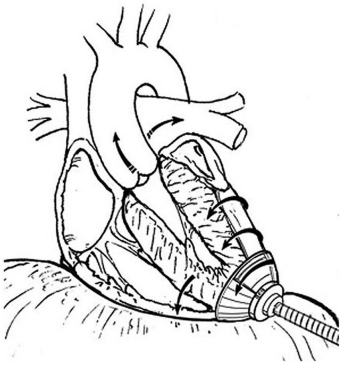

Figure 2.4: Visualisation of an apical torsional ventricular assist device whose operation is based solely on torsion of the myocardium [150]

Most of currently used and the recently proposed active solutions have a common disadvantage of requiring an electrical pump which needs to be powered either externally or has a limited operation time on battery. Some of the Nitinol based devices also require transcutaneous wires [149]. Removal of such from the potential design could increase the quality of treated patients' lives and reduce the risk of infection as suggested by Trumble et al. [150]. Additionally, many of the VADs need to be redesigned or adjusted to fit the specific sizes of patients' hearts [150]. Alternatively, in the case of pump based devices the blood flow needs to be carefully controlled [40]. This indicates the demand for a novel, highly reconfigurable device which does not require transcutaneous elements for operation and which could be activated by an external energy source. An additional benefit would be development of software and manufacturing process which allows for tailoring the device to personal needs of the patient in a short time.

The above review of ventricular assist devices and description of the complex heart motion determine the scope for improvement and requirements set for a new VAD. No device currently available incorporates all of the desired traits simultaneously:

- Motion range close to that of a healthy heart
- Operation without a need for transcutaneous elements or piercing the heart
- Adjustability of motion range
- Tailorability to the size of patient's heart
- Suitability for both destination and bridge therapies

2.1.2. ARTIFICIAL MUSCLES

The idea of a ventricular assist device which would encapsulate and activate the myocardium resembles the concept of introducing an additional muscle into a human body. There is a class of devices and materials, which are used for such applications and bear the name of artificial muscles. They possess the capability of reversible contraction, expansion and rotation within one component under application of a stimulus [93]. The idea behind their creation was their use in life-saving technologies or in adverse environments [71].

The primary requirement for such applications is the ability to actuate the material on demand which is why various materials with such properties are considered, including polymers, ceramics, alloys and composites. Among the possible actuation mechanisms (thermal, magnetic, photo, capillary, chemical [162] or electroactuation [57]) the electroactive and magnetoactive materials are examined, including the ones with shape memory effects, due to their versatility and ease of stimulus application.

Biological muscles are only able to contract, which is why humans have antagonist muscles and stretchable tendons to allow for reversibility of motion. Human muscles also require energy to stay in the contracted state in opposite to those of mollusks which can reach a catch state [93]. Additionally, the operating temperature can affect the actuation times of muscles as well as their strength [105]. The range of possible temperatures is relatively narrow for natural muscles: 9°C [105] - around 42°C [51]. Because the designed device would be implanted into the human body it also needs to be capable of operation in this temperature range. It should also resemble or even have superior physical properties in comparison to natural muscles (see Table 2.2).

Table 2.2: Properties of natural muscles. Adapted from [93] with additional information on temperatures from [105] and [51]

Property	Typical	Maximum
Strain [%]	0.1 (sustainable)	0.35
Stress [MPa]	0.1	0.35
Density [kg/m^3	1037	-
Strain rate [%/s]	-	>50
Bandwidth [Hz]	-	20 (humans) 1000 (midges)
Efficiency [%]	-	40
Cycle life	-	>10^9
Modulus [MPa]	10-60	-
Operation temperatures	around 36 °C	42 °C

The desired properties of active materials used in actuators were established by previous researchers' work and additionally suggested in literature [71, 93, 109]. The ones relevant to the device designed in this project are:

- Applicability in the system
- Flexibility and strain capability that match the application
- High strength and actuation pressure
- Short reaction times
- Ability to operate in the given temperature range
- High energy density and efficiency
- Ease of manufacturing
- Low environmental impact and biocompatibility
- Long medical device lifetime
- Actuation directionality

Most of the physical requirements must be matched by the substance chosen for the application, so that it can perform well in the given environment. However, some of them like strain capabilities or actuation directionality can be fulfilled by careful design of the device's structure. This brings up the idea of using a relatively new group of materials - metamaterials.

2.2. METAMATERIALS

Materials are usually assigned to one of the main classes of metals, polymers, glasses, elastomers ceramics or hybrids (composites) based on similarities in physical properties, manufacturing processes and often applications [3]. Currently, as a result of research related to tuning the internal structure of the materials we can name an emerging group of metamaterials. "Metamaterials are carefully structured materials — often consisting of periodically arranged building blocks — that exhibit properties and functionalities that differ from and surpass those of their constituent materials rather than simply combining them" [12].

This type of materials was firstly developed for thermal, optical and acoustic applications [168] and later found application in low density [92, 125], ultra strong structures, as aforementioned materials for space missions or as reusable shock - absorbing materials [42]. One of the benefits given by metamaterials is their capability of going beyond the classical Cauchy elasticity by for instance twisting under axial load [42].

This thesis further develops the idea of designing an extremely reconfigurable metamaterial as in [14] but adapting the design to heart's shape in order to create a myocardium assisting device.

The above - mentioned supercompressible metamaterial developed by Bessa et al. [14] was inspired by the deployable masts [112], which serve as a solution to the limited cargo space in space missions and can be especially useful in telescope systems with large apertures and medium baselines. Other authors suggest more utilizations for this type of structure like spectrometer booms [141], solar sails [99] or radar masts [161].

The metamaterial (shown in Figure 2.5) consists of two rigid rings connected with slender elements called longerons. Under the influence of an external vertical force applied to the top ring, the longerons buckle, leading to significant volumetric strains even beyond 94%, depending on the configuration [14]. Such a mechanism is passive and requires the external force for the deformation to occur while an activation due to other stimulus with an altered geometry could lead to broadening the range of motion and applications.

Figure 2.5: Initial metamaterial geometry (Bessa et al. [14])

2.2.1. METAMATERIAL CLASSIFICATION

Metamaterials may have various structures, which dictate numerous possibilities in terms of their properties; however their classification differs across sources. The first categorization is the one presented by Bertoldi et al. [12]:

- Linear mechanical
- Mechanism based
- Instability based
- Topological metamaterials

Linear mechanical metamaterials are described by Young's modulus in case of the isotropic ones and the elasticity tensor in the case of anisotropic ones which can assume any form which satisfies the laws of thermodynamics. Examples include auxetic [6, 50, 102], extreme and pentamode materials [12, 66].

Mechanism based metamaterials are a collection of rigid elements connected together by flexible hinges. They are useful for deployable and energy absorbing structures. Common examples include: origami/kirigami based [41], topological and soft - mechanism based metamaterials [12, 117].

Instability based metamaterials show elastic instabilities and are capable of large deformations. They usually contain slender elements able to snap between multiple stable states. Various instability mechanisms are possible [12] but the main one - buckling is the one utilized by the metamaterial designed by Bessa, Glowacki and Houlder [14]. Depending on design, the buckling based materials can have a reversible behaviour. Snapping metamaterials usually retain the deformed shape after unloading [57, 59]. Common examples include: frustrated and programmable metamaterials [12].

Topological metamaterials are insensitive to presence of disorder in their microstructure as well as smooth deformations [12, 32]. The most common applications can be found in the field of condensed matter physics research [12].

An alternative classification is presented by Yu et al. [168]

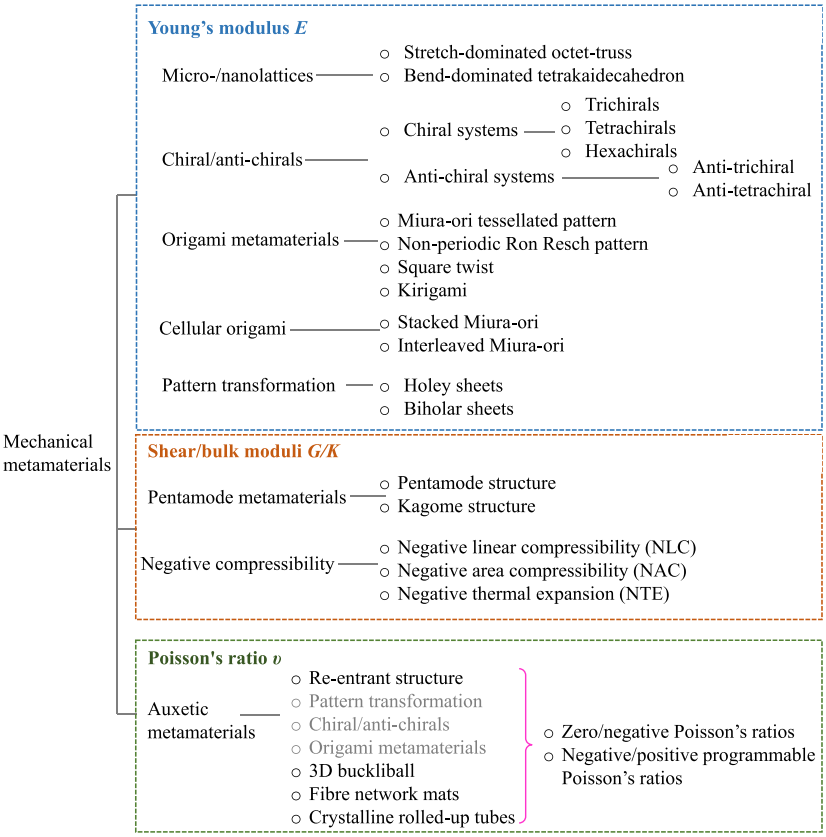

Figure 2.6: Metamaterial classification by Yu et al. [168]

Yu et al. categorize mechanical metamaterials with regards to their elastic constants - Young's modulus, shear modulus and bulk modulus as well as Poisson's ratio (see Figure 2.6).

Last classification by Hu et al. [57] differentiates metamaterials on the basis of their application - motion or energy related. The former group can be used for absorbers [26, 146], dampers, stabilizers or isolators [57]. Motion related metamaterials could find application in high motion rate applications as small perturbation can result in sudden snapping and reconfiguration of the material [57].

The metamaterial required for the ventricular assist device needs to undergo controlled squeezing and rotating motions. For this reason it is likely that the best type would be a motion related, mechanism based metamaterial with elements of limited flexibility. This may, however, not point towards the instability based metamaterial designed by Bessa et al. [14] at first. The reason for choosing to develop this particular structure into a VAD was its geometry which can be altered to fit the heart's shape. Additionally, it already had some traits of a mechanism based metamaterial like inclusion of rigid rings and their flexible joints with the longerons. The ring was seen as a potentially active element which could promote the squeezing motion, while longerons would encompass the myocardium and apply the strain to its surface.

2.3. ACTIVE MATERIALS

The purpose of this part of the literature review is to investigate materials suitable for activation of the heart assisting structure and establishing basic constitutive laws for analysis of their performance in FEM simulations.

The subsections below describe groups of materials considered for the application, specifically:

- Thermally activated materials 2.3.1
- Hygroscopic polymers and composites 2.3.2
- Electroactive polymers and alloys 2.3.3
- Shape memory materials 2.3.4
- Electroactive ceramics 2.3.5
- Electroactive composites 2.3.6
- Magnetoactive polymers 2.3.7

2.3.1. THERMALLY ACTIVATED MATERIALS

Increase in temperature causes expansion in most materials [147], although substances with negative thermal expansion coefficients also exist [81, 101].

Thermal expansion coefficient is defined as the ratio of the caused strain and temperature change that caused it [147]:

$$\alpha = \frac{\Delta L/L}{\Delta T} \tag{2.1}$$

Thermal expansion generates strain and, if constrained, stress [22]:

$$\sigma_{ij} = C_{ijkl}(\varepsilon_{kl} - \alpha_{kl}\Delta T) \tag{2.2}$$

Where C_{ijkl} is the elastic stiffness tensor and α_{kl} is a thermal expansion coefficient tensor.

Equivalently:

$$\varepsilon_{ij} = S_{ijkl}(\sigma_{kl} + \alpha_{ij}\Delta T) \tag{2.3}$$

with S_{ijkl} being the elastic compliance tensor

$$\begin{bmatrix} \varepsilon_1 \\ \varepsilon_2 \\ \varepsilon_3 \\ \gamma_{23} \\ \gamma_{31} \\ \gamma_{12} \end{bmatrix} = \begin{bmatrix} S_{11} & S_{12} & S_{13} & S_{14} & S_{15} & S_{16} \\ S_{21} & S_{22} & S_{23} & S_{24} & S_{25} & S_{26} \\ S_{31} & S_{32} & S_{33} & S_{34} & S_{35} & S_{36} \\ S_{41} & S_{42} & S_{43} & S_{44} & S_{45} & S_{46} \\ S_{51} & S_{52} & S_{53} & S_{54} & S_{55} & S_{56} \\ S_{61} & S_{62} & S_{63} & S_{64} & S_{65} & S_{66} \end{bmatrix} \begin{bmatrix} \sigma_1 \\ \sigma_2 \\ \sigma_3 \\ \tau_{23} \\ \tau_{31} \\ \tau_{12} \end{bmatrix} + \begin{bmatrix} \alpha_{11} \\ \alpha_{22} \\ \alpha_{33} \\ 2\alpha_{23} \\ 2\alpha_{13} \\ 2\alpha_{12} \end{bmatrix} \Delta T \tag{2.4}$$

Where:

$\tau_{23} = 2\sigma_{23}, \tau_{13} = 2\sigma_{13}, \tau_{12} = 2\sigma_{12}$

Direction of strain depends on the properties of the material contained in the thermal expansion coefficient. First three components of the vector ε_{11}, ε_{22} and ε_{33} correspond to strains in all three principal directions and the other three correspond to shear strains [81]. It is also possible to consider the thermal expansion in 2D and 3D in the form of area and volume strains respectively [147]. Typical values of the thermal expansion coefficient vary from $0.5\mu strain K^{-1}$ for silica glass up to $(450\mu strain K^{-1})$ for Ethylene Ethyl Acrylate Polymer (EEA) [1].

The thermal expansion simulation approach is a simple one available in most FEA software including ABAQUS, however it is not considered as a realistic activation mode due to the human body temperature limitations. In order to achieve significant local strains $(5-9\%)$ one would need to change the temperature of the structure by tens or hundreds of Kelvins [1] which is not feasible inside a human chest. The thermal model may serve another purpose - if the required material specific models are unavailable or for the sake

of simplicity it is possible to use the analogy between other deformation modes (for instance piezoelectric) and the thermal expansion [34, 38].

2.3.2. HYGROSCOPIC POLYMERS AND COMPOSITES

An alternative option to thermal loading of a material is putting the part in an environment with high moisture for expansion or low for contraction. Some materials, like polymers, exhibit the ability to absorb and desorb significant amounts of moisture, which results in an increase or decrease in their mass and volume. Such an effect is called hygroscopic swelling [104]. Some researchers have already successfully utilized this effect in smart materials [82, 83].

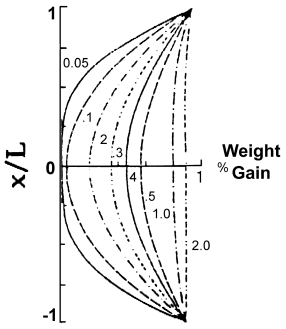

Figure 2.7: Exemplary one-dimensional weight gain based on Fickean kinetics (dashed curves represent situations at different normalized times) [158]

Absorption of moisture is a relatively slow process, in comparison to other forms of smart structure activation, due to the need for penetration of the material by diffusion [104]. Unbound water molecules penetrate the material and occupy the free volume. The swelling and plasticization effects may therefore be slower in the beginning in comparison to a later stage when most of the free volume is already occupied and addition of water content starts to cause stretching of the material [157]. For this reason it is possible that the hygroscopic swelling effect is mostly observed after a specific threshold of moisture content [158].

The expansion can be quantified with the diffusion coefficient D, which defines the rate at which moisture spreads in the material. This coefficient is not only affected by the amount of free space in the material which can be occupied by moisture but also by the affinity between the material and water molecules [157] or temperature [158]. Another crucial parameter is the moisture absorption capacity C^{∞} which quantifies the water amount that the material is capable of absorbing if given infinite time in a moist environment [104]. Current material water content C is defined as follows [28]:

$$C = \frac{\text{Wet weight - dry weight}}{\text{Dry weight/density}} \tag{2.5}$$

The sorption - time characteristic may assume various shapes (example in Figure 2.7), depending on the properties of the material, possible damage and physical or chemical break-downs of the material [158].

The aforementioned moisture sorption results in strain of the material and possibly stress, depending on the constraints. A constitutive law for this process is similar to the one which describes the thermal expansion [60, 104]:

$$\sigma = C(\varepsilon - \beta \Delta M) \tag{2.6}$$

Where: σ - stress vector
ε_{ij} - strain vector
β_i - hygroscopic expansion coefficient
ΔM - moisture content change (%)
C - stiffness matrix

Coefficient of moisture expansion ranges between $2 \cdot 10^{-3}$ and $5 \cdot 10^{-3}$ per 1% weight gain which is roughly 100 times the typical thermal expansion coefficient α - $2 \cdot 10^{-5} \frac{1}{K}$ [158].

Despite the benefit of simplicity and presence of moisture within the human body, the hygroscopic swelling activation is perceived as one of the least favourable possibilities due to long activation times and highly hysteretic behaviour [158].

2.3.3. ELECTROACTIVE POLYMERS AND ALLOYS

Wan et al. [155] define the electroactive materials as the ones that undergo shape or dimensional change in response to application of an electric field.

Multiple authors compare electroactive polymers of various types, described in this section, to human muscles [8, 109]. Within the electroactive polymers (EAP) two main groups can be defined - ionic and electronic [8, 155].

There are traits that make polymers appealing potential material candidates as they are generally lightweight, flexible, come in many forms and are easy to process and mass produce (see Figure 2.8) [8, 155].

Ionic EAP bending actuation is based on transport or diffusion of ions or molecules [16, 155]. They usually consist of two electrodes and electrolytic medium [8]. Ionic EAPs are characterised by low activation voltages below 5V and often biocompatibility [155]. Most of the ionic polymers can be used both as actuators and sensors [16]. Despite the benefits, this group of materials is not suitable due to the ion reservoir requirement (electrolyte presence) and need for encapsulation [16, 155]. It is also hard to maintain constant displacement under DC voltage activation (except for conducting polymers) [8, 16], which is not a requirement but just an inconvenience at a potential testing stage. The last aspect that prevents one from using the ionic EAPs is the activation speed which due to ion migration is measured in tens of a second [8].

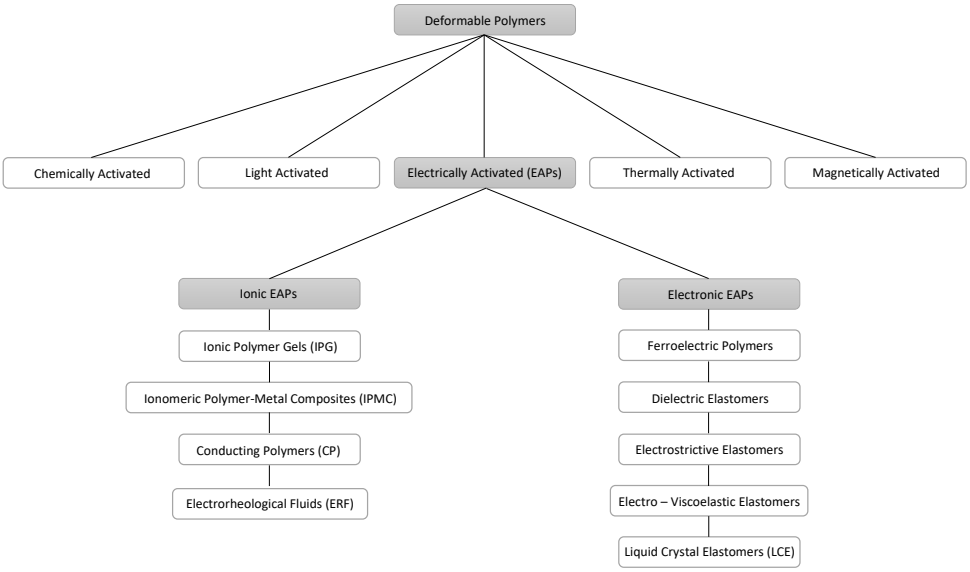

Figure 2.8: Summary of deformable polymer types adapted from article by Zhang et al. [91]

Electronic EAPs are activated by Coulomb forces originating from an electric field between electrodes on a film shaped polymer material [8]. The main examples include piezoelectric polymers, dielectric elastomer EAPs, electrostrictive polymers and liquid crystal elastomers. As a group they present a wide range of possible strains (from 0.1% to 380%) [87], they are free of electrolyte and provide short response times (mostly measured in milliseconds) [155]. The main disadvantage of the electronic EAPs is the closeness of the required high electric fields to the polymer breakdown level [7]. This can, however be alleviated by creation of multilayered structures with thin films or increasing the dielectric constant of the material by inclusion of particulates [8]. High electric fields also have a benefit in the form of low currents leading to low energy losses [71].

Table 2.3: Comparison of ionic and electronic EAPs. Adapted from [16]

Property	Electronic	Ionic
Activation voltage	Large	Small
Controllability	Easy	Difficult
Energy density	Good	Poor
Mechanism	Coulomb forces	Mobility or diffusion of ions
Electrolyte	Absent (dry)	Present (wet)
Displacement	Change of shape or dimensions	Bending
Ability to retain displacement	Yes	Only conductive polymers (CP)

Out of the group of electronic polymers the three types considered are:

- Ferroelectric polymers 2.3.3
- Dielectric elastomers 2.3.3
- Electrostrictive polymers 2.3.3

The liquid crystal elastomers are mainly rejected because of long actuation cycles. Their electroactive properties are based on Joule heating. Current passage results in temperature increase and phase change between nematic and isotropic phases usually within 1 second, however the cooling takes as long as 10 seconds [8].

FERROELECTRIC POLYMERS

Ferroelectric polymers are polar, crystalline materials characterised by a spontaneous electric polarization, which is reversible under an influence of an external electric field [89]. Within the group we can define typical ferroelectrics with a broad hysteresis loop and sudden dielectricity constant increase close to Curie temperature and relaxor ferroelectrics with a narrower hysteresis loop and a rounded peak of dielectric constant close to Curie temperature [80]. The most well-known ferroelectric polymer is polyvinylidene fluoride (PVDF) developed in the early 1970s.

All ferroelectric materials are also piezoelectric which is the crucial material property [80]. Piezoelectricity is defined as the ability of the material to produce electrical charges across its boundaries as a result of applied mechanical stress. The indirect piezoelectric effect is the exact opposite - strain is caused in the material due to application of an electric field to it [114]. A complex review of piezoelectric materials and their history was created by Uchino [153].

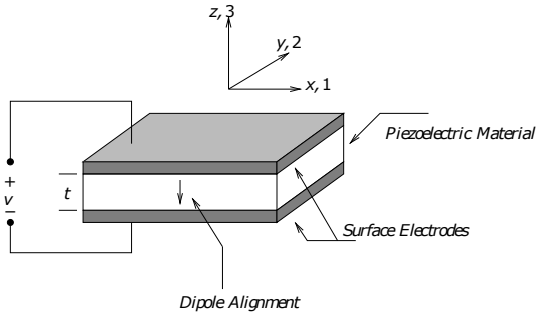

Figure 2.9: Piezoelectric material schematic [96]

Piezoelectric materials can be classified as bulk polymers, composites or voided charged polymers. These materials, being non - centrosymmetric [89], make use of the internal dipoles, which are oriented in the preferred direction by a process called poling [64]. It strengthens the piezoelectric properties of the material, which in the case of ferroelectric materials can initially be minimal due to random orientation of dipoles [80]. Afterwards, application of electric field in the direction of polarization results in material deformation [64]. In piezoelectric activation the strain is proportional to the strength of applied electric field and usually is below 1% [80] which is why they are usually used for sensors [8].

The coupled electromechanical constitutive law for piezoelectric materials is based on an assumption that the total strain consists of two components - one caused by the mechanical stress and the other one by the applied voltage [96].

The equation representing the converse piezoelectric effect at constant electric field (2.7) contains subscripts as shown in Figure 2.9. Axis 3 corresponds to the direction of initial polarization/poling, while the other two axes are perpendicular [96]. Ideal piezoelectric materials have a linear strain response to electric field, however ferroelectric materials like PVDF show a butterfly shaped hysteresis curve [80].

$$\varepsilon_i = S_{ij}^E \sigma_j + d_{mi} E_m \tag{2.7}$$

$$D_m = d_{mi} \sigma_i + \xi_{ik}^\sigma E_k \tag{2.8}$$

Where:
σ - stress vector $[N/m^2]$
ε - strain vector $[m/m]$
E - vector of applied electric field $[V/m]$
D - vector of electric displacement $[C/m^2]$
ξ_k - permittivity $[F/m]$
d - matrix of piezoelectric strain constants $[V/m]$
S - matrix of compliance coefficients $[m^2/N]$

Indices i, j = 1,2,3,4,5 or 6 and indices m, k=1,2 or 3

Electroactive actuation can assume different shape change modes described by the piezoelectric strain constant. It is represented as a 3 x 6 tensor containing ratios of strain to applied electric field [96]. For d_{ij} the subscript means that the field is applied in the i direction while displacement is expected in j direction. The most important elements are d_{31} and d_{33} corresponding to transverse and longitudinal coefficients respectively [114]. As the names state, they measure the amplitude of strain induced by unit voltage in the respective directions [80] (see Figure 2.10). The values of the piezoelectric strain coefficients can assume positive as well as negative values [61] resulting in either stretching or compression of the material under application of electric field in the given direction.

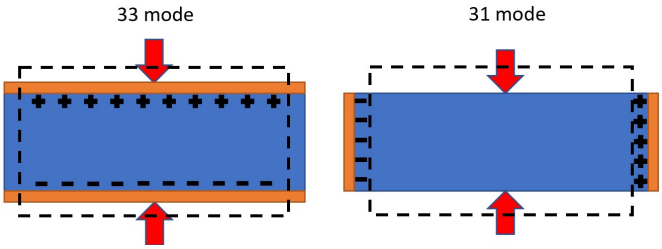

Figure 2.10: Piezoelectric transduction modes (adapted from [114])

The elastic compliance matrix contains coefficients being the ratio of the strain in direction i to the stress applied in direction j given no stress change in other directions. Subscripts 1-3 denote direct stresses and strains while subscripts 4-6 denote the shear strains and stresses [96].

2

For the most common piezoelectric polymer - PVDF, Moheimani and Fleming [96] suggest using the piezoelectric strain coefficient matrix below due to nonisotropic stresses on the surfaces of films.

$$d = \begin{bmatrix} 0 & 0 & d_{31} \\ 0 & 0 & d_{32} \\ 0 & 0 & d_{33} \\ 0 & d_{15} & 0 \\ d_{15} & 0 & 0 \\ 0 & 0 & 0 \end{bmatrix} \tag{2.9}$$

With a matrix like the one given in eq. (2.36) application of electric field in the direction of polarization results in different strains in directions of axes 1 and 2 [96].

Within the group of electroactive materials their performance is usually quantified with a coupling factor k^2 or efficiency, which can be as high as 90% [71].

$$k^2 = \frac{\text{Stored mechanical energy}}{\text{electrical energy input}} \tag{2.10}$$

$$\eta = \frac{\text{Output mechanical energy}}{\text{Consumed electrical energy}} \tag{2.11}$$

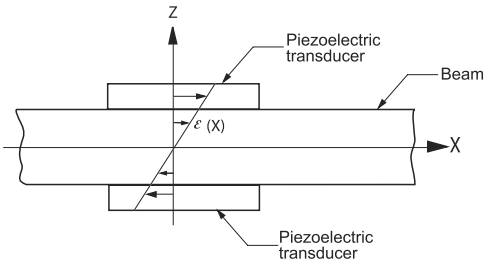

Figure 2.11: Bending beam actuation [96]

Moheimani and Fleming [96] show a potentially useful way of bending actuation for beams (see Figure 2.11). Two piezoelectric transducers can be used under opposite electric fields in order to induce bending.

The piezoelectric polymers like PVDF are seemingly suitable for the metamaterial due to possibility of application by cooling from melt or drying from solutions [80]. Printing in the case of some piezoelectric polymers is also possible [10]. The activation times below 1 ms are more than suitable for the potential application along with acceptable

activation stresses of more than 100 MPa in the case of ceramics and up to 4.8 MPa in the case of polymers. However, the maximum strains being below 0.1% for polymers and 0.2% for ceramics rule out all possible modes of activation of the metamaterial [96, 116].

ELECTROSTRICTIVE POLYMERS

Dielectric elastomers and electrostrictive polymers both belong to a group of dielectric electroactive polymers [169]. All dielectric materials exhibit displacement of atoms within the crystal lattice if an external electric field is applied to them. This effect is called electrostriction [93]. The effect is mostly detectable in softer and compressible materials [68].

The unit cell of an electrostrictive material is centro - symmetric because of which the strain does not come from change in structure but rather is inherent to it [64]. The mechanism behind actuation is based on separation of charged ions within the unit cell of the material [64]. Similar explanation is given by Kao [68] - internal polarization of the material involves displacement of electric charges, which causes them to be arranged non - symetrically. The polarization of ions in the material structure is more likely to happen in the form of extension of the lattice instead of compression, which is why for most of the electrostrictive materials the longitudinal coupling coefficient is positive [79]. The mechanism is presented in Figure 2.12. If the energy required to compress the pair of ions U_C is larger than the one required to stretch the pair U_E the longitudinal electrostrictive coefficient Q_{33} is positive or vice versa [79]. The effect of electrostriction is mostly visible in ceramics, polymers and some liquids which are slightly compressible as it leads to a minimal volume decrease [68].

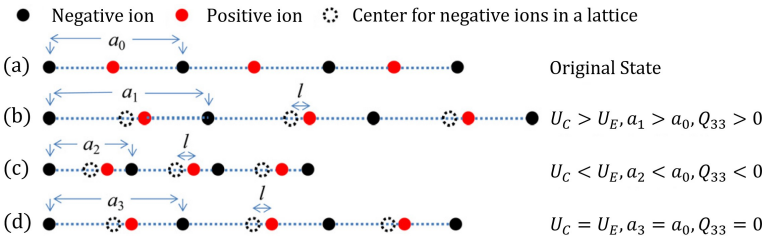

Figure 2.12: Principle of electrostriction - visualisation [79]. U_C and U_E denote the energy required to compress or extend an ion pair respectively, a is the distance between negative ions and Q_{33} is the electrostrictive coefficient.

As presented by Kornbluh [71] the basic law for electrostrictive materials describes the stress generated under influence of electric field:

$$\sigma = \varepsilon_r \varepsilon_0 E^2 \tag{2.12}$$

Also as defined by multiple authors [27, 79, 134] for a uniform material :

$$\varepsilon_{ij} = \varepsilon_r \varepsilon_0 \frac{E^2}{Y} = \gamma_{ijkl} E_k E_l \tag{2.13}$$

Where:
ε_r - relative dielectric constant of the material
ε_0 - permittivity of vacuum
E - Electric field applied between the electrodes
Y - Young's modulus
γ_{ijkl} - fourth rank electrostriction tensor

The relationship between stress or strain and the electric field is presented by equations 2.12 and 2.13 and is clearly quadratic, leading to theoretically stronger actuation for the same field than in the case of piezoelectrics [8]. This kind of relationship is a result of the field affecting the material in a twofold way - firstly it induces and maintains the charges, secondly it pulls the charges towards each other [27].

In the case of materials with large elastic compliance like soft polymers or materials with low dielectric constant the Maxwell stress contribution needs to be included [79]. Longitudinal strain in dielectrics caused by Maxwell stress is:

$$\varepsilon_{Maxwell} = -\frac{1}{2} s \epsilon_d E^2 \tag{2.14}$$

Where s is the elastic compliance of the investigated material and ε_d is the material's dielectric permittivity.

Electrostrictive polymers were suggested for use in artificial muscles by Kornbluh et al. in 1998. Flexible Electrostrictive Polymer Artificial Muscle (EPAM) devices were described as matching and even surpassing biological muscles in terms of some of their properties. Typically strains of such polymers reach up to 4% [169] and stresses are as high as 43 MPa [116]. Reaction times observed are below 1 ms and efficiencies as high as 90%, while typically above 80% due to low energy losses in electrostrictive polymers (mainly due to viscoelasticity) [71].

The application of electrostrictive polymer films in actuators is usually done by spin or dip coating. It is crucial for the film to be uniform in order to avoid electrical breakdown of the polymer [71]. The electrodes used with electroactive polymers must be compliant in order to maximize the strains and limit energy losses [8]. Common options are brushed powdered graphite electrodes (wear off with time) or polymers with conductive particles like carbon black (more durable but add stiffness) which are applied by spraying or dipping [71]. Despite development of the described manufacturing techniques the use of electrostrictive polymers is still restricted to thin films due to the high required electric fields (measured in MV/m) [116]. Therefore, the electrostrictive polymers may only be considered in elements like bimorph/uniform bending beams in macroscale.

DIELECTRIC ELASTOMERS

Dielectric elastomers are materials which can be used for quick response large strain actuators [164] with high efficiency and energy density [87] as well as reliability and durability [171]. According to Carpi [27] highly deformable materials with moduli up to 10 MPa usually fall into either the category of elastomers or gel materials. Pelrine et al. [109] suggest that the former ones (dielectric elastomers) could be used to mimic natural muscles [155].

In terms of structure the dielectric elastomer based actuators can be represented as parallel plate capacitors (see Figure 2.13) with flexible electrodes and compliant dielectric core [8]. The main cause for actuation is the Maxwell stress [17].

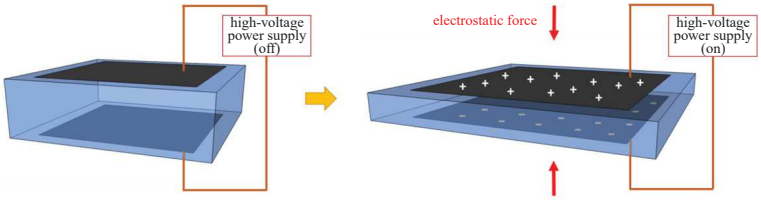

Figure 2.13: Actuation of a dielectric EAP by Wang et al. [155]

Carpi [27] suggests a few assumptions that simplify the analysis of dielectric elastomer actuation. Namely:

- Polymer and electrode materials are isotropic
- The electrodes are infinitely conductive and compliant
- Constant moduli of elasticity for the dielectric and zero modulus of elasticity for the electrodes
- Negligible hysteresis and viscoelasticity
- Material is incompressible

It is impossible to find a material ideally matching the assumptions, however some of them are close enough or it is possible to mitigate the differences. For instance the imperfection of electrode compliance can be included in the strain equation in the form of compliance matrix coefficient [27]. The constitutive law [109], often called the "Pelrine law" [160] for materials with negligible electrostrictive effects is:

$$\varepsilon = \varepsilon_r \varepsilon_0 \frac{E^2}{Y} = \varepsilon_r \varepsilon_0 \frac{V^2}{Y z^2} \tag{2.15}$$

Where z is the thickness of the element and V is the voltage applied.

In the case of large strains a z - direction strain s_{zz} correction for thickness of the actuator is required [27] in the form:

$$z = z_0(1 + s_{zz}) \tag{2.16}$$

An alternative formulation of the constitutive law for isotropic dielectrics showing both electrostrictive and Maxwell effects was explained by Krakovsky et al. [72]:

$$\sigma_{xx} = \frac{1}{2}\varepsilon_0\varepsilon_r E^2\left(1 + \frac{a_2}{\varepsilon_r}\right) \tag{2.17}$$

$$\sigma_{zz} = -\frac{1}{2}\varepsilon_0\varepsilon_r E^2\left(1 - \frac{a_1 + a_2}{\varepsilon_r}\right) \tag{2.18}$$

Where a_1 and a_2 are parameters related to the electrostriction, which describe the changes in dielectric properties under shear and bulk deformation [72]. The terms which do not contain the a coefficients are the ones related to Maxwell stress [72]. Petcharoen [111] confirms that for some materials like polyurethane the electromechanical response is a result of both electrostriction and Maxwell stress with a significant contribution of both (65 % and 35% respectively).

A discrepancy in formulae describing the stress and strain can be seen in the form of the $\frac{1}{2}$ coefficient. Carpi [27], Pelrine et al. [109], Löwe et al. [91] or Zhang et al. suggest the use of eq. (2.15). On the other hand Krakovsky et al. [72], Li et al. [79] recommend using equations containing the $\frac{1}{2}$ constant. Pelrine et al. [110] explain the doubled strain and pressure as a result of an assumption that the electrodes are perfectly compliant, only small strains are obtained and that the material is incompressible with a Poisson's ratio of 0.5. This causes the material to be solely compressed along the direction of field application and stretched transversely (increase in area).

Dielectric elastomers are characterised by low stiffness, high dielectric breakdown strength and large strain capability (up to 380% [87]) [8]. The typical activation times are measured in milliseconds [116]. It is worth noting that the strain can decrease over time due to creep release [8].

Dynamic mechanical analysis of dielectric elastomers may be more complicated due to their structure as application of electric field causes stiffening of the elastomer as described by Petcharoen [111].

The dielectric elastomers consist of three components - elastomer, catalyst and plasticizer with variable ratios which can be used to tune the actuator. Other crucial elements are the electrodes which need to be compliant, exactly in the same way as in electrostrictive polymer actuators which is why carbon grease is a suitable material [87].

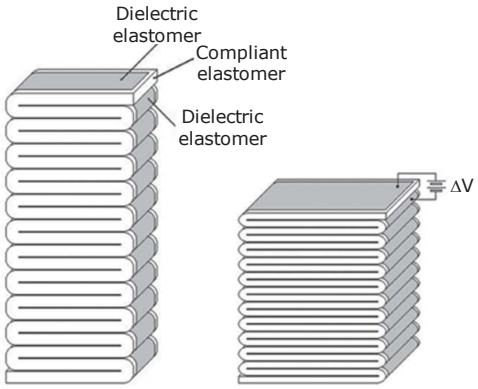

Figure 2.14: Stacked DEA [8]

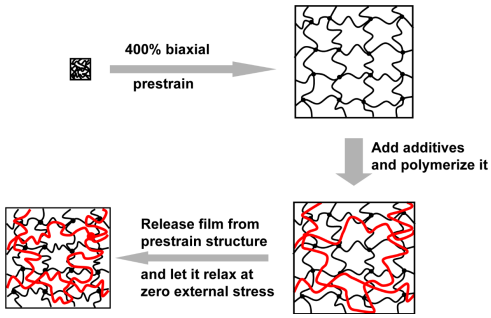

Figure 2.15: Prestretching process as presented by Qiu et al. [113]

The main two dielectric elastomers utilized are acrylate and silicone [169]. Acrylate provides higher maximum stress of around 7.2 MPa and maximum areal strain of almost 400% [169] while the silicone based mechanisms provide faster responses, broader temperature range stability and less viscosity [91]. The process responsible for increasing the strains and also the resistance to electrical breakdown in dielectric elastomers is prestraining the dielectric material [87] up to five times the original size (Figure 2.15) [91]. The force exerted by the mechanism can be multiplied by stacking them in layers (Figure 2.14) while the displacement can be increased by connecting them in series [91]. Application of the dielectric elastomer films is usually done similarly to electrostrictive polymers by spin coating or dipping, otherwise by casting or spraying [109].

Despite great strains that can be achieved with such materials and excellent activation times one would need a full analysis of a stacked dielectric actuator in order to design a metamaterial made out of it. Otherwise the dielectric elastomers can only be used in sheets and their thickness is limited to tens of micrometres which is not suitable for the application.

2.3.4. SHAPE MEMORY MATERIALS

Shape memory materials are capable of generating high strains and forces but often at the cost of slow actuation and large hysteresis [170]. They can show either shape memory effect, shape change effect or both [57]. If the material is capable of elastic or viscoelastic shape change it is defined as the shape change effect and if it is able to maintain the deformed shape until a stimulus is applied it is called shape memory effect [59]. Within the group possessing the shape memory trait one can distinguish shape memory polymers and shape memory alloys, some of both can be electroactivated [57].

The shape memory effect in shape memory alloys is a result of a martensitic transformation, while in the shape memory polymers it comes from a dual segment system as described by Leng et al. [77]. The shape recovery can be induced by various stimuli

depending on the material, including stress or temperature change [57] as well as stimulation by water (swelling/drying out) or electricity [59].

According to Liu et al. [86] the shape memory polymers are defined as macromolecular smart materials capable of changing their macroscopic properties under the influence of an external stimulus. They are lightweight, inexpensive materials which due to being highly deformable can be easily manufactured. Other advantages include biodegradability in most cases and tailorability of glass transition temperature [86]. On the other hand, their low stiffness leads to low recovery stresses, which can be alleviated by addition of fillers and creation of shape memory polymer composites. Such fillers usually include carbon black, carbon nanotubes or fibres of various kinds to increase stiffness. Additionally, electrically conductive fillers can be utilized to provide electroactivity [86]. The shape memory polymers and polymer composites come in two forms - either thermoplastic or thermoset. The thermoplastic ones lose shape memory after a few cycles while thermosets keep it for longer as well as provide higher stiffness, transition temperature and durability [86].

Both shape memory polymers and alloys have variable properties at different temperatures with glass transition and melting temperatures being critical [86]. As can be seen in Table 2.4 the shape memory materials can usually operate within a narrow range of temperatures, which fit those found in human body. Nevertheless, recovery times are too long and disqualify shape memory polymers as potential candidates for the metamaterial based structure [163].

Additional information in the following references:

- Shape memory alloys: [100, 107]
- Shape memory polymers: [73, 76]
- Optimization and programming of the shape memory effect: [143]
- Types of shape memory effect: [58]

The tabulated comparison (Table 2.4) yields a verdict that neither SMPs nor SMAs can be considered as suitable for the actuation mechanism in the metamaterial. SMPs have low strengths and long actuation cycles while the shape memory alloys despite being much faster, stronger and durable are too difficult in handling and shaping for a device which needs to be manufactured quickly in urgent situations.

Table 2.4: Comparison of shape memory polymers and alloys. Adapted from [84, 95, 144]

Property	Shape memory polymers	Shape memory alloys
Density [g/cm^3]	0.9 -1.1	6 - 8
Phase transformations	Glass transition	Martensitic transformation
Strain [%]	< 800	< 8
Young's modulus at T<T_{tran} [GPa]	0.01 - 3	83 (NiTi)
Young's modulus at T>T_{tran} [GPa]	$(0.1-10)\cdot 10^{-3}$	28 - 41
Stress required for deformation [MPa]	1 - 3	50 - 200
Stress generated during recovery [MPa]	1 - 3	150 - 300
Critical temperature [°C]	(-10) - 100	(-10) - 100
Recovery speeds	< 1 s - several minutes	> 0.1 s
Efficiency [%]	18	25
Biocompatibility	Can be biocompatible and/or biodegradable	Some are biocompatible not biodegradable
Processing conditions	< 200 °C, low pressure	> 1000 °C and high pressure
Corrosion performance	Excellent	Excellent
Shape training	Easy and fast	Difficult
Cost	Cheap	Expensive
Cycle life	< 10^6	< $5\cdot 10^6$

2.3.5. ELECTROACTIVE CERAMICS

Ceramics are also a member of the electroactive material family [155]. Their properties could probably be best described as extreme with dielectric constants reaching thousands [61] and strains being limited to as little as 0.1% [170]. The main examples are lead based ceramics like zirconate titanate (PZT) [69], lead magnesium niobate (PMN) or lead magnesium niobate-lead titanate (PMN-PT) [93]. Lead free materials also exist, for instance the barium titanate ($BaTiO_3$) [166]. The group of piezoelectric ceramics shows possible stresses above 100 MPa, efficiencies above 90% and fast reaction times [109]. The ceramics have also previously been successfully used in metamaterials on nanoscale including alumina as described by Meza et al. [92].

Ceramics have relatively good shaping properties and can be formed by molding (press, tape or injection), extrusion or starch consolidation. with good reproducibility [69]. The main issue are the low displacements, which could potentially be alleviated by creation of bimorph [69] or multilayer structures [145]. However, this and high processing temperatures (above 1000 °C) [69] make their use infeasible in this project.

2.3.6. COMPOSITE ELECTROACTIVE MATERIALS

Piezoelectric composites are materials formed as a combination of a piezoelectric polymer or ceramic with non-piezoelectric materials. Voids as a constituent part are also possible [136]. It is highly advantageous to mix piezoelectric ceramics with polymers in order to combine the high coupling factor and dielectric constant of ceramics and flexibility of polymers [114].

Three main groups of piezoelectric composites are considered - the (1-3) and (0-3) or (3-3) piezocomposites. The former ones are created by embedding inorganic piezoelectric pillars (square or cylindrical) in a polymer matrix [136]. The (0-3) and (3-3) forms are composites where the matrix is loaded with piezoelectric particles which are completely separated or in contact respectively [78]. For more information on various connectivity type composites please see Uchino [152].

There are two industrially available composite types within the (1-3) group - lead zirconate titanate (PZT) based, and composites based on lead magnesium niobate–lead titanate (PMN - PT). While both types are suitable for macroscale applications, PZT based composites only reach coupling coefficients up to 65% and PMN - PT based composites achieve ones as high as 85% thanks to reactive ion etching [114].

Smith [136] suggests that for applications requiring flexibility the piezoelectric rods should be embedded in polymers which allows for more strain. In such a case best traits of both materials are utilized - electromechanical coupling of the piezoelectric material and flexibility of the polymer [114]. In the (0-3) and (3-3) composites piezoelectric particles need to be mixed with the matrix and cured. This type of manufacturing, despite better applicability introduces modelling issues which are beyond the scope of this thesis.

It is particularly hard to find reliable information about all parameters of electroactive composites [114] especially the ones related to cycle lifes and Young moduli. This option could potentially be explored in further investigation.

2.3.7. MAGNETOACTIVE POLYMERS

Magnetoactive polymers (MAPs) are smart hybrid materials whose mechanical properties can be controlled with an external magnetic field. They bear similarity to rheological fluids, however MAPs are based on magnetic particles distributed in a solid matrix. This composite approach allows for their formation into complex shapes and retention of particles dispersion within the material [37].

Their properties and reaction to a magnetic field depend on the type and size of the magnetic particles. A unique feature is transition of the particles into single magnetic domains which as a system have paramagnetic properties if the size of particles drops below a specific size. They show no hysteresis, no remnant magnetisation and achieve high magnetic moments [44]. A common material used for the nanoparticles is Magnetite (Fe_3O_4) [74], for which the critical size is $30\mu m$ [31]. An important feature one must pay attention to is the correct spread of particles inside the matrix as aggregated particles may show a different behaviour under an external field application [44].

An interesting material for the desired application, which was used for the analysis presented in the following chapters, is based on polycaprolactone (PCL) used as a matrix doped with 20% of magnetite - reduced graphene oxide $rGO - Fe_3O_4$ nanoparticles embedded in it (see Figure 2.16). Similar particles were already described in terms of properties and manufacturing by Munasir and Kusumawati [98]. In such a combination magnetite plays the role of the magnetic material and the reduced graphite oxide adds great thermal and electrical properties to the design [98] which can be utilized at later stages of the project. Polycaprolactone, on the other hand, is a 3D printable [63], biocompatible, recyclable polyester, insoluble in water and alcohols, capable of significant strains up to 1000% [75].

Figure 2.16: Simplified nanoparticle preparation process (courtesy of Dr. M. Dias Castilho)

According to Dr. Castilho, a co-advisor of this work, the composite MAP is capable of activation up to 10% strain under the influence of an external magnetic field. Figure 2.17 shows the magnetic moments of the PCL based MAP. Most of the moment is achieved at around 5000 Oe which converts into 0.5 T.

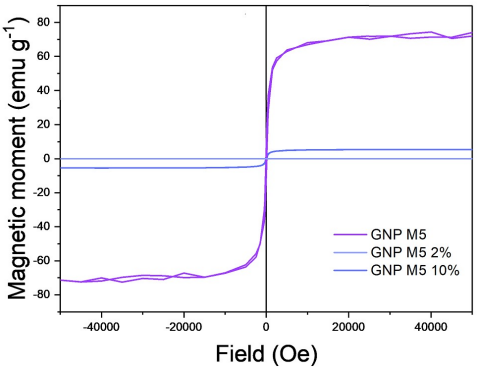

Figure 2.17: Magnetic moments induced in PCL+mGO printed fibres vs the strength of the external magnetic field (courtesy of Dr. M. Dias Castilho)

The Young's modulus of the MAP doped with 20% $rGO-Fe_3O_4$ particles is 405 MPa and it was obtained from tensile tests. Values for other particle percentage contents as well as the achievable magnetic moments can be seen in Table 2.5. Such should be checked under magnetization as according to literature [37] if any magnetorheological effect takes place, material's stiffness may change. This is usually true for very soft elastomers with Young moduli well below 1 MPa [142], hence it is not expected to distort the analysis significantly.

Table 2.5: Properties of the MAP produced by Dr. Castilho at different $rGO-Fe_3O_4$ doping percentages

$rGO-Fe_3O_4$ content [%]	Magnetic Moment	Elastic Modulus
2	0.04	360
10	5	382
20	9	405
100	74	-

2.4. MACHINE LEARNING

Similarly to the cases considered by Bessa et al. [13, 15] and Glowacki [45] the analysis of potential metamaterial designs is carried in a multidimensional design space. This kind of a problem requires a suitable method which can extract the patterns from multiple FEM simulations outputs and which is computationally inexpensive. While tuning the models for small databases can be done by trial and error, for larger ones it can be streamlined with machine learning techniques [13]. It is worth defining machine learning then, which according to Mitchell is:

Definition of Machine Learning: *A computer program is said to learn from experience E with respect to some class of tasks T and performance measure P, if its performance at tasks in T, as measured by P, improves with experience E.*

An overview of pattern recognition techniques and machine learning, specific to the metamaterial analysis was created by Glowacki [45]. Only a brief summary is presented below.

Learning can be described as either supervised when the model is trained on the basis of a set of preclassified data or unsupervised if the data is not labelled and classes are defined in the learning process [131]. Pattern recognition can be done with various systems out of which the best known ones include template matching, statistical classification, structural machining and neural networks [62]. In the previous work done by Glowacki [45] both classification and regression were utilized. What falls into the scope of this thesis is supervised machine learning in the form of regression (modelling a function which describes the quantity of interest [53], see section 2.4.1) and Bayesian optimization which is described in section 2.4.3. The former one is used for determination of

how quantities of interest depend on parameters which describe the geometry of the designed structure. Bayesian optimization, on the other hand, leads to establishing the values of parameters which describe a configuration that performs best in terms of a predefined objective.

In the statistical approach one defines the features in a d-dimensional space and in the machine learning process decision boundaries are found with criteria like a mean squared error for instance [62]. On the basis of the training dataset the program finds relationships between the features and classes, which later can be tested and applied for classification on pre-processed datasets [53]. In the case of a regression problem there is not a limited number of classes but rather the data is continuous, which means that the program is expected to learn and come up with a model which predicts the target value on the basis of the input [53].

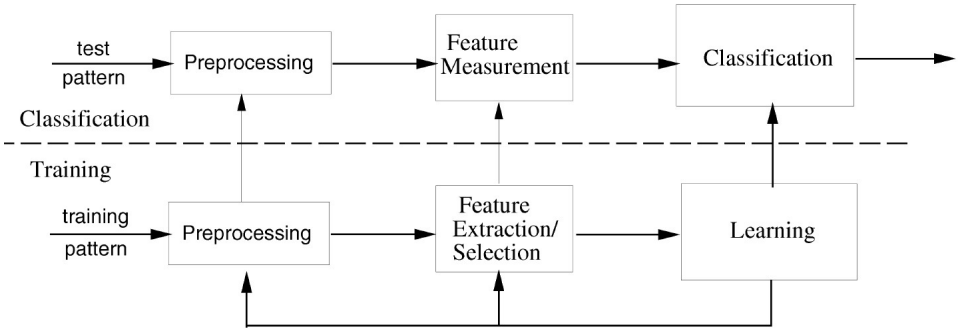

Figure 2.18: Statistical pattern recognition model [62]

The statistical machine learning framework (so called " The learner's input") [131] can be divided into :

- **Domain set:** An arbitrary set of objects X to be labelled, usually shown as a d-dimensional vector containing all the features
- **Label set:** Set of output values (y), either in the form of labels for discretized outputs or an infinite set in the case of continuous outputs
- **Training set:** Part of the known set of (X,y) pairs which is used to train the model
- **The prediction rule:** The classifier or equations expected on the basis of the learning process, which map inputs X to outputs Y
- **Test set:** The remainder of the known set of (X,y) pairs used to assess the validity of the found prediction rule
- **Measures of success:** An error of the predictor represented in the form of probability of it predicting an incorrect output on a random point from the input data set. A commonly chosen one is the mean squared error function

2.4.1. GAUSSIAN PROCESS REGRESSION

The regression problem in this thesis is mostly addressed with Gaussian processes. They are non-parametric, stochastic models utilizing Bayesian theory with a Gaussian prior [128]. Gaussian process regression models are based on definition of probability distribution over possible functions and subsequent inference [115].

Gaussian processes can be used for multiple purposes [127]:

- **Function modelling:** Establishing a relation between inputs and outputs in a function form
- **Function exploration:** Choosing the input points for which one wants to observe the outputs so that the model is as accurate as possible and obtained efficiently
- **Function exploration - exploitation:** Choosing the inputs points for which one wants to observe the highest outputs and maximize total reward within specific time

The first purpose is related to the function regression. The second and third applications of Gaussian process regression are linked to determination of trends in the design space and optimization, where the Gaussian Process can play the role of a surrogate model, respectively.

Left side of Figure 2.19 presents an initial belief about expected functions in the form of probability distribution. Average of functions presented in the figure is zero due to lack of additional information. If it becomes available, the knowledge about functions and therefore probability is updated [115]. When new points become known, the prior probability function is combined with the likelihood and a posterior distribution is obtained for which the functions pass through the known points [115] (see the right side of Figure 2.19). The task which the machine learning process is supposed to perform is optimization of the covariance function parameters [115].

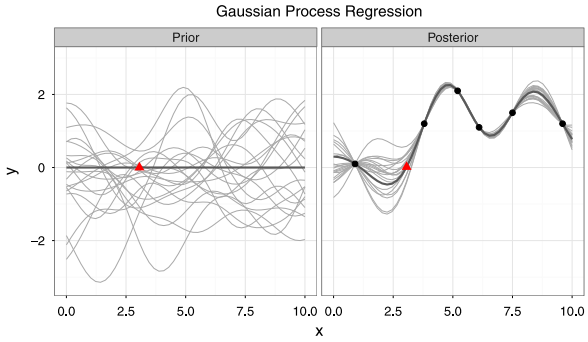

Figure 2.19: Comparison of prior and posterior descriptor function distributions [127]. Grey lines are samples from the Gaussian Process, black dots indicate observations and dark lines represent mean of the function.

The Gaussian process is fully specified by the mean $m(x)$ and covariance $k(x,x')$ functions:

$$f(x) \sim \mathcal{GP}\left(m(x), k(x,x')\right) \tag{2.19}$$

Where:

$$m(x) = E\left[f(x)\right] \tag{2.20}$$

$$k(x,x') = E\left[\left(f(x) - m(x)\right)\left(f(x') - m(x')\right)\right] \tag{2.21}$$

The covariance function, often called a kernel, models the joint variability of the random variables and needs to be defined by the user [20] on the basis of factors like expected function smoothness and patterns [127]. Choice of the kernel sets prior information about the distribution and affects convergence of the process [115]. It usually assumes more similarity between close points and less between distant ones. A commonly used kernel for smooth and stationary functions is the radial basis function kernel [127] with hyperparameters in the form of variance of the noise signal σ_f^2 and length-scale l:

$$k\left(x,x'\right) = \sigma_f^2 exp\left(-\frac{||\, x - x' \,||^2}{2l^2}\right) \tag{2.22}$$

The likelihood of the functions of interests is obtained with the help of Bayes rule [115]:

$$\text{posterior} = \frac{\text{likelihood} \times \text{prior}}{\text{marginal likelihood}} \tag{2.23}$$

The posterior distribution is denoted as:

$$f_* \mid X, y, X_* \sim \mathcal{N}\left(K(X_*,X)[K(X,X)+\sigma^2 I]^{-1} y,\ K(X_*,X_*) - K(X_*,X)[K(X,X)+\sigma^2 I]^{-1} K(X,X_*)\right) \tag{2.24}$$

The log marginal likelihood, which is used to train the GP by finding a local maximum (with respect to the kernel hyperparameters) [137] is equal to:

$$log\, p(y \mid X) = -\frac{1}{2} y^T (K + \sigma_n^2 I)^{-1} y - \frac{1}{2} log \mid K + \sigma_n^2 I \mid - \frac{n}{2} log 2\pi \tag{2.25}$$

Where:
f_* - Gaussian process prediction
X - D x n matrix of the training inputs
D - number of dimensions
n - number of data points
X_* - matrix of test inputs
K - covariance matrix
y - scalar output
σ_n^2 - noise variance
I - identity matrix of size n

For all other equations and derivations the reader is advised to look into the summary written by Glowacki [45], a tutorial on Gaussian distribution [127] as well as other relevant sources [20, 115].

2.4.2. SPARSE GAUSSIAN PROCESS REGRESSION

The standard Gaussian process approach has a primary limitation in the form of its cubic time complexity $\mathcal{O}(n^3)$ which results from the need to invert the determinant of the kernel matrix [85]. A solution to this problem was proposed in the form of scalable Gaussian processes which can be categorized as local or global approximations. The former ones assume the divide-and-conquer approach in order to train the models on local subsets of data [85]. Global approximations simplify or approximate the kernel matrix by considering only a subset of the training data (subset of data), removal of uncorrelated entries in the kernel matrix (sparse kernels) or employment of low - rank approximations (sparse approximations) [85].

Subset of data approach uses only a part of the training data with size m, reaching time complexity of $\mathcal{O}(m^3)$ with $m << n$. Limitation of the training data subset leads to a lower confidence about the prediction in comparison to the case when all datapoints are utilized [85].

Sparse kernels simplify the kernel matrix elements by setting them to zero for a distance between input points which exceeds a certain value. The time complexity is then $\mathcal{O}(\alpha n^3)$ with $0 < \alpha < 1$. Such a solution is mostly suitable for capturing local patterns [85] so its employment could lead to overlooking some global trends.

Sparse approximations achieve an improved performance with training time complexity of $\mathcal{O}(nm^2)$ [137]. m is the number of inducing points (pseudo - input points), which through Nyström approximation eq: (2.26) are used to summarize the training data dependencies [85].

$$K_{nn} \approx Q_{nn} = K_{nm} K_{mm}^{-1} K_{nm}^T \tag{2.26}$$

Global sparse approximations were previously utilized in the metamaterial analysis by Glowacki [45] and proved to be suitable for this design process. Thanks to focusing on global trends instead of local patterns they help with avoiding overfitting and prediction discontinuity which may be the case if the local approximations are used [85]. For this reason as well as availability of software which employs the global sparse approximations they are further investigated.

The sparse approximations are based on a set of inducing pairs (X_m, f_m), which represent the whole data set [85]. The inducing variable f_m is assumed to be statistically sufficient for the test data latent function f [85].

The sparse approximations to Gaussian processes can be further categorized [85] into:

- **Prior approximations:** Prior approximation with exact inference (complexity $\mathcal{O}(nm^2)$)
- **Posterior approximations:** Exact prior with approximated inference (complexity $\mathcal{O}(nm^2)$)
- **Structured sparse approximations:** Exploitation of specific Kronecker structures in the kernel matrix (complexity $\mathcal{O}(n)$)
- **Stochastic variational sparse approximations:** which utilize stochastic optimization (complexity $\mathcal{O}(m^3)$)

Where m is always the number of inducing points and n the total number of datapoints.

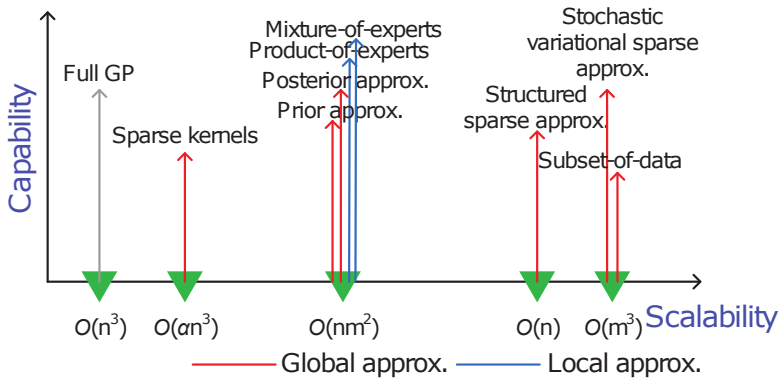

Figure 2.20: Comparison of available scalable Gaussian processes with respect to their scalability and capability [85]

Figure 2.20 reinforces the information available on various GP approximations. The highly scalable approaches may result in shorter computational time, however, apart from stochastic variational approximation their use results in loss of prediction capabilities. The methods with complexity $\mathcal{O}(m^3)$ do not benefit fully from increasing the dataset size. What can be inferred is that the best GP algorithms for the given application are the posterior approximations. They provide high capability and as proved by Bessa et al. can be used in the design process of a simply-parametrized metamaterial structure within time constraints of this project.

SPARSE POSTERIOR APPROXIMATIONS

The posterior approximations evaluate the prior exactly but approximate at the inference step. A well known solution for the posterior approximation procedure is the variational free energy described by Titsias [148]. Variational inference is used in order to approximate the posterior distribution [9] and the inducing inputs are defined as variational parameters [148], which protects them from overfitting [2]. Their selection is done on the basis of minimization of the Kullback - Leibler divergence between the approximated posterior distribution $p(f, f_m \mid y)$ and a variational distribution $q(f, f_m \mid y)$ [85, 148]:

$$KL(q(f, f_m \mid y) \mid\mid p(f, f_m \mid y)) = log\, p(y) - F_q \tag{2.27}$$

Where the so called evidence lower bound (ELBO) or the aforementioned variational free energy F_q can be used for optimization of the variational parameters and hyperparameters by its maximization [85, 148] and is represented as:

$$F_q = \left\langle log \frac{p(y, f, f_m)}{q(f, f_m \mid y)} \right\rangle_{q(f, f_m \mid y)} \tag{2.28}$$

Maximization of F_q with respect to the variational parameters results in an improved match between the evidence $p(y)$ and the posterior $p(f, f_m \mid y)$ [85].

Further knowledge on this method can be obtained from a summary done by Glowacki [45] or the relevant sources [2, 85, 148].

2.4.3. BAYESIAN OPTIMIZATION

Bayesian optimization has become a common way of finding the optimal solutions in cases such as hyperparameter tuning for machine learning applications [138] or constrained experiment design for example in the world of Materials Science [5, 108]. Typical global optimizers will usually reach the minimum of the given function, however at the expense of multiple function evaluations [43]. Bayesian optimization is applicable in situations when the cost of probing the values repeatedly is prohibitive and one desires to reach the optimum quickly and at low expense [43].

The Bayesian approach towards optimization evaluates the black-box functions sequentially, meaning that data is evaluated and sampling continues until a satisfying result is

obtained without a necessary predetermination of exact sample size [11, 94]. With an unknown function that is expensive to probe one may want to utilize two well known strategies - Gaussian Process (GP) surrogate model or tree structure Parzen estimator approach (TPE) [11]. For the sake of simplicity only the Gaussian Process approach is described as the analysis carried out in this thesis is mostly related to Gaussian Process based machine learning techniques.

The Bayesian framework solves a basic problem in the form:

$$\min_x f(x) \tag{2.29}$$

where $f(x)$ is the objective function to be minimized. Gaussian Process is used to update the prior belief about the function and quantify uncertainty at each point in order to pick the best location x^* for the next sample (look back at Figure 2.19). Function is evaluated at the point x^* and the posterior belief about it is updated with the Gaussian process model [43]. The described next point choice is taken on the basis of an acquisition function, which can lead to exploitation of the function, its exploration or be a trade-off between the two options [36].

The most common acquisition functions are expected improvement [65], maximum probability of improvement [94], upper confidence bound methods [33] or entropy search [54].

EXPECTED IMPROVEMENT

An acquisition function which balances exploration and exploitation is the expected improvement [36]. This expected improvement (EI) method tries to maximize the gain in the objective function as follows:

$$\tilde{I}(\hat{x}) = \max\left(0, f(x^+) - \tilde{f}(\hat{x})\right) \tag{2.30}$$

$$EI(\hat{x}) = \mathbb{E}\left[\tilde{I}(\hat{x}) | \hat{x}\right] \tag{2.31}$$

Where x^+ is the best point so far, $\hat{x}$ is a potentially considered point and $\tilde{f}(\hat{x})$ is a GP posterior random variable for $f(\hat{x})$ [43, 94]. This approach assigns a reward to the considered point if the predicted result would be better than the current minimum or 0 if it does not improve the result. The point with highest reward is then selected as the next sampling position [65].

An analytical evaluation of the expected improvement looks as follows:

$$EI(\hat{x}) = \begin{cases} \left(\tilde{\mu}(\hat{x}) - f(x^+)\right)\Phi(Z) + \sigma(\hat{x})\phi(Z) & \text{if} \quad \sigma(\hat{x}) > 0 \\ 0 & \text{if} \quad \sigma(\hat{x}) = 0 \end{cases} \tag{2.32}$$

Where:

$$Z = \frac{\tilde{\mu}(\hat{x}) - f(x^+)}{\sigma(\hat{x})} \tag{2.33}$$

Φ is the standard normal cumulative distribution and ϕ is the standard normal probability density function. The expected improvement acquisition function works with a balance between choice of points with high variance for exploration and low mean for exploitation [24].

MAXIMUM PROBABILITY OF IMPROVEMENT

Another old approach, presented by Kushner in 1964, maximizes the probability of improvement with respect to $f(x^+)$ defined as:

$$PI(\hat{x}) = P\left(f(\hat{x}) \leqslant f(x^+) - \xi\right) = \Phi\left(\frac{\tilde{\mu}(\hat{x}) - f(x^+) + \xi}{\sigma(\hat{x})}\right) \tag{2.34}$$

This method is more exploitative than expected improvement as points with a high chance of yielding an even slightly lower value of the objective function will be chosen. It is possible to add a decreasing trade-off modification ξ which is not its inherent part. It leads to more exploration in the initial stage of optimization by accepting only improvement bigger than the given parameter ξ. This approach is also possible with expected improvement function to promote more exploration in the beginning of the process [24, 94].

ENTROPY SEARCH

Alternatively the entropy search method can be utilized. Its main aim is minimization of uncertainty of the optimal value x_*. Having obtained the posterior distribution for the location x_* which is $p(x_*|D)$ one wants to select the next probing point $\hat{x}$ so that the reduction in negative differential entropy is maximized [54, 56]. The acquisition function looks as follows:

$$\alpha(x) = H\left[p(x_*|D)\right] - \mathbb{E}\left[H\left[p\left(x_*|D, x, f(x)\right)\right]\right] \tag{2.35}$$

Where D is the previous observation set and $H\left[p(x)\right] = -\int p(x)\log p(x)dx$ is the argument's differential entropy [56]

Evaluation of equation (2.35) is tough due to entropy computations not being analytical as well as due to the necessity of evaluation of $p(x_*|D)$ for multiple points at every iteration [56]. Rather complicated approximations are required and for details the source articles should be checked [54, 56]. Wang and Jegelka [156] suggest that entropy search algorithm tend to be inefficient in multi-dimensional analyses as evaluation of a large number of samples may be required. For this reason as well as the aforementioned complexity of the method it is not utilized in this project.

CONFIDENCE BOUND

The last type of acquisition function described is the upper confidence bound algorithm or in the case of minimizing the objective function the lower confidence bound. It implicitly utilizes the mean and uncertainty while choosing the next sampling point in order to maximize the exploration and exploitation [24, 33, 140]:

$$\alpha_{\mathrm{LCB}}(x;\beta) = \mu(x) - \beta\sigma(x) \tag{2.36}$$

Where $\beta > 0$ is a trade-off parameter which can decrease with time to smoothly switch from exploration to exploitation and $\sigma(x)$ is the marginal standard deviation of the objective function at x. This method is based on optimism related to uncertainty, meaning that the algorithm will pick the next sampling point which poses a chance of being the minimum based on its mean and uncertainty [24]. Value of the objective is sampled at the chosen point and if it is smaller than the current minimum it becomes the new one and the process is repeated. Choice of higher β coefficient usually leads to higher confidence about finding the global minimum of the objective [33].

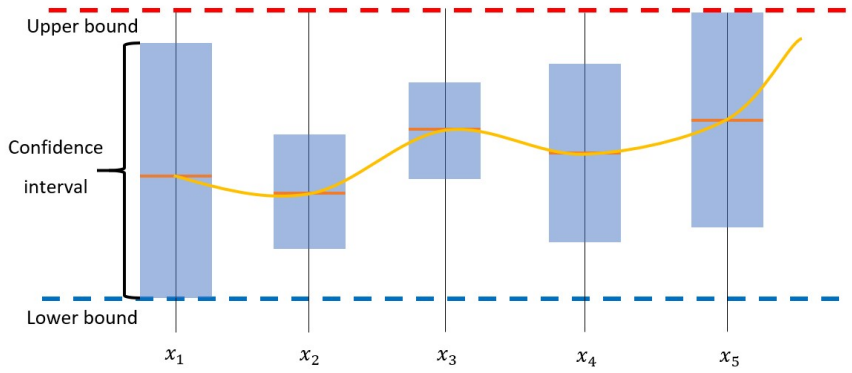

Figure 2.21: Graphical representation of the upper/lower confidence bound

Having chosen the acquisition function one can choose the right framework which allows for the desired optimization properties. Most of them like GpyOpt [4], GPflowOpt [70] or Dragonfly [67] allow for multiple design parameters, bounds imposed on them and use of parameter constraints as well as most or all of the described acquisition functions. Some of the frameworks like Dragonfly [67] allow for multi-objective optimization and some like GPflowOpt [70] allow for imposing black-box constraints on the outcomes.

2.4.4. ARTIFICIAL NEURAL NETWORKS

An approach which complements Gaussian processes in regression, presented in this work, is artificial neural network (ANN) based analysis. Artificial neural networks mimic the human brain, which consists of around 10^{11} neurons that perform the cognitive functions [39]. Such biologically motivated models are based on various networks of processing units (artificial neurons) [132] as shown in Figure 2.22.

In supervised learning, which falls into the scope of this project, data is fed into the system through the input layer and processed within the network until it learns how to map the outputs to the inputs correctly. Finally, the results can be read from the output layer [49, 132]. Some applications of artificial neural networks other than function approximation include: classification, clustering, associative memory, process control and optimization [35, 39].

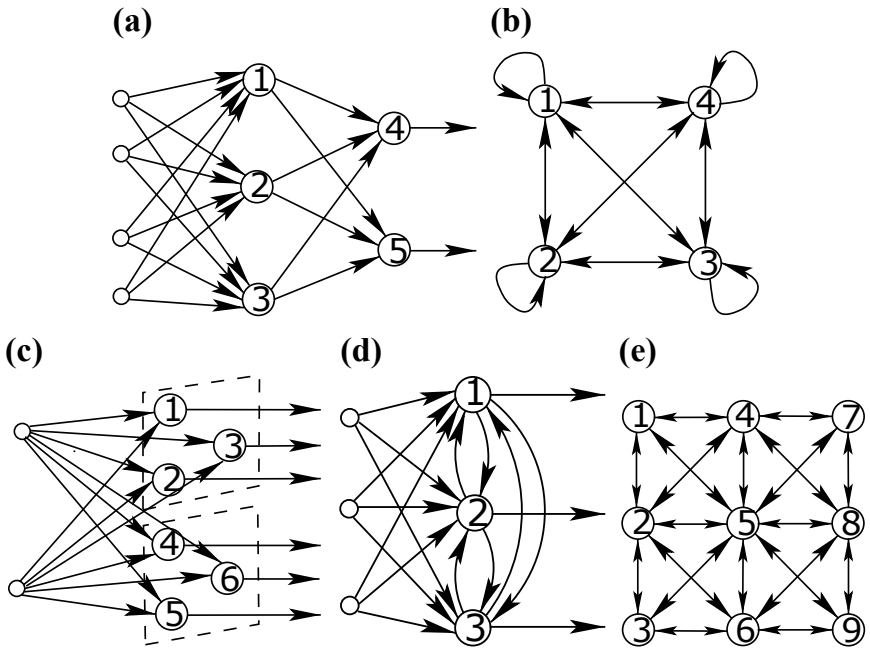

Figure 2.22: Types of neural networks: a) Layered feedforward network, b) Recurrent network, c) two-dimensional lattice network, d) layered feedforward network with lateral connections, e) cellular network. Numbered circles represent neurons and the blank ones depict input nodes [39].

This review focuses on the feedforward networks due to their popularity and simplicity which results from the layered approach and lack of feedback between such layers [39]. Additionally, implementation of this approach in the machine learning software, with Keras Python library [30], was readily available to the author.

Feedforward neural networks are based on information flow, without feedback connections, between the input layer, through the processing layers up to the output layer [48]. The input pairs $(x, f^*(x))$ provide information about the points sampled from a desired function $f^*(x)$ [48]. The model needs to match the output function $f(x)$ with the function $f^*(x)$ as closely as possible, which is quantified with accuracy metrics [39]. Number of layers between the input and output ones defines the depth of the network. Such layers are called the hidden layers because it is not clear on the basis of only the training data what the output of each of them should be [48].

NEURONS

Figure 2.23 depicts a simplified biological neuron which consists of [35, 49]:

- **Dendrites** which bring inputs into the neuron
- **Cell body** which performs the processing of information
- **Axon** which leads the impulse to other neurons
- **Synapses** that connect the neuron with dendrites of other neurons

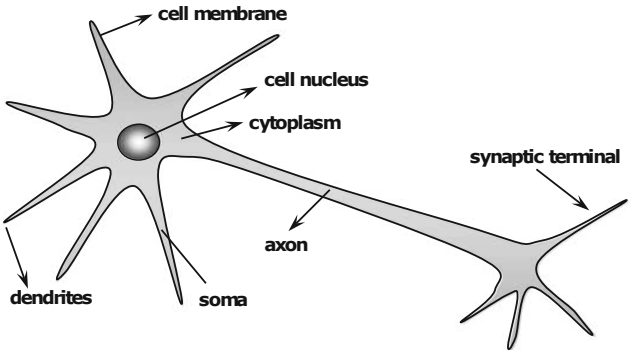

Figure 2.23: Representation of a biological neuron [35]

In artificial neural networks the processing unit can be represented similarly (see Figure 2.24). Inputs $x_1, x_2, ..., x_n$ are weighted with weights $w_1, w_2, ..., w_n$ and summed with a linear aggregator. A bias B is subtracted from the sum in order to set a threshold for signal generation. If the activation potential u expressed by equation (2.37) is non-negative then a signal is generated and further limited by the activation function g to the desired range of values, which becomes the output y [35].

$$u = \sum_{i=1}^{n} (w_i \cdot x_i) - B \tag{2.37}$$

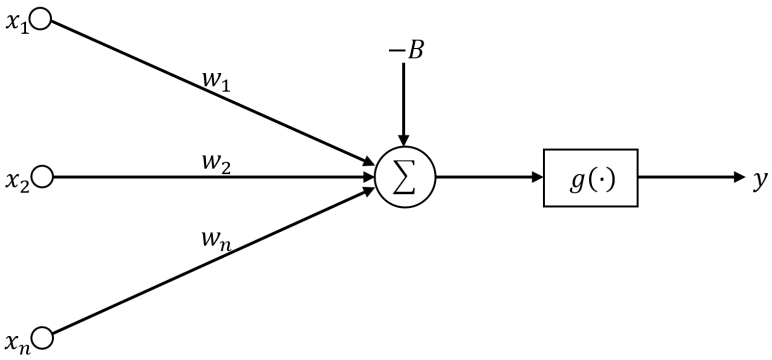

Figure 2.24: Representation of the most frequently used artificial neuron model, proposed by McCulloch and Pitts [35]

TRAINING

Training of feedforward neural networks is based on establishment of a loss function on the output and its minimization which is done by adjustment of the weight and bias values. If the model function is in the form $f(x;\theta)$ with θ being a set of parameters then an exemplary mean squared error loss function J is evaluated on the testing set as [48]:

$$J(\theta) = \frac{1}{4} \sum_{x \in \mathbb{X}} \left(f^*(x) - f(x;\theta) \right)^2 \tag{2.38}$$

The method utilized for minimization of the loss function, which is usually used in neural networks, is the gradient descent [48]. It is based on calculation of the loss function's partial derivatives with respect to the parameters of the last layer and back-propagation over the previous layers until the beginning of the network is reached [97]. Parameters are adjusted according to the following equation which applies to both weight and bias values [132]:

$$\Delta w_{ji} = \eta \sum_{p=1}^{k} \left(\frac{dJ}{dw_{ji}} \right)_p \tag{2.39}$$

Where w_{ji} represents the weight between j^{th} and i^{th} neurons, k is the number of batches and p is the batch counter. η is the learning rate, which can be constant or variable in order to ease achievement of the loss function's minimum [97].

Batch is the number of samples analysed by the network before the parameters are updated [97]. One can split the gradient descent based optimizations of parameters with respect to this quantity as follows [97]:

- **Batch gradient descent** with batch size being equal to the training set size
- **Stochastic gradient descent** with batch size equal to one
- **Mini-batch gradient descent** with batch size which assumes values between one and the size of the training set

According to Goodfellow et al. [48] larger batch sizes lead to more accurate gradient estimates, however if processed in parallel the amount of memory required scales with the batch size. On the other hand small batches often help with regularization (reduction of overfitting) due to the noise they introduce [48] and their use can result in faster learning [97].

The parameter optimization process runs over a set number of epochs, which defines the number of times the algorithm goes through the whole dataset, or until a satisfying convergence is reached [97].

ACTIVATION FUNCTIONS

Activation functions employed in artificial neural networks assume continuous or discontinuous forms and usually map the output into the range $(-1,1)$ or $(0,1)$ [39]. The activation functions can also be split with regards to their differentiability [35] or linearity [103]. Their choice affects how the hidden layer values are calculated and how much information can be gained during training [48]. The weighted sum along with the bias processed by each neuron give an output linear in nature. For this reason, if a non-linear final output is expected, then such non-linearity needs to be introduced with the activation functions [103].

The first, partially differentiable function, is the heaviside function which assumes the value of 1 if the activation potential is positive and a value of 0 if it is negative [35, 133]:

$$g(u) = \begin{cases} 1 & \text{if} \quad u \geq 0 \\ 0 & \text{if} \quad u < 0 \end{cases} \tag{2.40}$$

This function is the simplest activation function in existence, however, its use is limited to equally uncomplicated applications like binary classifiers due to the zero gradient which affects the back-propagation [133].

In the group of functions whose first derivative exists in the whole domain one can find the popular: linear function, logistic function, hyperbolic tangent and rectified linear unit function (ReLU) [35, 39].

The simplest, linear function assumes the form [133]:

$$g(u) = au \tag{2.41}$$

Where a denotes the gradient. Such a function due to its simplicity can be fit quickly and reliably, however, use of linear models is limited to modelling linear functions only [48]. Additionally, the network based on linear functions can not improve the error in the next iterations due to a constant gradient [133].

The logistic and hyperbolic functions assume values from ranges $(0,1)$ and $(-1,1)$ respectively and belong to the group of nonlinear activation functions [35]. The former one is represented as [35]:

$$g(u) = \frac{1}{1+e^{-\beta \cdot u}} \tag{2.42}$$

And the latter as [35]:

$$g(u) = \frac{1-e^{-\beta \cdot u}}{1+e^{-\beta \cdot u}} \tag{2.43}$$

Where β is a real constant related to the slope at the function's inflection point [35].

The sigmoid function is an easy to understand function, which is mostly used in shallow networks in applications like binary classification problems and modelling logistic regression [103]. The basic version of the sigmoid function suffers from gradient saturation and slow convergence [48] which make it unlikely to be used.

The hyperbolic tangent activation function tends to be easier to train and shows better performance in multi-layer networks than the sigmoid function [103]. It is also zero-centred, unlike the sigmoid function, which helps with the back-propagation [103, 133].

The last and most important activation function described is the rectified linear unit (ReLU), which is defined as:

$$g(u) = max(0, x) \tag{2.44}$$

It is recommended for use in majority of feedforward neural networks [48]. Its closeness to linearity allows for easy optimization with gradient descent methods [48]. Additionally, its use results in better generalization and performance than in the case of using sigmoid or hyperbolic tangent functions [103]. However, one needs to pay attention to overfitting and neuron death, which happens if a neuron outputs zero for any input, while using this function [103]. Some softwares offer improved versions of this function in the form of Leaky ReLU which alleviates some of the disadvantages [48].

3

DESIGN AND DATA-DRIVEN ANALYSIS

A successful analysis relies on preparation of the right framework. The one utilized in this project is based on previous work done by Bessa and Glowacki [13, 45] and extended by addition of a Bayesian optimization module. The first part consists of a data - driven examination of parameters which affect the performance of the investigated smart structure. Their importance and bounds to be imposed on the optimization problem are determined with the use of sensitivity analysis and design space projections. Additionally, trends in behaviour are analysed with the help of regression models which describe the quantities of interest. The optimization step (described in Chapter 4) on the other hand leads to choosing values which describe the design whose behaviour matches the reference performance in the closest way.

This chapter describes the idea behind the designed structure and steps of its development as well as parametric approach towards the geometry in Section 3.1, introduction to the data-driven analysis in Section 3.2 and its results in Section 3.3. It is also concluded with optimization of the data-driven model (Subsection 3.3.3) which could be used for designing an optimal VAD with configuration that matches prescribed constraints without the need for additional FEM simulations.

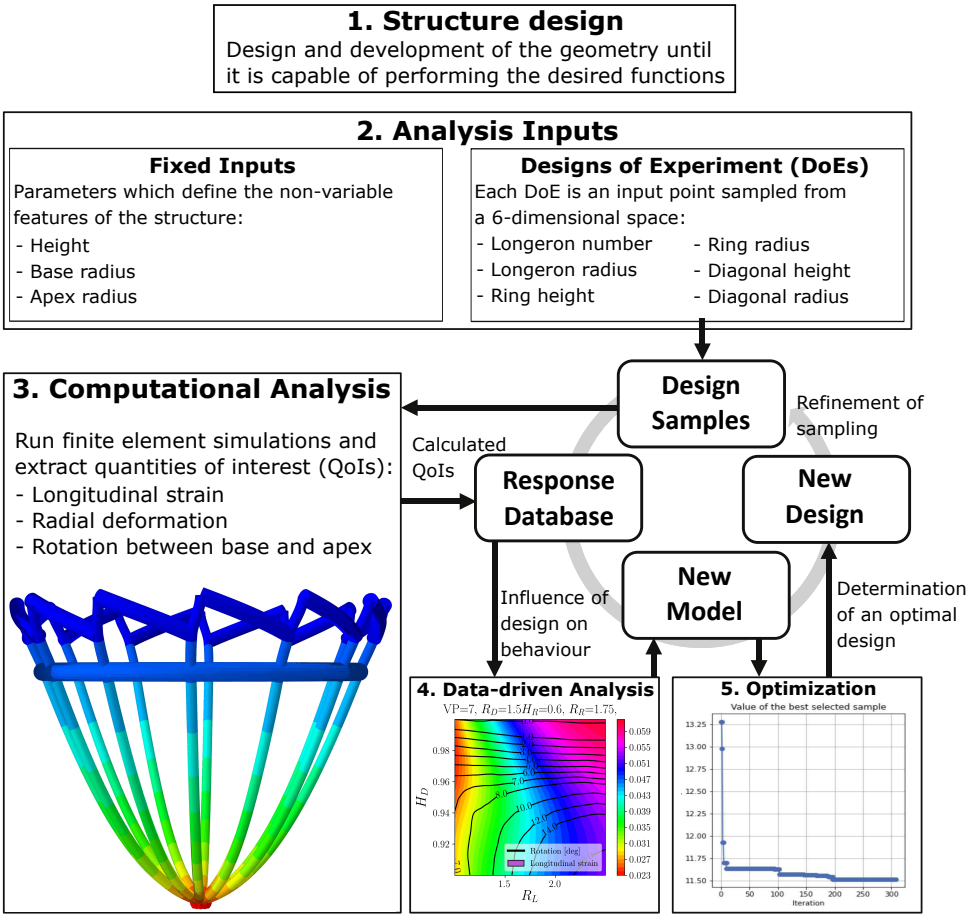

Figure 3.1: Framework visualisation adapted from [15]

3.1. MAGNETOACTIVE VENTRICULAR ASSIST DEVICE

The investigated, metamaterial based, myocardium supporting structure is a result of three months of iterations and redesigning the starting geometry in order to achieve the expected functionality. Development of the novel structure can be seen on the right side of Figure 3.4 and starts with the initial supercompressible, but passive metamaterial [14]. As described in Section 2.1 the choice of metamaterial developed by Bessa et al. [14] was motivated by the possibility of its adjustment to heart's shape and inclusion of elements which can perform the required squeezing motion.

The following step includes addition of diagonal elements, attached to the rigid base and the longerons. They proved to be successful in inducing rotation and vertical strain when contracted as they bend longerons to the side and down to an extent defined by the height of attachment. In structures designed by Roche et al. [118, 119] (on the left

side of Figure 3.4), which act as a reference, the rotation is induced by contractive motion of angled pneumatic muscles. In the case of the described, magnetically actuated device, induction of longerons' contraction would only be possible with one of the methods described below - field inducing coils wrapped around them. In order not to limit the possibilities at this stage, before feasibility of both proposed solutions is practically examined, the universal design with diagonal elements was chosen.

The final design, visible in Figure 3.5, inspired by devices researched by Roche et al. [118, 119], incorporates the diagonal elements concept. Vertical elements (longerons) have a shape that matches that of a human heart and can be described by an exponential function derived on the basis of geometrical dimensions presented by Roche et al. [119]. They are held together by an active, compressive ring, which causes radial compression, and diagonals capable of shortening and inducing rotation within the structure. With longerons fixed at the top, as shown in Figure 3.7, the actuation results in the ring pulling the longerons towards the centre of the structure and their tips move upwards which is perceived as longitudinal and radial deformations respectively. Simultaneously, diagonals pull on the longerons sideways which causes the twist between the apex and base planes. The investigated metamaterial structure forms an active scaffolding of the desired device. For application inside a human body and uniform strain application to myocardium it would have to be encompassed by an elastic sleeve at a later stage of development.

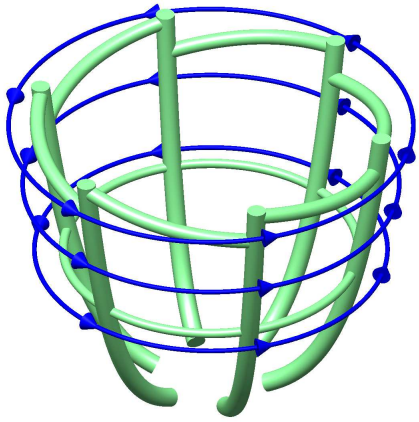

Figure 3.2: Visualisation of the circular field based mode of actuation (magnetic field direction in blue)

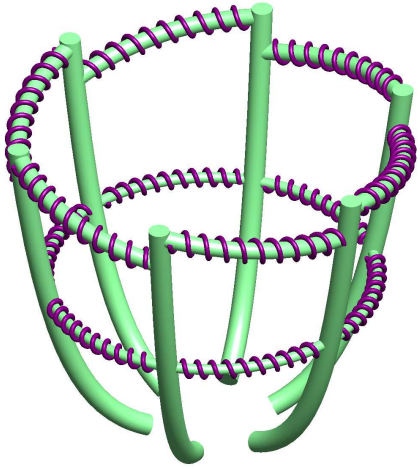

Figure 3.3: Visualisation of the device's configuration with field inducing coils (in purple)

All elements have a circular cross-section for simplicity of design and ease of modelling. At this stage all joints within the structure are treated as compliant (as opposed to hinges) due to the expected manufacturing process choice being 3D printing. The device would be custom designed and made for every patient. Hence, 3D printing was chosen for its capability of building complex-shaped structures without the need of long machine adjustments to accommodate a new geometry. The material chosen for the device (polycaprolactone doped with 20% of $rGO - Fe_3O_4$) is printable, which makes this process a suitable solution.

The structure can potentially be activated magnetically by application of fields in the directions of the ring and the diagonals. The exact activation mechanism design is beyond the scope of this thesis, however, two ideas were considered:

- **Field inducing vest** which would create a circular magnetic field inside patient's chest, in the direction of the ring and closely matching the direction of slightly inclined diagonals (see Figure 3.2)
- **Compliant, insulated coils around the ring and diagonals** which could be powered across the skin through an induction based circuit or temporarily from an internal battery (see Figure 3.3)

The main advantage of the first solution is the minimal number of parts implanted into patient's body, which may cause pain if they occupy excessive space [52]. The magnetic vest would, however, be highly inconvenient in everyday life so its use would mostly be restricted to bridge therapies on the way to a transplant. The second approach would allow for more versatility in its applications. An external exchangeable and an internal rechargeable batteries could be used in order to provide a full-time heart support to the patient. Additionally, the magnetic field would be applied locally to the device instead of the whole chest, especially if the device is shielded. This would result in more precise field application to the active elements and its lower influence on human body. What may become prohibitive is the size and number of parts which would have to be implanted in order to power the device.

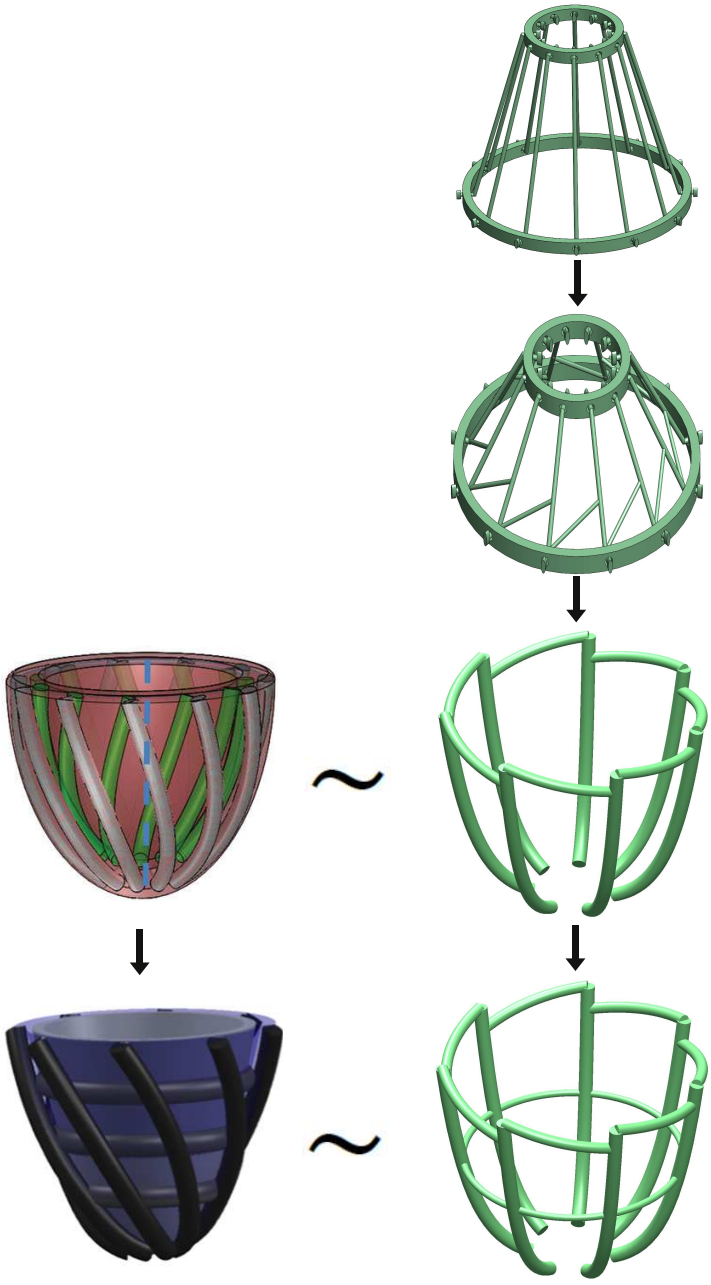

Figure 3.4: Development steps of the final geometry (Initial geometry (top right) [14], other designs on the left [118, 119])

3.1.1. PARAMETRIZATION

Each configuration of the device is described as a separate Design of Experiment (DoE). Every DoE is a result of sampling 6 variables which, along with the fixed features, fully define the geometry. The variable parameters (as presented in Figure 3.5) include:

- Height of ring attachment normalized by structure's height $\boldsymbol{H_R}$
- Height of diagonal attachment normalized by structure's height $\boldsymbol{H_D}$
- Radius of the longerons $\boldsymbol{R_L}$
- Radius of the diagonals $\boldsymbol{R_D}$
- Radius of the ring $\boldsymbol{R_R}$
- Number of longerons $\boldsymbol{Polygon}$

Choice of bounds for each of them was based on similar devices designed by Roche et al. [118, 119] as well as a considerable number of design iterations which led to conclusions about the geometrical limitations. Yet, the choice is not believed to be final and may be subject to change when progress is made in manufacturing and testing the first samples.

Number of longerons used by Roche et al. in their design was 7 [119] or 8 [118]. This parameter affects the sturdiness of the structure to the highest extent so the minimum number of longerons was set at 6 and maximum at 12. Height of diagonal attachment points was chosen so that the angle between the circular magnetic field in the ring's direction and the diagonals does not become highly significant. The ring was "mounted" at various heights between the very bottom of the device and close proximity of the diagonals. Radii of all elements were picked so that they do not clash with each other, in an undeformed configuration, on the basis of pre-design iterations. All variables are continuous between their bounds apart from the number of longerons which is discrete.

Table 3.1: Bounds of design parameters

Parameter	H_R	H_D	R_L	R_D	R_R	$Polygon$
Lower Bound	0.1	0.9	1 mm	1 mm	1 mm	6
Upper Bound	0.8	1	2.5 mm	2.5 mm	2.5 mm	12

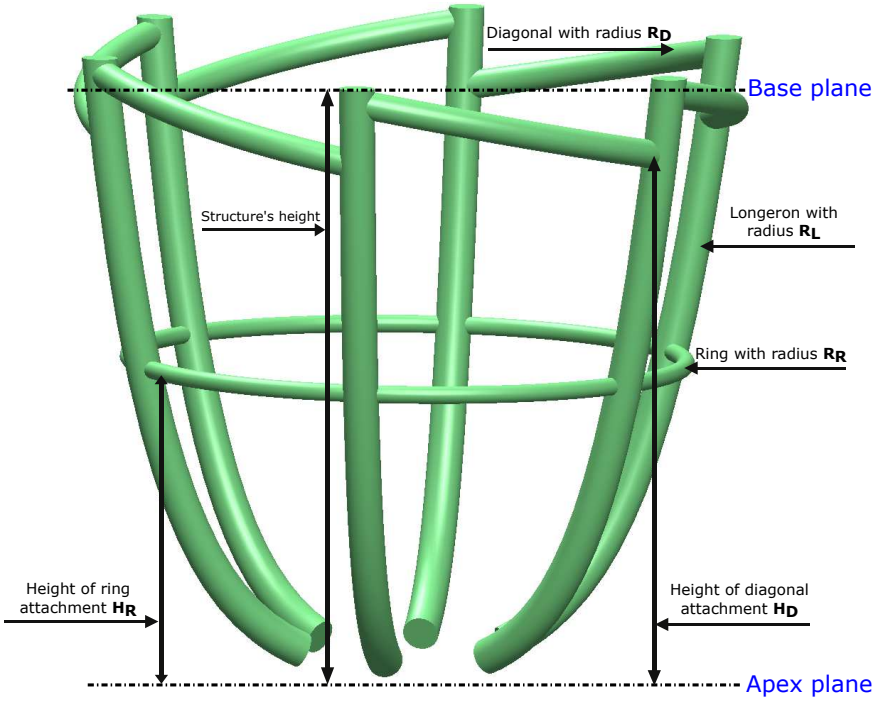

Figure 3.5: Parametrization of the cardiac sleeve design

In this analysis the shape of the structure fits the size of an adult's heart [119]. It can, however be tailored or scaled with the values, currently fixed at:

- **Apex radius**: 12 mm
- **Base radius**: 37 mm
- **Height of the structure**: 71mm

Additionally to fixing the radii and height of the structure, the material properties were set constant throughout the analysis. Doped PCL was used for the magnetically active elements and longerons were "made" of pure PCL unaffected by the magnetic field. Properties of both are presented in Table 3.2. It is possible to analyse the influence of variable material parameters on the structure's behaviour, however, it is beyond the scope of this thesis and is recommended as a potential material development stage.

Table 3.2: Properties of the materials used in the analysis

Property	PCL + 20%$rGO - Fe_3O_4$	Pure PCL
Young's modulus [MPa]	405	363.3
Poisson's ratio	0.3	0.3
Maximal strain [%]	10	0

3.2. ANALYSIS

Having reached the final parametrized design of the structure, its data-driven performance quantification is performed on the basis of 50000 datapoints obtained with FEM simulations. As described in Figure 3.1, each datapoint represents a separate DoE with a unique geometrical configuration based on the variable parameters sampled from the domain presented in Table 3.1 and on the fixed inputs - height and radii of the base and apex. Quantities of interest: longitudinal strain, radial deformation and rotation are extracted from each simulation and saved to a database, which acts as a source of information for training the performance predicting models.

3.2.1. FINITE ELEMENT SIMULATIONS

Similarly to analyses done by Bessa [13] and Glowacki [45], as the same kind of framework is used, the design of experiment (DoE) sampling is done with Sobol sequence [139]. This approach generates sequences of points in the multidimensional hypercube in a manner which fills it with high "evenness" and allows for a better description of the design space [124]. An example can be seen in Figure 3.6 where Sobol sequence is compared with random sampling.

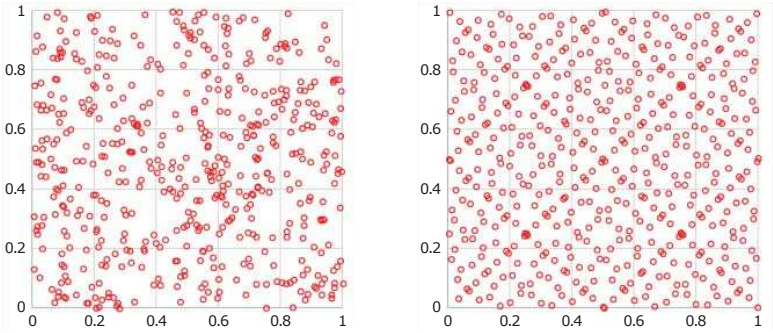

Figure 3.6: Random sampling (left) comparison against Sobol sequence (right) [124]

Analysis of each DoE is performed with Finite Element Method (FEM) implicit static simulations in which a predefined local thermal strain is assigned to the diagonal elements and the ring. Such a solution has been used before instead of other activation modes like piezoelectric one [34, 38]. Only the final deformation is crucial and the transient behaviour is beyond the scope of this thesis, hence the thermal model is used to imitate the predefined deformations of the material in a magnetic field. This approach is a major simplification of the analysis which, with more computational power and time available, could potentially be done with electromagnetic simulations. When the magnetic material is fully developed and the exact mode of actuation chosen, the accuracy of the thermal model simplification needs to be validated experimentally.

In the simulations an identical local strain value of 10% is applied to both the ring and diagonals for simplicity and limiting the number of parameters which determine the resultant behaviour. However, both types of active elements (ring and diagonals) are unlikely to deform to the same extent, under the influence of an external circular field, unless their respective doping percentage of $rGO - Fe_3O_4$ is adjusted. As can be seen in Figure 3.2 the field in the direction of the ring would create an angle with the diagonals so a better understanding of the material's behaviour in differently angled magnetic fields is required to determine the feasibility of this mode of activation. The coil-based mechanism seems to be superior in this matter as desired fields can be achieved independently for each element by varying the currents flowing through the coils. Therefore, the coil activation idea justifies the choice of applying identical strains to active elements and the circular field concept can be investigated at further stages of the project.

Quantities of interest in the form of:

- Longitudinal strain
- Radial deformation
- Rotation between the base and apex

are extracted after each simulation and saved to a file. The former two are measured at 26 points along the first longeron and after addition of a symmetrical reflection can be used to display the X-Z plane deformation of the structure like the one seen in Figure 4.1. Relative rotation between the base and apex of the device is quantified on the basis of the first longeron's tip displacement as shown in Figure 3.7.

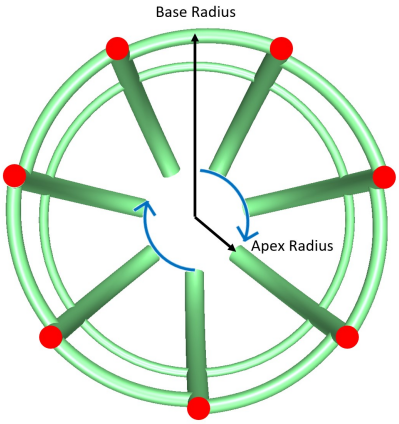

Figure 3.7: Top view of the structure along with fixed feature names, fixed constraints applied to the structure (in red) and direction of rotation (in blue)

The restrictions imposed on the structure are visible in Figure 3.7 in the form of fixed geometry condition at the top of each longeron. This kind of constraints can also be found in the analysis performed by Roche et al. [119] and is critical for the contractive behaviour of the structure.

All elements are modelled as spline beams with a circular cross-section integrated during the analysis, due to their slenderness and considerable deformation during analysis. Mesh test was performed with respect to the three quantities of interest: longitudinal strain, radial deformation at longeron's tip and rotation, which led to setting the beam element's length at 0.074 mm. All quantities are measured with relative inaccuracy lower than 1%. Contact detection is not included in this part of the analysis due to the need of a large dataset for data-driven examination. Use of contact detection in the simulation increases its computation time by a factor of around 50 – 60 which would make the analysis of 50000 datapoints infeasible with the available computational power and time. This approach causes incorporation of designs with clashing longerons,

as shown in Figure 3.16, into design space and makes their rejection impossible at this stage. This issue is solved at the final step of the analysis - Bayesian optimization, where contact detection can be applied due to a lower required number of simulations.

3.2.2. MACHINE LEARNING MODELS

Derivation of trends quantifying the behaviour of the smart structure is the first step of its data-driven analysis and the right machine learning framework is required for it. Similarly to work done by Glowacki [45] in this project the main algorithm utilized is sparse Gaussian process regression (SGPR). It was chosen for its versatility and applicability to various types of behaviour thanks to the non-parametric approach as well as the limited risk of overfitting [23, 115]. Additionally, as described in the literature review, it scales better than the full Gaussian process approach while staying relatively easy to train [85]. This analysis is purely conceptual and contains no geometrical imperfections which results in noiseless, deterministic data. Despite no need for quantification of uncertainty, which is an inherent benefit of Gaussian process approach [115], it is used for its reliable performance in establishing two out of three required models (longitudinal strain and radial deformation) whose nature was unknown before the analysis.

Rotation model is obtained with an artificial neural network due to its superior performance in this application and an ability to model complex relationships, which this one proves to be (see the sensitivity analysis 3.14). It was chosen as a secondary option due to the high risk of overfitting and need for more precise training to avoid it [151]. The training takes longer than in the case of SGPR before the right hyperparameters are found. Application of Bayesian optimization to neural network hyperparameter tuning is a known and widely used approach [138]. Therefore, its use could help produce even more accurate models in a shorter time in the next stages of this project.

All models contain single outputs because neither of the algorithms proved to perform better than the other in all cases at once and because of complications which a double output Gaussian process method would bring. Multiple output Gaussian processes are useful in applications like sensors, where missing signals can be predicted due to modelled correlation between outputs [90]. Such solutions, however, require additional steps like the use of full covariance matrices which leads to poor scaling $\mathcal{O}(n^3D^3)$ with n being the number of datapoints and D being the number of outputs [90]. Alternatively, Gaussian processes can be modelled as white noise sources with the use of smooth parametrized kernels [23] or approximations to the coupled covariance matrix can be made [90]. The project did not include creation of multiple output Gaussian process models for simplicity. The two single models were also deemed sufficient for analysis of trends in quantities of interest. Obtaining a model which includes correlations between the outputs could, however, result in its better performance [90].

For simplicity the comparison of machine learning models was done only for Sparse Gaussian process regression (SGPR) and artificial neural network models. Other Gaussian process models did not provide any improvement over the SGPR or were infeasible to use in the given time frame as in the case of full Gaussian process regression.

All models, longitudinal strain and radial deformation as well as rotation, were compared with respect to R^2 and mean squared error metrics. Accuracy of the models measured with R^2 coefficient increased as more datapoints were analysed and mean squared error decreased simultaneously as expected. All models fit the test data well and in the case of the longitudinal and radial deformation functions there are few prediction outliers which results in low MSE. The rotation model has a weaker performance in this matter with an average mean squared error of 1.176 which is still expected to be of little significance if potential manufacturing imperfections and the simulation discretization error are taken into consideration. However, if possible, the model should be improved to minimize the difference between the expected and actual rotation by inclusion of more datapoints and better hyperparameter tuning. More information on model performance is provided in Appendix A.

Table 3.3: Model accuracy and mean squared error. In Longitudinal model strain is considered as fraction of 1, rotation is measured in degrees and the radial deformation is quantified in mm.

Parameter	Longitudinal strain	Rotation	Radial deformation
Accuracy	0.9996	0.9941	0.9997
MSE	$3.273 \cdot 10^{-7}$	1.176	0.0035

The sparse Gaussian process models compared below were obtained with a Matern52 kernel each and the number of inducing points was set at the datapoint number for sets up to a 1000 points and at 1650 for all sets bigger than that due to GPU memory limitation. The hyperparameters were optimized with Scipy optimizer [154] over 2000 iterations with the L-BFGS-B algorithm, which is suitable for large, nonlinear and optionally unconstrained problems when limited memory is available [172]. The artificial neural networks (NN) were trained with ReLu activation function and 4 sequential layers with 350 neurons in each of them. Inclusion of more layers and neurons led to worse performance of the model, most likely due to overfitting. Adam optimizer was used for 500 epochs with a learning step of 0.0005 and a batch size of 5000. All final models were obtained for cases with 80% of data being used for training and 20% for testing which corresponds to approximately 40000 datapoints and 10000 datapoints respectively.

The disproportion in artificial neural network models' performance, in the case of the simpler longitudinal and radial behaviours, is most likely associated with the overfitting and could potentially be improved at least partially with optimization of the hyperparameters. This was, however not done as the performance of Gaussian processes was deemed sufficient for longitudinal and radial deformation and the potential gain in NN models' accuracy would not justify the additional effort required at this stage. NN hyperparameters for the rotation model, where the SGPR model lacked, were chosen iteratively by varying the number of neurons and hidden layers to maximize performance. A single model with multiple outputs, based on either SGPR or NN, would be much simpler to use and should be obtained for the final design if possible and computationally feasible.

LONGITUDINAL STRAIN MODEL

For the final longitudinal strain quantification sparse Gaussian process regression with 80% of training points and around 4.4% inducing/training points ratio was used. When all of the 50000 datapoints were used the Neural Network algorithm resulted in similar model accuracy but strongly lacked in terms of average error (over 1 order of magnitude of difference) as shown in Figure 3.8 and Figure 3.9 respectively. This quantity of interest seemed to be the easiest one to predict with the use of SGPR as the accuracy of the model was close to 1 even with smaller datasets and MSE would still be acceptable at the level of 10^{-5} obtained with 500 datapoints. This would, however not be recommended as a good predictor for the whole design space as such a model was only tested on 100-400 datapoints.

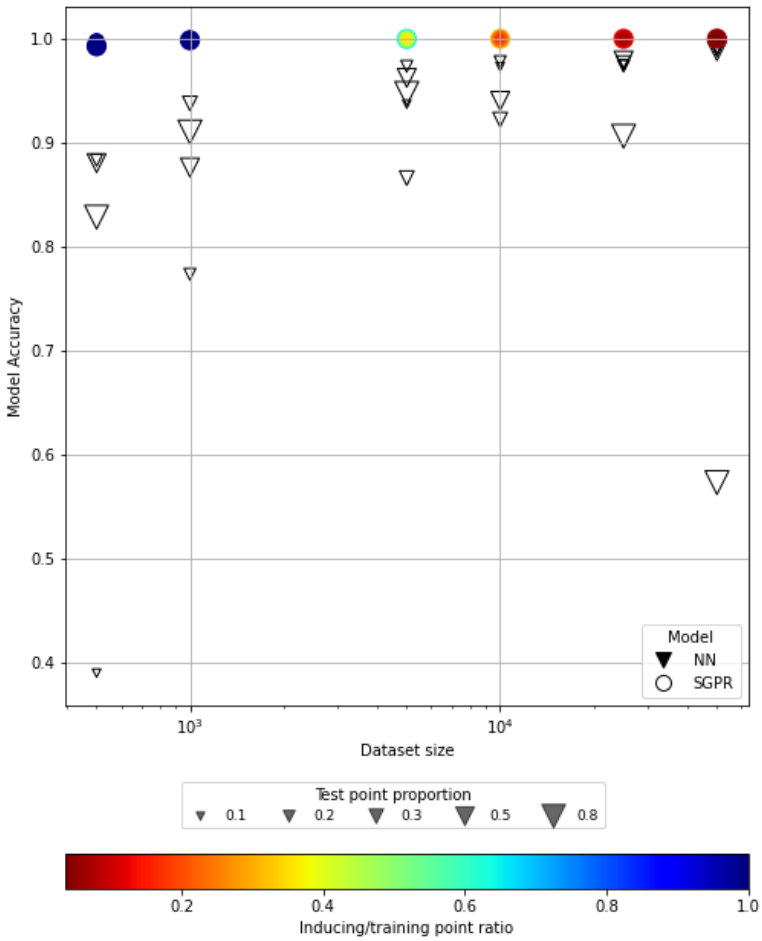

Figure 3.8: Accuracy of the longitudinal strain data-driven model plotted against dataset size with inclusion of inducing to training points ratio for Gaussian process regression

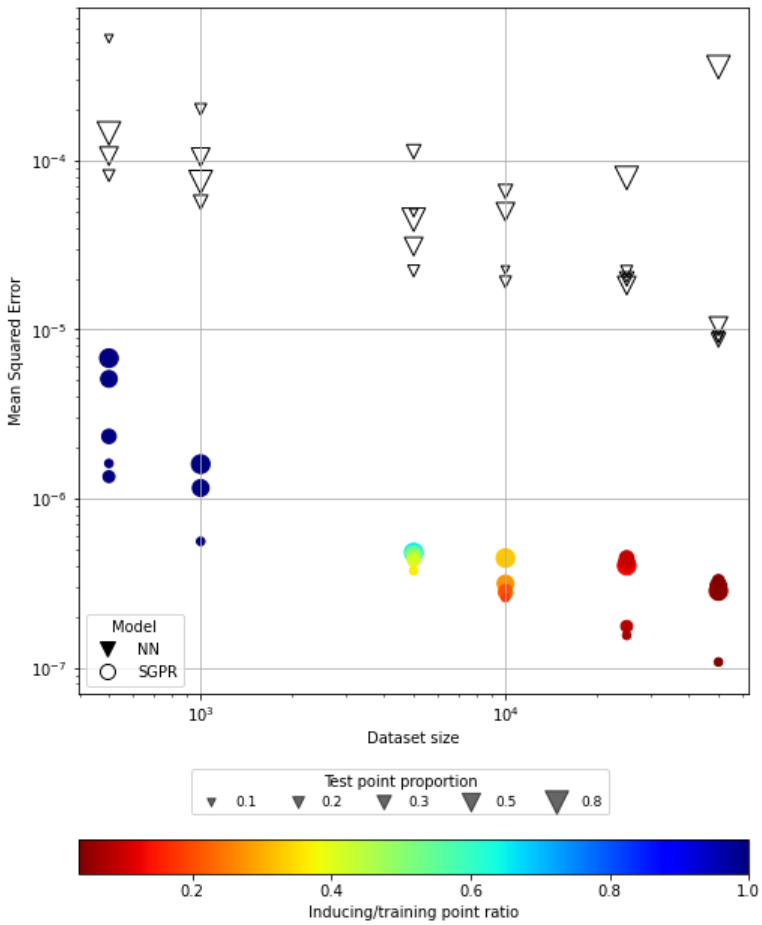

Figure 3.9: Mean Squared error in the longitudinal strain data-driven model plotted against dataset size with inclusion of inducing to training points ratio for Gaussian process regression

RADIAL DEFORMATION MODEL

Radial deformation model comparison showed a slight increase in model accuracy when larger datasets were used for both SGPR and NN with the latter one scoring significantly lower (see Figure 3.10). It can still be seen that lower test point proportion increases accuracy, as expected.

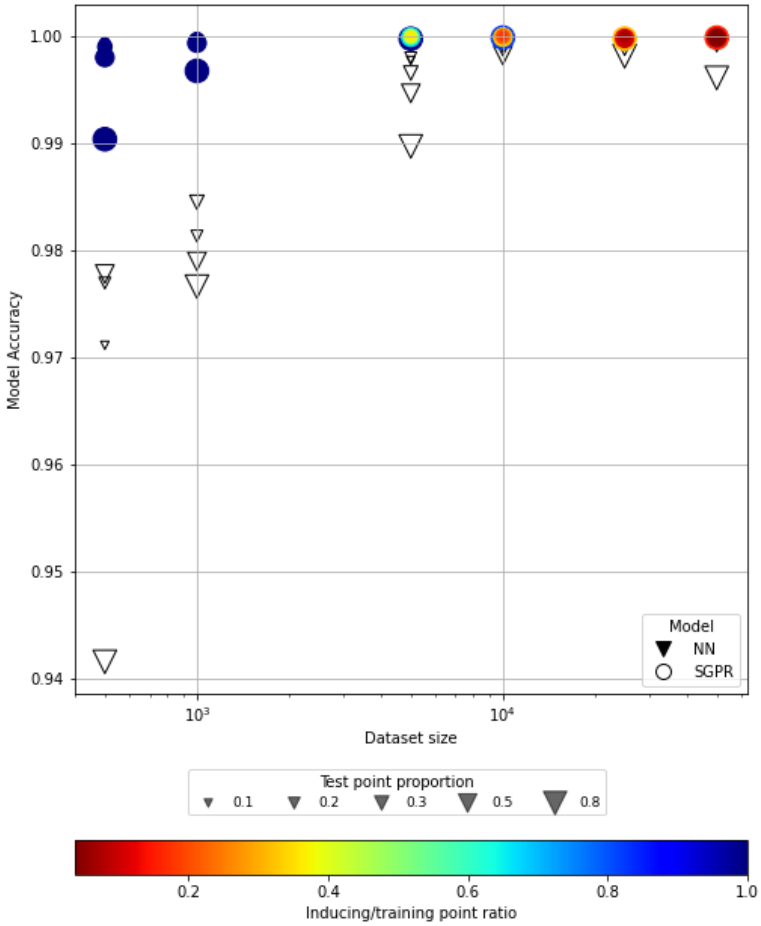

Figure 3.10: Accuracy of the radial deformation data-driven model plotted against dataset size with inclusion of inducing to training points ratio for Gaussian process regression

The radial deformation MSE plot (Figure 3.11) shows an almost equally strong disproportion in performance as in the longitudinal strain case, however, for the largest dataset the NN algorithm obtains just a slightly worse error than SGPR for the case when test point proportion is 20%. The 10% test point proportion samples are disregarded as too small and are included only for trend prediction purposes. According to Figure 3.11 the model obtained with SGPR at 20% of testing point proportion and with 25000 datapoints overall has a lower MSE than the one obtained with 50000 datapoints. The latter one was still chosen due to the fact that its performance was evaluated on a twice higher number of testing points leading to more certainty about the results.

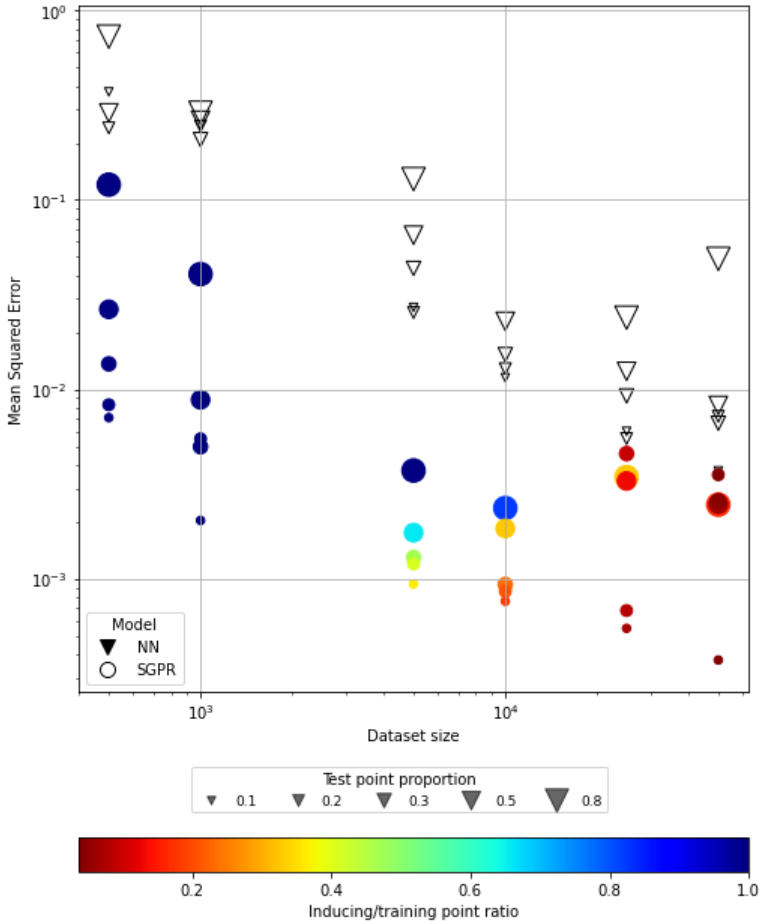

Figure 3.11: Mean Squared error in the radial deformation data-driven model plotted against dataset size with inclusion of inducing to training points ratio for Gaussian process regression

ROTATION MODEL

Rotation between the base and apex of the smart structure is the most complicated model as shown by the increase in accuracy when more datapoints are used (see Figure 3.12. Only at 10000 datapoints the NN algorithm starts to perform better than SGPR. Both machine learning techniques show a significant increase in accuracy, however NN algorithm performs visibly better at the maximal dataset size.

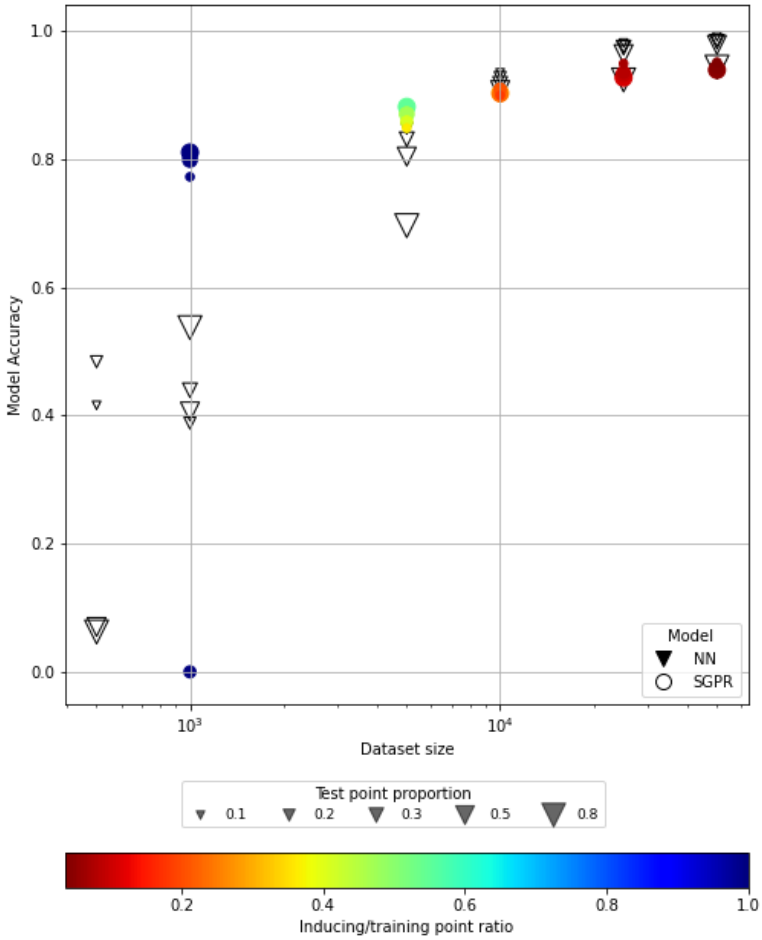

Figure 3.12: Accuracy of the rotation data-driven model plotted against dataset size with inclusion of inducing to training points ratio for Gaussian process regression

In terms of error both SGPR and NN show a decline as the dataset size increases with the gradient of decline being being visibly stronger in the case of neural network which again outperforms SGPR with datasets bigger than 10000 samples (see Figure 3.13). Finally, the artificial neural network algorithm is chosen to model rotation of the material under activation.

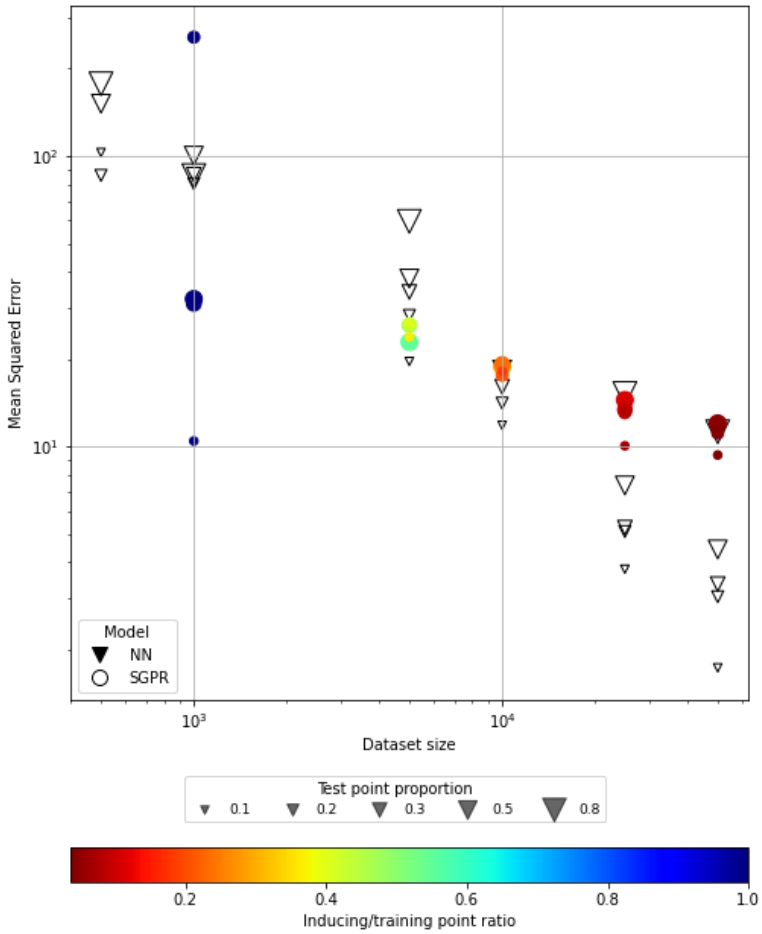

Figure 3.13: Mean Squared error in the rotation data-driven model plotted against dataset size with inclusion of inducing to training points ratio for Gaussian process regression

3.3. RESULTS

This section contains a description of the data-driven analysis results including general trends in the behaviour of the smart structure and explanation of optimization parameters choice based on sensitivity analysis. As described in subsection 3.1.1 the full geometry was described with three fixed and six variable parameters whose influence on the VAD's performance was analysed.

The results presented in this section give an indication of how to find configurations of the device which performs specific functions. With the use of the three machine learning models, without any additional simulations, one can find a design which gives specific longitudinal strain, radial deformation or which twists to a specific extent. This section is concluded with a sample optimization of the model for longitudinal strain with chosen constraints as described later in subsection 3.3.3.

3.3.1. SENSITIVITY ANALYSIS

Sensitivity analysis is a process which can be defined as:

Definition of Sensitivity analysis: *The study of how uncertainty in the output of a model (numerical or otherwise) can be apportioned to different sources of uncertainty in the model input [122].*

In this work it is used to determine the most crucial parameters to represent in the form of design space projections and to make the understanding of the relationships between them and the outputs easier. Additionally, it suggests which parameters should be variable in Bayesian optimization and which could be fixed in order to save time by limiting the computational requirements.

Sensitivity of the output to each of the inputs can be quantified with an index of value between 0 and 1. Such exist in three basic types [123]

- **First order indices** which measure the independent contribution towards variance of the output caused by the given input
- **Second order indices** which measure the combined contribution towards variance of the output caused by a combination of two inputs
- **Total order indices** which measure the total contribution towards output's variance caused by the given inputs

The library used for sensitivity analysis in this project is SALib. It operates in four steps which include the previously developed machine learning models [55]:

- Determination of parameters and their ranges
- Generation of inputs with Saltelli sample function [121]
- Evaluation of outputs at the given inputs with the use of regression models
- Computation of sensitivity indices on the basis of inputs and outputs

Such a sensitivity analysis could potentially be done on the initial datapoints without inclusion of data-driven models for prediction, however the initial Sobol sequence is discontinuous because of several simulation failures. Figure 3.14 presents the results with inclusion of 95% uncertainty confidence intervals.

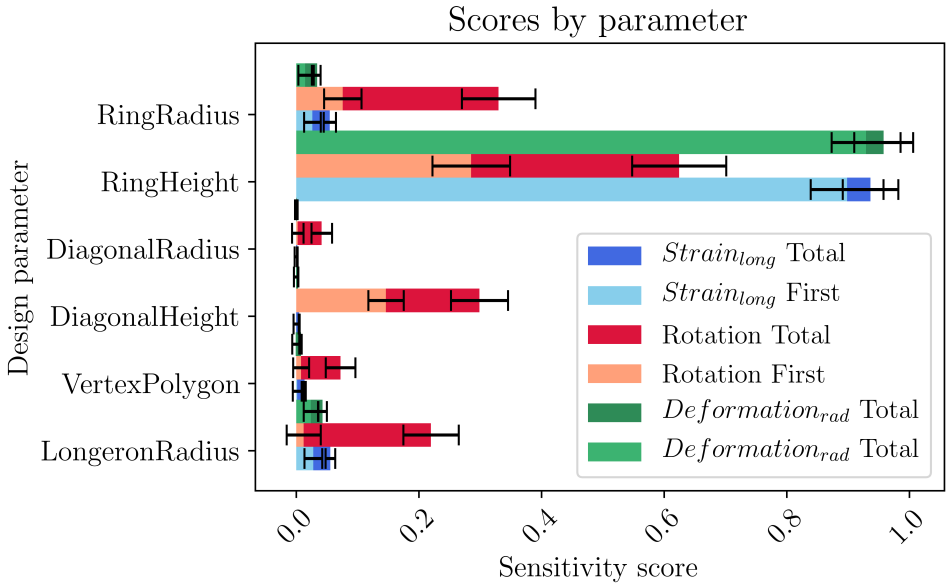

Figure 3.14: Sensitivity analysis performed with SALib [55] library on all three models: longitudinal strain, radial deformation and rotation

It can be seen that most of all longitudinal, radial and rotational behaviour of the smart structure can be explained with positioning of the ring at various heights. This element causes the inward motion of the longerons and its mounting height defines the extent of the radial deformation. Ring's compression is the main driver for the longitudinal strain and a partial one for rotation. As much as ring height is the most crucial parameter for the first two quantities of interest, which accounts for most of their amplitude, rotation also strongly depends on radius of the ring, height at which the diagonals are attached and radius of the longerons. Height of the diagonal attachment defines the extent to which longerons are pulled sideways which is perceived as their rotation. Thicknesses of the ring and longerons affect the stiffness of each of these elements and influence the extent and, as shown in Subsection 3.3.2, the way in which longerons deform. Judging by the results of the sensitivity analysis it can be said that all parameters affect the rotation of the structure to a visible extent. The longitudinal strain and radial deformation behaviours are also influenced to some degree by the ring and longeron radii for the same aforementioned reasons. On the other hand, the radius and height of diagonals as well as the number of longerons barely affect them.

3.3.2. DESIGN SPACE PROJECTIONS

Sensitivity analysis described above allowed for determination of the most crucial parameters in both models. Similarly the Automatic Relevance Determination (ARD) [129] lengthscales of the kernels were checked to conclude what the variability of strain/rotation functions is as specific parameters are changed (see table 3.4). Longitudinal strain model lengthscales indicate significant differences in variability of the output with regards to the parameters. As expected, it mostly changes as height of the ring and radius of the longerons are altered, it is also affected the least by the radius of the diagonal. Radial deformation varies in all dimensions visibly as suggested by the generally low lengthscales. As confirmed by the sensitivity analysis the height of the ring affects it the most and radius of the diagonal the least, however all the other parameters influence the stiffness of the structure and also contribute to some changes in radial strain. Lengthscales for the rotation model are not available as it was obtained with artificial neural networks instead of sparse Gaussian process regression.

Table 3.4: ARD Lengthscales for longitudinal and radial strain models

Parameter	R_L	$Polygon$	H_D	R_D	H_R	R_R
Longitudinal	46.5	131.1	67.0	142.5	28.7	70.5
Radial	8.8	24.8	13.0	25.9	5.7	14.3

Out of the three components of the structure's behaviour two are represented in the form of design space projections - longitudinal strain and rotation. This is due to the fact that they are single output quantities of interest while the radial deformation is more complex and is measured at 26 points along the first longeron. So, even though the radial deformation data-driven model is solely based on the displacement of the first longeron's tip, a decision was taken to analyse the radial compression in the form of X-Z plane cross-sections of the configurations of interest.

Figure 3.15 shows trends in mean longitudinal strain and rotation as the three most crucial parameters are varied: radius and height of the ring as well as the longeron's radius. It can be observed that radius of the ring only slightly influences the longitudinal strain for low longeron radii and as they increase its influence diminishes even further. This can be explained by increasing stiffness of the structure coming from larger longeron's radius and therefore decreasing impact of ring's size on how much it can squeeze the material. Height of the ring invariably influences the longitudinal strain as it is the main driver for deformation of the structure; the higher the ring is placed the more strain can be expected (see Figures 3.16 and 3.17). It is worth noting that the minimal and maximal strains achievable barely change between structures with different longeron radii but for the thicker ones the high strain region occupies a larger area of the design space. This may again be due to the stiffness of the longerons which, if thicker, do not bend locally but rather deform as whole entities when squeezed (see Figures 3.18 and 3.19).

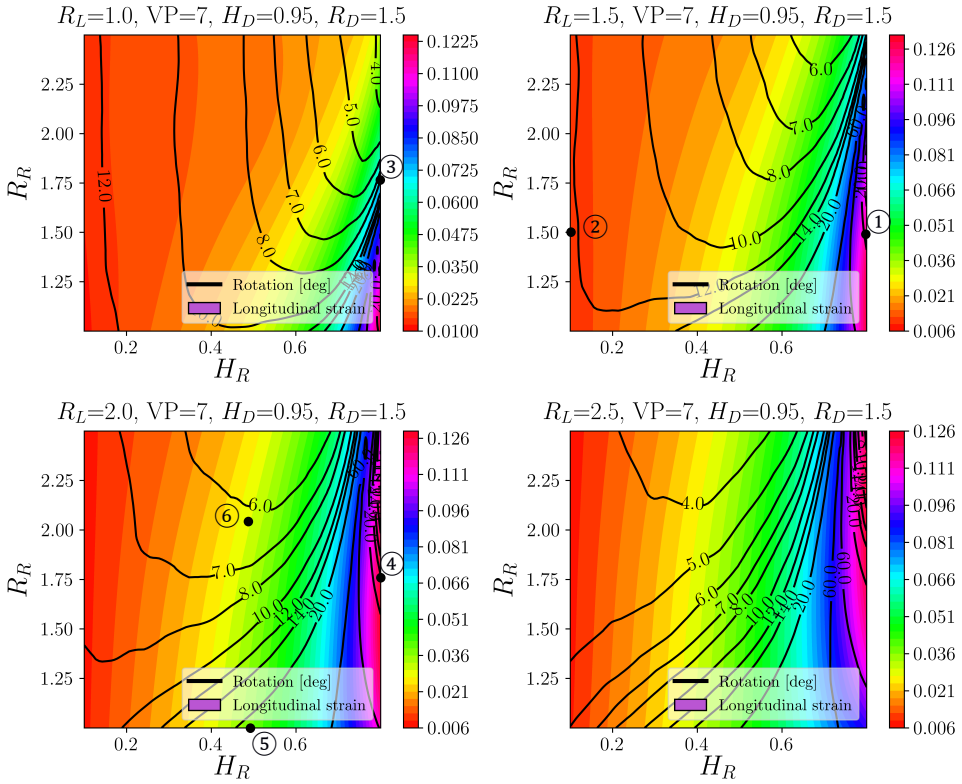

Figure 3.15: Mean longitudinal strain and rotation values presented as functions of ring height, ring radius and longeron radius. Included numbers refer to designs shown in Figures 3.16 - 3.23.

The shape of the rotation contours depends strongly on both radius and position of the ring with the influence of the former one increasing as the radius of the longerons is increased. Height of the ring plays a significant role in causing the rotation and for thicker longerons the general trend of the rotation can be described as increasing with increasing the ring's height. In configurations with thin longerons and low positioned ring tangential bending of the central part of the device can be observed, as shown in Figure 3.20. which leads to little rotation as longeron tips are constrained. In the case of highly positioned ring (see Figure 3.21) longerons are bent close to the base of the structure and the ring keeps their bottom parts straight which leads to significant rotation between the base and the apex. Thickness of the ring (R_R) barely affects the rotation in configurations where it is highly positioned but does influence it when the ring occupies an intermediate position, like in Figures 3.22 and 3.23. The thinner it is the less it contributes to tangential stiffness of the longerons which are in turn easier to pull sideways by the diagonals.

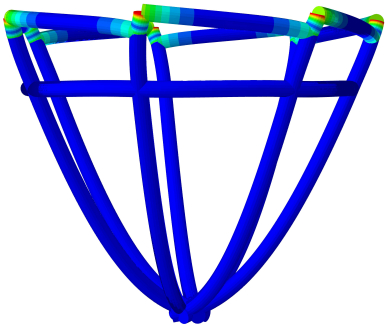

Figure 3.16: Side view of a structure with a highly positioned ring. Configuration corresponds to point 1 in Figure 3.15.

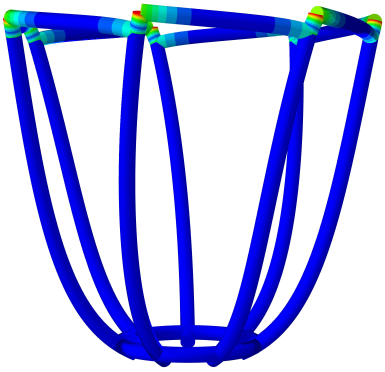

Figure 3.17: Side view of a structure with a low positioned ring. Configuration corresponds to point 2 in Figure 3.15.

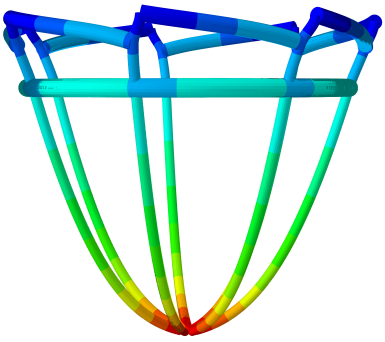

Figure 3.18: Side view of a structure with thin longerons. Configuration corresponds to point 3 in Figure 3.15.

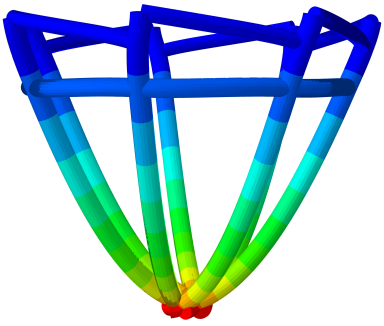

Figure 3.19: Side view of a structure with thick longerons. Configuration corresponds to point 4 in Figure 3.15.

Table 3.5: Configuration parameters for Figures 3.14 - 3.17

Parameter	Figure 3.14	Figure 3.15	Figure 3.16	Figure 3.17
R_L [mm]	1.5	1.5	1.0	2.0
$Polygon$	7	7	7	7
H_D	0.95	0.95	0.95	0.95
R_D [mm]	1.5	1.5	1.5	1.5
H_R	0.8	0.1	0.8	0.8
R_R [mm]	1.5	1.5	1.75	1.75

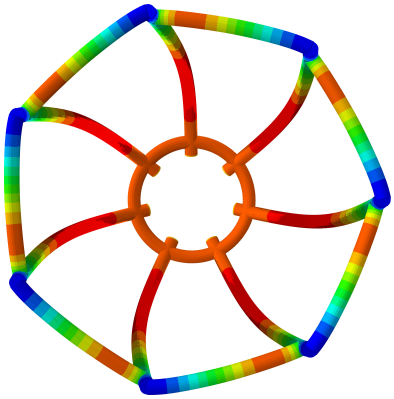

Figure 3.20: Top view of a structure with a low positioned ring. Configuration corresponds to point 2 in Figure 3.15.

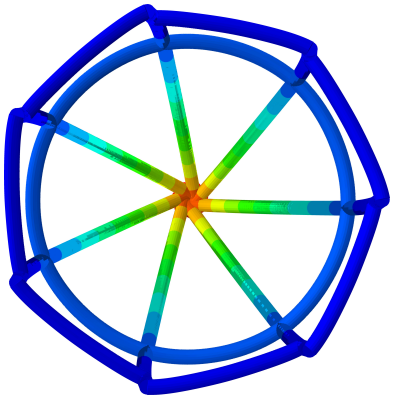

Figure 3.21: Top view of a structure with a highly positioned ring. Configuration corresponds to point 1 in Figure 3.15.

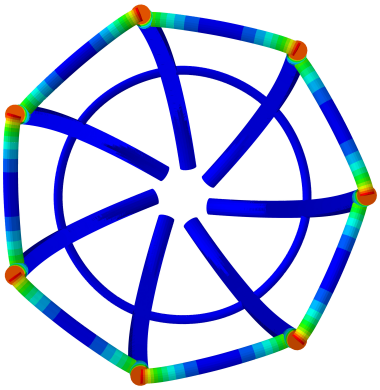

Figure 3.22: Top view of a structure with a thin ring. Configuration corresponds to point 5 in Figure 3.15.

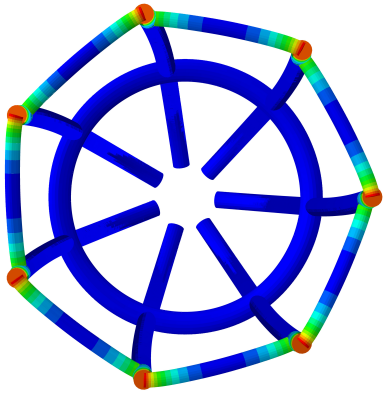

Figure 3.23: Top view of a structure with a thick ring. Configuration corresponds to point 6 in Figure 3.15.

Table 3.6: Configuration parameters for Figures 3.18 - 3.21

Parameter	Figure 3.18	Figure 3.19	Figure 3.20	Figure 3.21
R_L [mm]	1.5	1.5	2.0	2.0
$Polygon$	7	7	7	7
H_D	0.95	0.95	0.95	0.95
R_D [mm]	1.5	1.5	1.5	1.5
H_R	0.1	0.8	0.5	0.5
R_R [mm]	1.5	1.5	1.0	2.0

The next strain and rotation relationships considered are the ones with radius and position of the diagonal as well as position of the ring shown in Figure 3.24. All graphs show small variation in longitudinal strain, especially the ones with low positions of the ring which leads to little compression of the structure and therefore low strains overall (see Figure 3.17). Such a phenomenon was expected on the basis of sensitivity analysis which suggested low influence of diagonal's radius and attachment point on longitudinal strain.

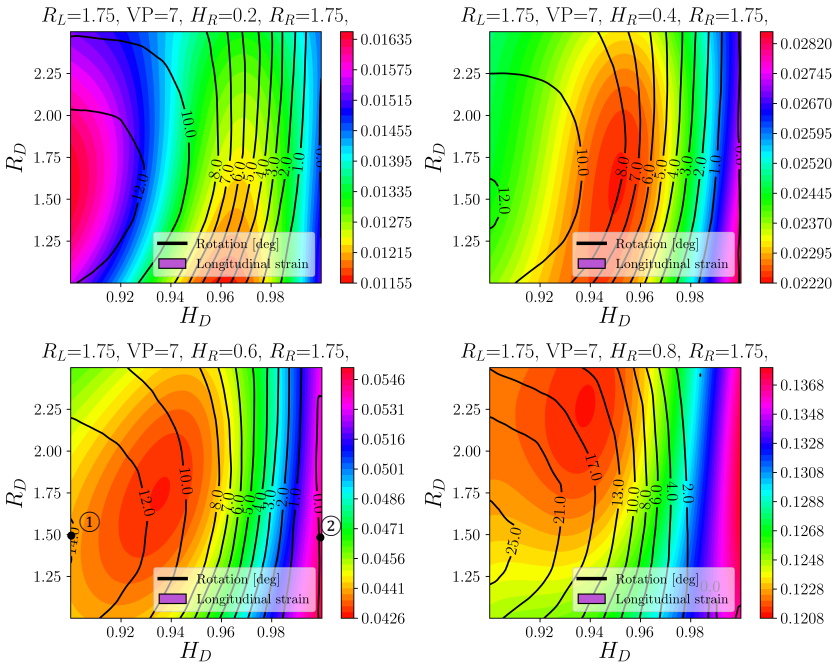

Figure 3.24: Mean longitudinal strain and rotation values presented as functions of diagonal radius and height as well as ring's height. Included numbers refer to designs shown in Figures 3.25 and 3.26.

Relationship between rotation and the parameters presented in Figure 3.24 mostly depends on the heights at which the diagonals and the ring are mounted. Radius of the diagonals seems to have a little influence on the range of rotation for low attached diagonals and almost no influence above $H_D > 0.95$. Height of the ring affects the extent to which longerons are pushed inwards so the higher it is mounted the more rotation can be expected as shown before in Figures 3.20 and 3.21. Finally, the height of diagonal's mounting point is the crucial parameter which determines the extent to which longerons are bent tangentially. Attachment of diagonals further away from the constrained points (lower) makes the moment, with which diagonals act on longerons, bigger. Additionally, the further down the less stiff the longeron is, hence more rotation is caused (see Figures 3.25 and 3.26).

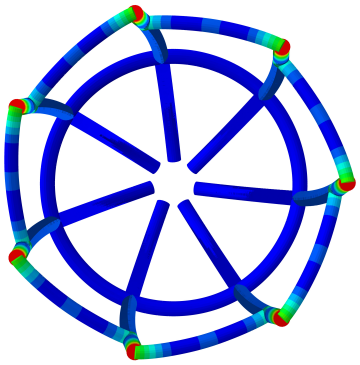

Figure 3.25: Top view of a structure with a low placed diagonal. Configuration corresponds to point 1 in Figure 3.24. (H_R = 0.6 H_D = 0.9 R_L = 1.75 R_D = 1.5 R_R = 1.75 $Polygon$ = 7)

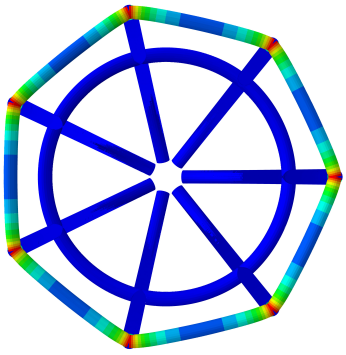

Figure 3.26: Top view of a structure with a highly placed diagonal. Configuration corresponds to point 2 in Figure 3.24. (H_R = 0.6 H_D = 0.999 R_L = 1.75 R_D = 1.5 R_R = 1.75 $Polygon$ = 7)

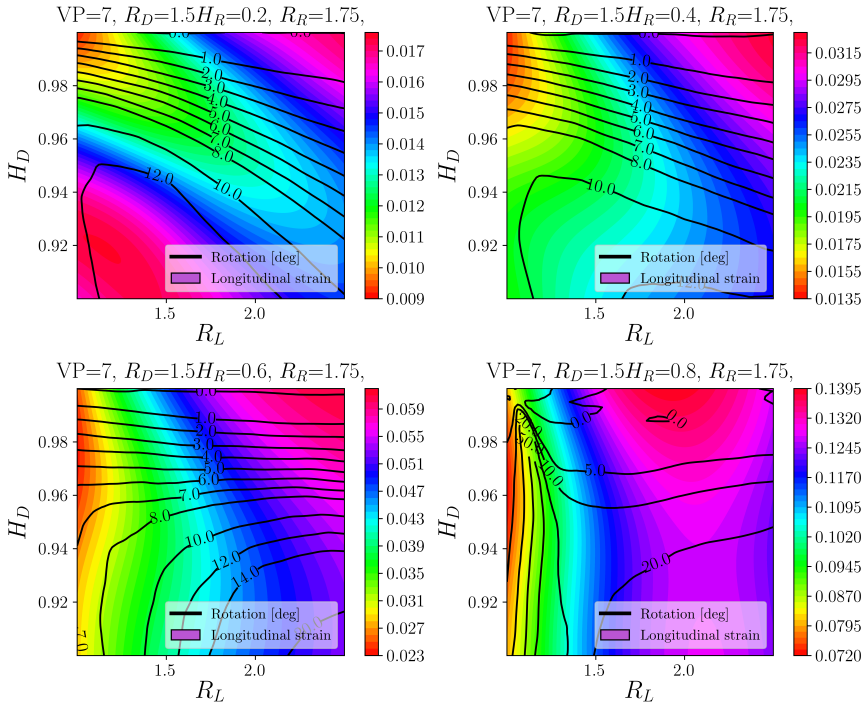

Figure 3.27: Mean longitudinal strain and rotation values presented as functions of diagonal height, longeron radius and ring height

The above analysis suggests that configurations of interest are the ones with highly positioned rings, which cause more longitudinal and radial strains, while rotation can be adjusted with diagonal related parameters. What can be observed on the basis of Figure 3.27 is that in structures with intermediate ring height of $H_R = 0.6$ increasing the longeron's thickness leads to increased rotation and longitudinal strains. This can be explained by relatively long length over which they can bend before being constrained by the ring and also their consistent bending due to own stiffness. Ring at the height of $H_R = 0.8$ leaves little space for lateral bending of longerons and either they need to be thin and possible to be pushed inwards causing more rotation or thick in order to retain the lateral motion.

So far it can be observed that rotation of the structure in most configurations is developed in two stages - tangential deformation of longerons in the first place and extending the effect further with radial compression by the ring. If relatively low rotations (up to 15°) are to be obtained, diagonal placement plays the key role in definition of the rotation extent. In the case when more rotation is desired, for instance to test its influence on inflammation of heart's tissue under application of the structure, the effect needs to be developed further by increasing the height of the ring as shown in the last quadrant of Figure 3.27.

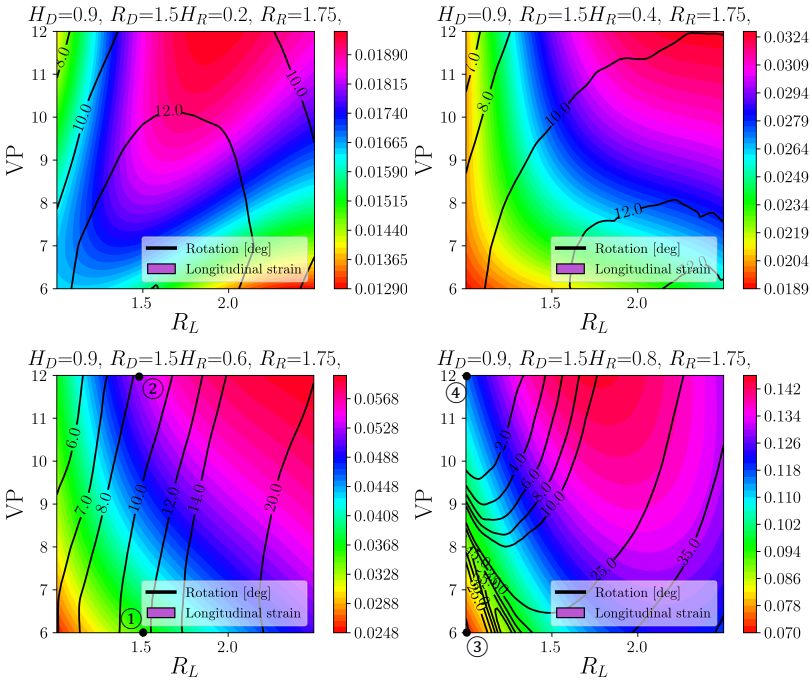

Figure 3.28: Mean longitudinal strain and rotation values presented as functions of number and radius of the longerons as well as the height of the ring. Included numbers refer to designs shown in Figures 3.29 - 3.32.

The last parameter, which in combination with the height of the ring, strongly affects both rotation and longitudinal strain is the number of longerons. Regardless of the position of the ring, increasing the number of longerons leads to an increase in longitudinal strain. It needs to be noted though that strains above around 8% seemed to be impossible to achieve in any configuration within the given bounds due to the longerons clashing. The more longerons included the easier it is for them to clash (see Figure 3.32) but this could not be quantified with the data-driven analysis due to prohibitive computational expense of contact detection. For this reason a significant part of the fourth quadrant of Figure 3.28 is not realistically useful. The increasing trend in strain based on the number of longerons can be explained by less slack in contraction of the ring; the ring compresses the structure at more points leading to more uniform radial squeezing and retaining the circular shape as shown in Figure 3.30.

Rotation described in the design space sections presented in Figure 3.28 is relatively complex. For low ring positions one may expect low variance of this quantity of interest while as the ring is put higher the possible extent of rotation increases, especially if such a change is accompanied by an increase in radius of the longerons as described before. The additional property which can be inferred from Figure 3.28 is that as the number of longerons increases the expected rotation drops. This is because diagonals are shorter in such configurations and are able to pull on the longerons to a lesser extent.

As the activation mode has not been decided at the moment of writing this document, a higher number of longerons is desirable. It makes the diagonals shorter and helps the upper structure retain the circular shape as shown in Figure 3.30 which makes the use of a circular magnetic field easier. Otherwise, with a small number of longerons, the diagonals are long and deform as shown in Figure 3.29. This makes the analysis fully realistic only with the coil-based mode of activation as such coils can deliver the same field magnitude regardless of the diagonals' shape.

General conclusions could be drawn at this stage and the choice of parameters as well as their bounds for optimization were made. The number of longerons was expected to be 6 or 7 in order to avoid their clashing while providing enough sturdiness to the structure and allowing sufficient rotation. Height of the ring was deemed unlikely to be the maximum as it leads to excessive compression but definitely to be above $H_R = 0.6$ in order to provide enough strain. Small radius of the ring proved to allow for more rotation and did not affect the longitudinal strain to a significant extent so a value close to the minimum was expected. Radius of the diagonal was chosen as fixed at 1.5 mm in order not to make the connection points too stiff. Radius of the longerons was predicted to be close to the maximal bound as it makes the achievement of high longitudinal strains easier and is also beneficial to the sturdiness of the structure. As the optimization was designed with an additional parameter in the form of varying local strain, the above conclusions were likely to change to some extent.

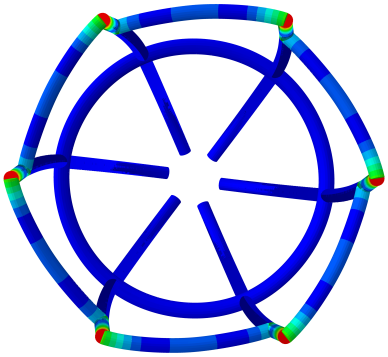

Figure 3.29: Top view of a structure with 6 longerons. Configuration corresponds to point 1 in Figure 3.28.

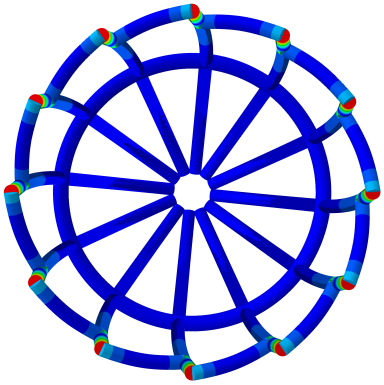

Figure 3.30: Top view of a structure with 12 longerons. Configuration corresponds to point 2 in Figure 3.28.

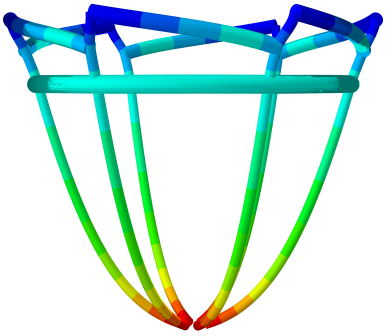

Figure 3.31: Side view of a structure with 6 longerons. Configuration corresponds to point 3 in Figure 3.28.

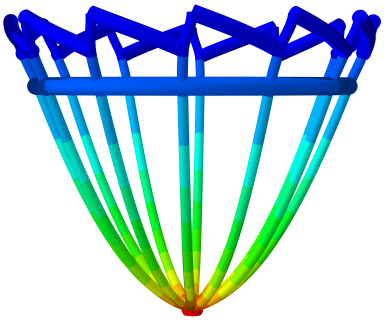

Figure 3.32: Side view of a structure with 12 longerons. Configuration corresponds to point 4 in Figure 3.28.

Table 3.7: Configuration parameters for Figures 3.27 - 3.30

Parameter	Figure 3.27	Figure 3.28	Figure 3.29	Figure 3.30
R_L [mm]	1.5	1.5	1.0	1.0
$Polygon$	6	12	6	12
H_D	0.9	0.9	0.9	0.9
R_D [mm]	1.5	1.5	1.5	1.5
H_R	0.6	0.6	0.8	0.8
R_R [mm]	1.75	1.75	1.75	1.75

3.3.3. DATA-DRIVEN MODEL OPTIMIZATION

If the designed ventricular assist device is developed further and passes tests positively it could be configured and printed in various facilities all over the world. Making this process as smooth and fast as possible requires software capable of picking the best design for a specific patient and their needs. For this reason, with the use of a supercomputer one should obtain a general model for the VAD whose geometry is not only parametrized with respect to the 6 variables presented in this thesis but also with respect to general dimensions: height, apex radius and base radius. Such, a full model could be used to pick a suitable design for any heart size within the bounds for which it is created.

If the developed machine learning model is based on a sufficient number of datapoints one can just impose constraints on the outputs and pick the most suitable configuration out of the simulated ones. However, if the model is scarce, an optimization process can be run on the model itself without a need for additional simulations. Such a solution reduces the need for access to simulation software at the production facilities.

A sample comparison of the two described approaches is presented herein:

- **Approach 1:** Finding an optimal solution from just the simulated datapoints
- **Approach 2:** Finding an optimal solution by exploitation of the model with an optimization process

Constraints imposed were related to scope of motion of a healthy heart and the objective was the longitudinal strain whose achievement at a sufficient level appeared to be the hardest throughout this work:

- **Objective:** Maximization of longitudinal strain
- **Constraint 1:** Rotation $\geq 13°$
- **Constraint 2:** Rotation $\leq 19°$
- **Constraint 3:** Radial deformation $\leq 10mm$

The purpose of limiting the radial deformation was to avoid clashing of longerons as the apex radius was set at $12mm$ in this analysis. Constraining this displacement to only $10mm$ leaves some space for each of the longerons in the deformed position. Introduction of contact detection into simulations which act as training points for the model would be much more accurate and desired. However, at this stage the imposed limitation seemed to be the best solution to the problem. It makes the device in its optimal configuration physically capable of performing its function without the contact of elements under compression. Rotation requirement was set between 13 and $19mm$ for it being the natural scope of motion in a healthy heart. Such constraints can be tailored to personal needs and imposed on any of the three quantities of interest: longitudinal strain, radial deformation or rotation or on any of the 6 variable parameters if needed.

The second approach was realized with augmented Lagrangian algorithm coupled with the nonlinear optimizer NLopt, both of which are available in pygmo Python library [19]. This choice was motivated by the algorithm's capability of global optimization with constraints and its good performance. The method was unconventional, as the algorithm was fed with an initial population consisting of all available 49994 datapoints and purely exploited to check the potential scope of improvement over the best datapoint. All three quantities of interest: longitudinal strain, radial deformation and rotation were predicted at each iteration with the respective machine learning models. The resultant, best objective function evaluation was a longitudinal strain of 7.7% obtained with the configuration whose parameters are shown in Table 3.8.

Table 3.8: Best input parameters

Parameter	H_R	H_D	R_L	R_D	R_R	$Polygon$
Best input	0.64	0.91	1.39 mm	2.17 mm	1.12 mm	11

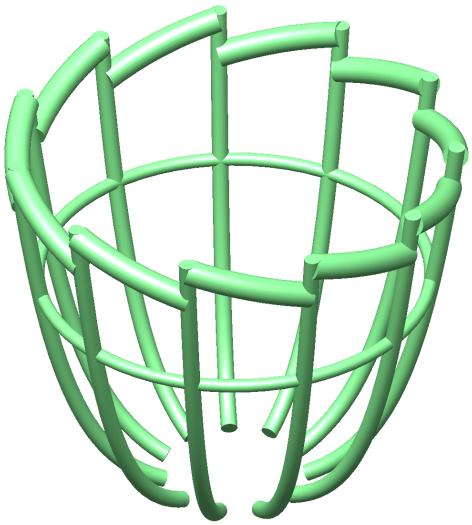

Figure 3.33: Configuration obtained from the exploited data-driven model with parameters presented in Table 3.8 and longitudinal strain capability at the level of 7.7%

Optimal input components found from both approaches differ by less than 0.3% of each value and the difference in objective is lower than 0.1% of longitudinal strain. Such results show that the model developed on the basis of 6 variable parameters, for the specific heart dimensions, and with the use of 50000 datapoints performs well on its own. However, development of such a model for 9 parameters, including the general heart dimensions within naturally found bounds, would not be possible without the use of a supercomputer. Simulations run within such facilities may become expensive, depending

on the time of analysis. Hence, another solution feasible with the use of just a powerful PC is proposed in Chapter 4.

What can be seen in Figure 3.33 is that the optimal, model-based configuration would encompass the heart well due to presence of 11 longerons. The ring is placed at a moderate height, which aids the stiffness of the structure as the longerons are laterally supported. Parameter suboptimal from the practical point of view is the radius of the diagonals, which are significantly thicker than longerons to which they are attached. This could cause issues while manufacturing so an additional constraint of diagonal radius being equal or smaller to longeron radius is proposed as a solution. According to sensitivity analysis (see Figure 3.14) diagonal radius has little to no influence on longitudinal strain and radial deformation so this parameter is expected not to affect the outcome significantly.

4

BAYESIAN OPTIMISATION

IN this chapter a solution alternative to data-driven approach is proposed. If simulation software like ABAQUS is available and a limited number of designs is to be obtained one can search for the most advantageous configuration with Bayesian optimization. As described in Subsection 2.4.3, this algorithm evaluates the black-box function (with FEM simulations of specific configurations in this case) and suggests every next sampling point so that the optimum is reached in a small number of trials. This method could be used to design a suitable VAD for patients until a general data-driven model is obtained and shared with production facilities. Its computational cost is significantly lower provided that the number of desired configurations is small. For production at multiple facilities and for numerous patients it would still be desirable to obtain a full data-driven model which can be sampled with constraints or exploited without further simulations.

This chapter describes the methodology applied in the optimization process - Section 4.1, the results obtained from two analyses of different complexities - Section 4.2 and is concluded with a short analysis of the potential next generation VAD - Section 4.3.

4.1. METHODOLOGY

The developed structure in its basic version was optimized in two stages, once with only 4 most significant parameters, to determine scope for simplification and time saving, and later with all 7 of them. Data-driven analysis allowed for determination of reasonable parameter bounds and choosing the ones which should be included in the first stage of optimization. Additionally to the variables which describe the geometry of the VAD, local strain was added in order to check if the maximal local deformation of the material as well as the maximal magnitude of the magnetic field are required for the optimal operation of the device.

Table 4.1: Variable parameters used in optimization at both stages along with their lower and upper bounds

	First stage		Second stage	
Parameter	Low. bound	Up. bound	Low. Bound	Up. bound
Ring height	0.1	0.8	0.1	0.8
Diagonal height	0.92	0.92	0.9	0.999
Longeron radius [mm]	1.0	2.5	1.0	2.5
Diagonal radius [mm]	1.5	1.5	1.0	2.5
Ring radius [mm]	1.0	2.5	1.0	2.5
Polygon	7	7	3	12
Local strain [%]	1	10	1	10

Choice of parameters for the first stage of optimization was performed in a twofold manner. Firstly the longitudinal and radial deformation models were considered as the ones which influence the outcome to the highest extent because of the way the objective function was defined. Secondly the three most important factors from sensitivity analysis were chosen along the local strain and all were given bounds as defined in table 4.1. The other parameters required for full specification of the geometry were fixed constant at values which promoted sturdiness of design and were deemed beneficial to the behaviour as indicated by the data-driven analysis (see Chapter 3). Number of longerons was fixed at 7 for such a design rarely resulted in clashing parts. Diagonal relative height was chosen to be 0.92 with consideration of its change after optimization as this parameter barely affects the longitudinal and radial deformation while mostly defining extent of rotation. Diagonal radius was fixed at 1.5 mm in order to add some material to the structure while avoiding making it too rigid.

In the optimization process position of the first longeron in all dimensions is sampled at 26 points along its length which allows for various ways of objective function definition. The most obvious one would be comparison of deformed geometry of the smart structure in the X-Z plane with the reference deformation of a perfect myocardium with the use of an R^2 fit coefficient. This was, however, ruled out due to the fact that top of the structure is fixed as can be seen in Figure 4.1 and maximization of the fit coefficient could result in overcompressing the bottom of the structure to make up for the immobility of its top part. Therefore, the choice of the objective function went for the distance between the tip of the longeron in deformed position and average position in which it should be according to the healthy heart reference. Such distance as shown in Figure 4.1 reflects on both longitudinal and radial deformations, the trade-off of which is supposed to give the correct longeron's tip placement. The distance is calculated as:

$$Obj = \sqrt{(\text{radial distance})^2 + (\text{vertical distance})^2} \tag{4.1}$$

The deformed reference geometry comes in two forms: the minimal and maximal ones attainable by a healthy heart as presented in Table 2.1 - with 15.9 - 22.1% contraction longitudinally and 20.9 - 27.8% circumferentially. The function which describes the undeformed outer shape of the sample myocardium [119] was obtained so the specific circumferential and longitudinal strains are applied as percentage contraction in the X and Z directions respectively. This is, however, only an approximation made for the sake of simplicity of the analysis. As described in Subsection 2.1.1, the motion of a healthy heart is complex and the best approach, impossible at this stage and inconvenient in general, would be to scan the specific organ for which the VAD is made in order to establish its range of motion and exact shape.

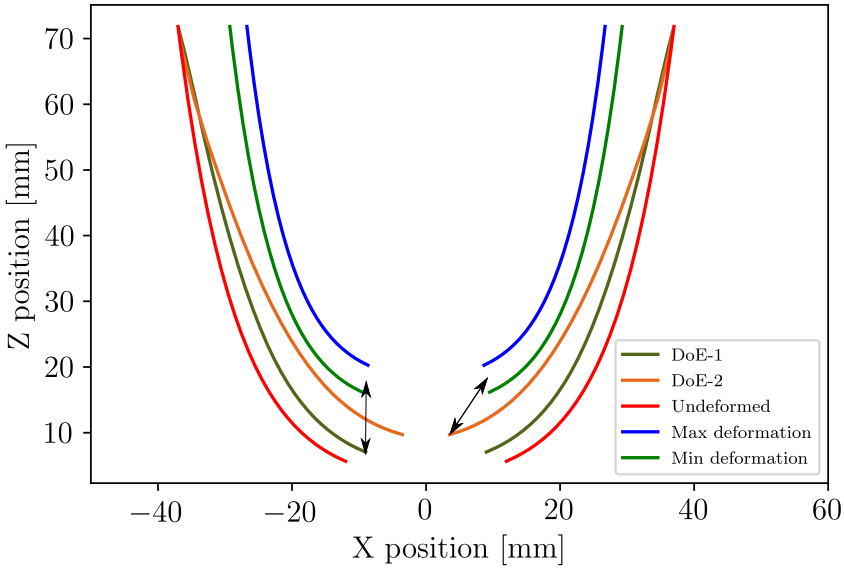

Figure 4.1: Visualisation of the metamaterial's deformation in X-Z plane compared against maximal and minimal deformations typical for healthy myocardia. The black arrows show the objective for both DoEs, which in this particular case have values of 13.04 mm and 11.58 mm for DoE-1 and DoE-2 respectively. Parameters of the DoEs are as follows: DoE-1 ($H_R = 0.31$ $H_D = 0.91$ $R_L = 1.24$ $R_D = 1.89$ $R_R = 1.43$ $Polygon = 8$), DoE-2 ($H_R = 0.63$ $H_D = 0.96$ $R_L = 2.12$ $R_D = 1.06$ $R_R = 2.09$ $Polygon = 10$).

Bayesian optimization was implemented with the GPyOpt module [4] due to its simplicity and ease of connection with the FEM simulation software. Based on the acquisition function review summarised earlier the Expected Improvement function was chosen for its trade-off in exploration and exploitation. The required optimization time and number of iterations were not known before solution of the problem. For this reason at first a few trials with 1000 iterations were done without contact detection in simulations in order to estimate the needed number of DoE analyses in short time. In all cases little to

no improvement (less than 0.1%) in objective function was seen after 250 iterations so the minimum number of iterations was set at 300 for the same number of parameters in order not to lose potential improvement but also to limit the time needed to evaluate DoEs with contact detection. This feature was employed to the extent possible with ABAQUS implicit - contact detection between centerlines of the beam elements. The optimization algorithm at each stage evaluated an initial population of 150 samples and then worked until convergence or for additional 300 iterations.

4.2. RESULTS

Bayesian optimization yielded interesting results in the form of design presented in Figure 4.2 with the objective function value at the level of 11.5 mm. Such a result can be obtained with parameters given in table 4.2 but similar compression of the myocardium could also be reached with other configurations. The value to which the objective function converges is limited by the fixed length of longerons which are unable to contract along their own axis. A week long second stage analysis with 7 parameters was run in order to check how much one could improve this result and the outcome suggested an optimal value at the level of 11.49 mm for the objective. Such a design consisted of 8 longerons with thickness of 2.5 mm and a ring positioned at the maximal relative height of 0.8 which already results in slight clashing of the longeron tips. Short analysis of convergence of both optimization processes and the results of the second stage analysis with all parameters are summarized in Appendix B.

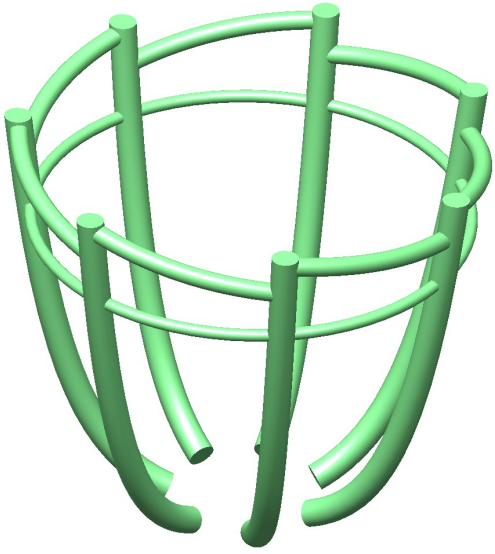

Figure 4.2: Visualisation of the design optimized with 4 parameters capable of 7.2% longitudinal strain and 63° of rotation.

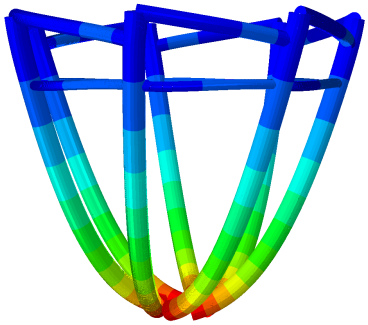

Figure 4.3: Side view of the deformed configuration optimized with 4 parameters

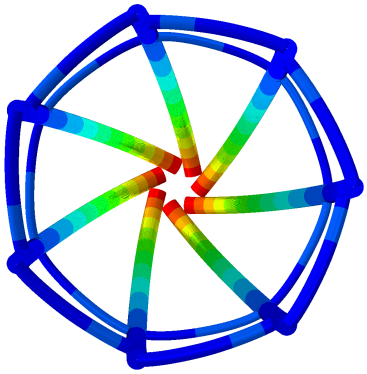

Figure 4.4: Top view of the deformed configuration optimized with 4 parameters

Table 4.2: Parameter values of the design optimized for ring height, ring radius, longeron radius and local strain

Parameter	R_L	$Polygon$	H_D	R_D	H_R	R_R	Strain
Optimal value	2.5 mm	7	0.92	1.5 mm	0.8	1.0 mm	7.24%

The optimal design suggested by a 4 parameter analysis is capable of 7.2% longitudinal strain at induced rotation of 63° and local strain of 7.1%. This shows that the magnetic field required to activate the metamaterial does not need to reach the maximal value which causes 10% of local strain. This specific design as shown in Figure 4.3 and 4.4 utilizes the highest possible placement of the ring which allows for the aforementioned lowered required local strain, which is the main difference between data-driven predictions and the actual result. Low positioned diagonals of sufficient thickness induce significant amount of rotation which according to Trumble et al. [150] should be tolerated by the myocardium.

At the moment of writing this document the first samples of the optimized metamaterial were 3D-printed. The tips of longerons at the base were extended and flattened in the model as can be seen in Figure 4.2 in order to facilitate the manufacturing process. It was also noted that such a configuration may not be ideal for practical reasons of the high ring placement and low rigidity of the structure.

Figure 4.5 shows the cross section of the optimized design which for the lower part of the structure provides enough strain to match the minimal deformation of a healthy heart. The issue that remains for all configurations is the immobility at the base which should be removed in the next iteration of the design. Additionally, it can be seen that the apex of the myocardium is compressed radially but not lifted high enough to match the desired position. Such problem seems to be solvable only with longerons capable of axial contraction, hence the coil-based mode of activation would be required for it. An opti-

mization stage with includes this mode and contractible longerons is presented below in Section 4.3.

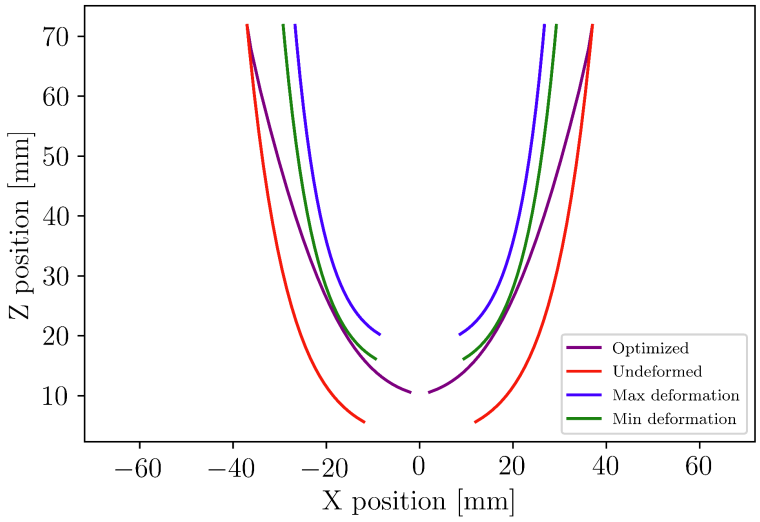

Figure 4.5: X-Z plane cross-section of the optimized design plotted against minimal and maximal deformations typical for a healthy myocardium

As mentioned above it seems to be impossible to break the distance limit of 11.5 mm in the case of the given objective function because of non-contractible longerons and their non-zero thickness that prohibits further contraction towards the centre of the structure. It may, however be possible to achieve similar values of the objective function with alternative configurations as suggested by the data-driven analysis. This can be utilized in order to make the structure more rigid and durable or for tailoring the design to special needs of the patient. For more information please see the last section of Appendix A.

4.3. NEXT GENERATION

The final stage of the Bayesian optimization related work was the brief analysis of a structure which could potentially alleviate the issues described above. With the assumption of feasibility of the coil-based mode of actuation the Bayesian optimization framework was utilized to find an optimal configuration of a device with contractible longerons.

The material used for the whole structure was still the PCL doped with 20%$rGO-Fe_3O_4$ nanoparticles described in Subsection 2.3.7. All elements of the metamaterial were activated with the same strain as chosen from the range of 1 – 10%, which is a vast simplification and should not be reproduced as most likely even better results could be obtained with local strain varied across elements. The framework settings remained unchanged with variable parameters being the same as in the case of basic 7 parameter optimization (see Table 4.1). The simulations were, however, run without contact detection due to a time constraint and because the clashing of longerons was not expected with their ability to contract.

As expected, the results brought an improved design which more than halved the value of the objective function, reaching just 4.6 mm. Shortening of longerons resembles the natural compression of the heart, hence their endpoints could be brought closer to the desired position as shown in Figure 4.9. Such a design is capable of 15.6% of longitudinal strain and 26.7° of rotation. Parameters of the optimal configuration are presented in Table 4.3.

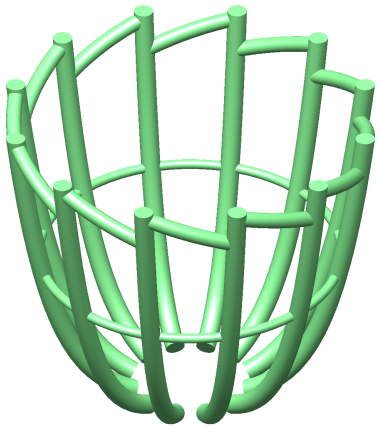

Figure 4.6: Visualisation of the optimized design with contractible longerons capable of 15.6% longitudinal strain and 26.7° of rotation

Table 4.3: Parameter values of the optimized design with contractible longerons

Parameter	R_L	$Polygon$	H_D	R_D	H_R	R_R	Strain
Optimal value	2.0 mm	12	0.9	1.6 mm	0.53	1.0 mm	10%

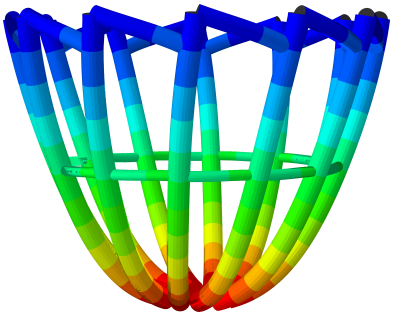

Figure 4.7: Side view of the optimized configuration with contractible longerons (in deformed state)

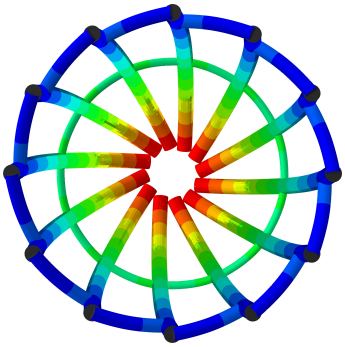

Figure 4.8: Top view of the optimized configuration with contractible longerons (in deformed state)

Deformation of the structure visible in Figures 4.7 and 4.8 does not result in significant clashing of longerons, hence with a little modification of their ends it could potentially be used to achieve strains close to the ones of a healthy heart in the vicinity of the apex. The design presented in Figure 4.6 achieves higher sturdiness than the configurations from the previous section due to retaining the relatively high thickness of longerons and a lower position of the ring. The only required improvement is liquidation of the structure's immobility close to the base as visible in Figure 4.9.

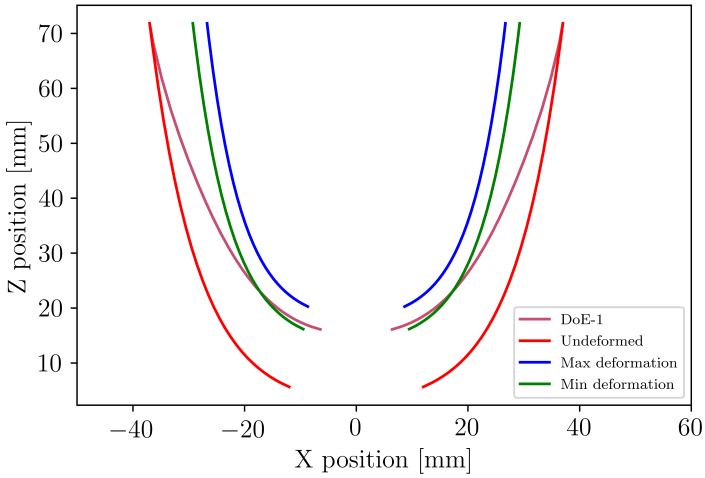

Figure 4.9: X-Z plane cross-section of the optimized design with contractible longerons plotted against minimal and maximal deformations typical for a healthy myocardium

5

CONCLUSIONS AND RECOMMENDATIONS

THE created framework allowed for development of the first iteration of a metamaterial based VAD. This chapter summarises the achievements along with imperfections of the design and analysis as well as provides suggestions on potential improvements if the project were to be continued.

5.1. CONCLUSIONS

The current design shows potential to match the radial deformation of a healthy myocardium close to its apex but clearly lacks radial strain in the proximity of the base and longitudinal strain at the apex in the basic configuration. It is still perceived as worth prototyping, mainly in order to test feasibility of the desired actuation modes and accuracy of the prepared machine learning models.

The next generation design presented in Section 4.3 is even more promising as it alleviates the longitudinal strain deficiency. Its operation is, however, only possible with the coil-based mode of activation. On the other hand, this mode seems to be more realistic and until the magnetic material's behaviour becomes better understood, it can be seen as the default mechanism.

The developed concept of a metamaterial based VAD shows capability of aiding the heart to a significant extent. Its actuation, according to the current predictions, can be achieved without transcutaneous wires and the device itself would not require any contact with blood as opposed to pump based appliances. The range of motion can be adjusted either with the variable parameters or with the applied magnetic field which influences local strains of the active elements. The next generation concept showed promising longitudinal strain and rotation values, comparable to the ones obtained by Roche et al. with their devices [118, 119]. Depending on the durability of the device,

which can only be assessed in the testing phase, the designed VAD could potentially be used in both bridge and destination therapies due to its non-intrusive nature. Finally, the developed framework and software show capability of tailoring the configuration to the patient's needs in a reasonable time-frame. It would still be beneficial to develop a general data-driven model including a range of heart sizes along with the currently variable parameters in order to make the configuration choice simpler.

The obtained machine learning models were seen as satisfying for a conceptual design due to their low mean errors and high accuracy, especially in the case of radial deformation and longitudinal strain models. The rotation model due to its complexity did not perform perfectly as shown in Appendix A but was sufficient to suggest trends that were later confirmed during Bayesian optimization. It needs to be noted that the predictions are based only on substance data provided by Dr. Miguel Dias Castilho and do not include imperfection modelling inherent to material or structure manufacturing. Material stiffness and complex interactions, resulting from geometry of the joints, are also not taken into account. For these reasons the uncertainty quantification was not performed and the confidence intervals for deformation magnitudes are not available.

Behaviour of the structure with the current geometry is mostly susceptible to changes in ring's height and radius as well as number and radius of the longerons. These parameters along with choice of local strain determine most of the radial and longitudinal strain. Rotation of the structure can be tuned with selection of the diagonal height attachment point and their radius barely affects the outcome so it can be chosen to fit other requirements like rigidity of the geometry.

The main disadvantage of the model in this field is the application of the same local strain to the ring and diagonals which was done in order to minimize the number of parameters and facilitate the analysis in the given time frame. No data was available to the author regarding behaviour of the magnetically activated material in fields non-axially aligned with the components. Hence, no additional assumptions could be made about the extent to which the diagonal elements contract in the same field as the ring or how the contraction of all elements varies under deformation and misalignment with the magnetic field. An activation solution which guarantees causation of the strains predefined for the simulations is the use of thin, flexible coils around the ring and diagonals, capable of creating the exact required fields in the structure. This would, however, be suboptimal with regards to the number of parts which need to be implanted into human body in order to power the VAD. The final decision about the mode of actuation still remains to be made.

5.2. RECOMMENDATIONS

Author of this thesis would like to acknowledge the fact that the analysis of potential application for the newly created magnetic material was performed when it was still at the development stage. For this reason the first recommendations are related to data that should be obtained in order to utilize the framework in a more informed way:

- **Material behaviour under non-axial magnetic fields** which would allow for differentiation between local strains in the diagonals and the ring
- **Quantification of the relationship between achievable local strain and the applied magnetic field** which could be implemented directly in the prepared programs to provide users with magnitudes of fields required for activation of each configuration
- **Measurement of maximal strain dependence on magnetic nanoparticle content** which could potentially facilitate use of lower magnitude magnetic fields in activation
- **Checking deterioration of material's properties in time** in order to estimate the safe number of cycles for the device

When such information is obtained and the framework is updated the next crucial step would be removal of the immobility at the base of the structure. This could potentially be achieved by utilization of another contractible ring at the metamaterial's base with a lower local strain than the main ring. Such a solution alone does not solve all the problems though as contraction of the geometry at the base leaves less space for the longeron tips and leads to lower possible longitudinal strains. After choosing the final mode of actuation - magnetic vest, coil-based system or any other solution which proves to be successful in activating the device, the concept of contractible longerons briefly investigated in Section 4.3 should be developed further. Another suggestion may be consideration of rotation as a mechanism for longitudinal strain induction. This, however falls beyond the scope of this document and is just a suggestion of potential improvement.

Finally, the computational approach can be further improved by:

- Addition of imperfection model and uncertainty quantification as performed by Glowacki[45]
- Increasing the number of datapoints used in data-driven analysis
- Optimization of hyperparameters in both data-driven analysis and Bayesian optimization
- Implementation of a better contact detection algorithm which detects clashing of elements' surfaces instead of only their axes
- Investigation of other objective functions for the optimization for instance volumetric contraction of the whole structure, which would provide more physical meaning of the objective value

- Development of a data-driven model which would not only include the 6 variable parameters defining the geometrical configuration but also the height of the structure as well as the apex and base radii

The additional suggestions listed above were not implemented in the current framework due to no need for additional accuracy at the conceptual stage of design but could provide more insight in future phases of the project.

REFERENCES

[1] CES EduPack Software, 2019.

[2] A. Alexander, J. Hensman, R. Turner, and Z. Ghahramani. On sparse variational methods and the Kullback-Leibler divergence between stochastic processes. Jan. 2016.

[3] M. F. Ashby. Engineering Materials and Their Properties. In *Materials Selection in Mechanical Design*, pages 31–56. Elsevier, 2011.

[4] T. G. authors. Gpyopt: A bayesian optimization framework in python. http://github.com/SheffieldML/GPyOpt, 2016.

[5] J. Azimi, X. Fern, A. Fern, E. Burrows, F. Chaplen, Y. Fan, H. Liu, J. Jaio, and R. Schaller. Myopic policies for budgeted optimization with constrained experiments. volume 1, Jan. 2010.

[6] S. Babaee, J. Shim, J. C. Weaver, E. R. Chen, N. Patel, and K. Bertoldi. 3d Soft Metamaterials with Negative Poisson's Ratio. *Advanced Materials*, 25(36):5044–5049, Sept. 2013.

[7] Y. Bar-cohen. Electroactive polymers as artificial muscles - Reality and challenges. In *19th AIAA Applied Aerodynamics Conference*, Anaheim,CA,U.S.A., June 2001. American Institute of Aeronautics and Astronautics.

[8] Y. Bar-Cohen. Electroactive polymers as actuators. In *Advanced Piezoelectric Materials*, pages 287–317. Elsevier, 2010.

[9] M. Bauer, M. van der Wilk, and C. E. Rasmussen. Understanding probabilistic sparse gaussian process approximations. In D. D. Lee, M. Sugiyama, U. V. Luxburg, I. Guyon, and R. Garnett, editors, *Advances in Neural Information Processing Systems 29*, pages 1533–1541. Curran Associates, Inc., 2016.

[10] S. Bauer and S. Bauer-Gogonea. Piezoelectric and Electrostrictive Polymers as EAPs: Devices and Applications. In F. Carpi, editor, *Electromechanically Active Polymers*, pages 533–547. Springer International Publishing, Cham, 2016.

[11] J. Bergstra, R. Bardenet, B. Kégl, and Y. Bengio. Algorithms for hyper-parameter optimization. Dec. 2011.

[12] K. Bertoldi, V. Vitelli, J. Christensen, and M. van Hecke. Flexible mechanical metamaterials. *Nature Reviews Materials*, 2(11), Oct. 2017.

[13] M. A. Bessa, R. Bostanabad, Z. Liu, A. Hu, D. W. Apley, C. Brinson, W. Chen, and W. K. Liu. A framework for data-driven analysis of materials under uncertainty: Countering the curse of dimensionality. *Computer Methods in Applied Mechanics and Engineering*, 320:633 – 667, 2017.

[14] M. A. Bessa, P. Glowacki, and M. Houlder. Bayesian Machine Learning in Metamaterial Design: Fragile Becomes Supercompressible. *Advanced Materials*, 31(48), Nov. 2019.

[15] M. A. Bessa and S. Pellegrino. Design of ultra-thin shell structures in the stochastic post-buckling range using Bayesian machine learning and optimization. *International Journal of Solids and Structures*, 139-140:174 – 188, 2018.

[16] B. Bhandari, G.-Y. Lee, and S.-H. Ahn. A review on IPMC material as actuators and sensors: Fabrications, characteristics and applications. *International Journal of Precision Engineering and Manufacturing*, 13(1):141–163, Jan. 2012.

[17] J. Biggs, K. Danielmeier, J. Hitzbleck, J. Krause, T. Kridl, S. Nowak, E. Orselli, X. Quan, D. Schapeler, W. Sutherland, and J. Wagner. Electroactive Polymers: Developments of and Perspectives for Dielectric Elastomers. *Angewandte Chemie International Edition*, 52(36):9409–9421, Sept. 2013.

[18] E. J. Birks, P. D. Tansley, J. Hardy, R. S. George, C. T. Bowles, M. Burke, N. R. Banner, A. Khaghani, and M. H. Yacoub. Left ventricular assist device and drug therapy for the reversal of heart failure. *New England Journal of Medicine*, 355(18):1873–1884, Nov. 2006.

[19] F. Biscani and D. Izzo. A parallel global multiobjective framework for optimization: pagmo. *Journal of Open Source Software*, 5(53):2338, 2020.

[20] C. M. Bishop. *Pattern recognition and machine learning*. Information science and statistics. Springer, New York, 2006.

[21] P. Bovendeerd, M. Arts, T. Delhaas, J. Huyghe, D. Campen, van, and R. Reneman. Regional wall mechanics in the ischemic left ventricle: numerical modeling and dog experiments. *American Journal of Physiology : Heart and Circulatory Physiology*, 270(1):H398–H410, 1996.

[22] A. F. Bower. *Applied mechanics of solids*. CRC Press, Boca Raton, 2010.

[23] P. Boyle, M. Frean, P. Boyle, and M. Frean. Multiple output gaussian process regression. Technical report, 2005.

[24] E. Brochu, V. M. Cora, and N. de Freitas. A Tutorial on Bayesian Optimization of Expensive Cost Functions, with Application to Active User Modeling and Hierarchical Reinforcement Learning. *arXiv:1012.2599*, Dec. 2010.

[25] G. Buckberg, A. Mahajan, S. Saleh, J. I. Hoffman, and C. Coghlan. Structure and function relationships of the helical ventricular myocardial band. *The Journal of Thoracic and Cardiovascular Surgery*, 136(3):578–589.e11, Sept. 2008.

[26] A. Cao. Super-Compressible Foamlike Carbon Nanotube Films. *Science*, 310(5752):1307–1310, Nov. 2005.

[27] F. Carpi. *Electromechanically active polymers: a concise reference*. Springer Berlin Heidelberg, New York, NY, 2016.

[28] H.-C. Cheng, H.-H. Huang, W.-H. Chen, and S.-T. Lu. Hygro-thermo-mechanical Behavior of Adhesive-Based Flexible Chip-on-Flex Packaging. *Journal of Electronic Materials*, 44(4):1220–1237, Apr. 2015.

[29] Ching-Ping Chou and B. Hannaford. Static and dynamic characteristics of McKibben pneumatic artificial muscles. In *Proceedings of the 1994 IEEE International Conference on Robotics and Automation*, pages 281–286, San Diego, CA, USA, 1994. IEEE Comput. Soc. Press.

[30] F. Chollet et al. Keras. https://keras.io, 2015.

[31] R. M. Cornell and U. Schwertmann. *The Iron Oxides Structure, Properties, Reactions, Occurrences and Uses*. 2006.

[32] C. Coulais, C. Kettenis, and M. van Hecke. A characteristic length scale causes anomalous size effects and boundary programmability in mechanical metamaterials. *Nature Physics*, 14(1):40–44, Jan. 2018.

[33] D. D. Cox and S. John. Sdo: A statistical method for global optimization. In *in Multidisciplinary Design Optimization: State-of-the-Art*, pages 315–329, 1997.

[34] F. Côté, P. Masson, N. Mrad, and V. Cotoni. Dynamic and static modelling of piezoelectric composite structures using a thermal analogy with MSC/NASTRAN. *Composite Structures*, 65(3-4):471–484, Sept. 2004.

[35] I. N. da Silva, D. Hernane Spatti, R. Andrade Flauzino, L. H. B. Liboni, and S. F. dos Reis Alves. *Artificial Neural Networks*. Springer International Publishing, Cham, 2017.

[36] T. Desautels, A. Krause, and J. W. Burdick. Parallelizing exploration-exploitation tradeoffs in gaussian process bandit optimization. *Journal of Machine Learning Research*, 15(119):4053–4103, 2014.

[37] A. Diermeier, D. Sindersberger, L. Krenkel, X. C. Rosell, and G. J. Monkman. Controllable Magnetoactive Polymer Conduit. *The Open Mechanical Engineering Journal*, 12(1):192–200, Nov. 2018.

[38] X.-J. Dong and G. Meng. Dynamic analysis of structures with piezoelectric actuators based on thermal analogy method. *The International Journal of Advanced Manufacturing Technology*, 27(9-10):841–844, Feb. 2006.

[39] K.-L. DU. *Neural Networks and Statistical Learning*. SPRINGER, 2019.

[40] B. Fajdek and K. Janiszowski. Automatic control system for ventricular assist device. In *2014 19th International Conference on Methods and Models in Automation and Robotics (MMAR)*, pages 874–879, Miedzyzdroje, Sept. 2014. IEEE.

[41] E. T. Filipov, T. Tachi, and G. H. Paulino. Origami tubes assembled into stiff, yet reconfigurable structures and metamaterials. *Proceedings of the National Academy of Sciences*, 112(40):12321–12326, Oct. 2015.

[42] T. Frenzel, M. Kadic, and M. Wegener. Three-dimensional mechanical metamaterials with a twist. *Science*, 358(6366):1072–1074, Nov. 2017.

[43] J. Gardner, M. Kusner, E. Xu, K. Weinberger, and J. Cunningham. Bayesian optimization with inequality constraints. volume 3, 06 2014.

[44] A. Y. Gervald, I. A. Gritskova, and N. I. Prokopov. Synthesis of magnetic polymeric microspheres. *Russian Chemical Reviews*, 79(3):219–229, May 2010.

[45] P. Glowacki. Data-driven design of a metamaterial unit cell using sparse gaussian processes, Mar. 2019.

[46] J. R. Gohean, M. J. George, T. D. Pate, M. Kurusz, R. G. Longoria, and R. W. Smalling. Verification of a Computational Cardiovascular System Model Comparing the Hemodynamics of a Continuous Flow to a Synchronous Valveless Pulsatile Flow Left Ventricular Assist Device:. *ASAIO Journal*, 59(2):107–116, 2013.

[47] D. J. Goldstein and R. B. Beauford. Left ventricular assist devices and bleeding: adding insult to injury. *The Annals of Thoracic Surgery*, 75(6):S42–S47, June 2003.

[48] I. Goodfellow, Y. Bengio, and A. Courville. *Deep learning*. Adaptive computation and machine learning. The MIT Press, Cambridge, Massachusetts, 2016.

[49] D. Graupe. *Principles of artificial neural networks*. Number volume 7 in Advanced series on circuits and systems. World Scientific, New Jersey, 3rd edition edition, 2013.

[50] J. N. Grima, R. Gatt, and P.-S. Farrugia. On the properties of auxetic metatetrachiral structures. *physica status solidi (b)*, 245(3):511–520, Mar. 2008.

[51] B. E. Grunau, M. O. Wiens, and J. R. Brubacher. Dantrolene in the treatment of MDMA-related hyperpyrexia: a systematic review. *CJEM*, 12(05):435–442, Sept. 2010.

[52] J. Han and D. Trumble. Cardiac Assist Devices: Early Concepts, Current Technologies, and Future Innovations. *Bioengineering*, 6(1):18, Feb. 2019.

[53] P. Harrington. *Machine learning in action*. Manning Publications Co, Shelter Island, N.Y, 2012.

[54] P. Hennig and C. J. Schuler. Entropy Search for Information-Efficient Global Optimization. Dec. 2011. arXiv: 1112.1217.

[55] J. Herman and W. Usher. Salib: An open-source python library for sensitivity analysis. *Journal of Open Source Software*, 2(9):97, 2017.

[56] J. M. Hernández-Lobato, M. W. Hoffman, and Z. Ghahramani. Predictive Entropy Search for Efficient Global Optimization of Black-box Functions. June 2014.

[57] N. Hu and R. Burgueño. Buckling-induced smart applications: recent advances and trends. *Smart Materials and Structures*, 24(6):063001, June 2015.

[58] W. Huang, C. Song, Y. Fu, C. Wang, Y. Zhao, H. Purnawali, H. Lu, C. Tang, Z. Ding, and J. Zhang. Shaping tissue with shape memory materials. *Advanced Drug Delivery Reviews*, 65(4):515–535, Apr. 2013.

[59] W. M. Huang, H. B. Lu, Y. Zhao, Z. Ding, C. C. Wang, J. L. Zhang, L. Sun, J. Fu, and X. Y. Gao. Instability/collapse of polymeric materials and their structures in stimulus-induced shape/surface morphology switching. *Materials & Design*, 59:176–192, July 2014.

[60] F. Jacquemin, S. Fréour, and R. Guillén. A self-consistent approach for transient hygroscopic stresses and moisture expansion coefficients of fiber-reinforced composites. In *11th European Conference on Composite Materials*, Rhodes, Greece, 2004.

[61] B. Jaffe, W. R. Cook, and H. L. Jaffe. *Piezoelectric ceramics*. Number v. 3 in Nonmetallic solids. Academic Press, London, New York, 1971.

[62] A. Jain, P. Duin, and Jianchang Mao. Statistical pattern recognition: a review. *IEEE Transactions on Pattern Analysis and Machine Intelligence*, 22(1):4–37, Jan. 2000.

[63] Z. Jiao, B. Luo, S. Xiang, H. Ma, Y. Yu, and W. Yang. 3D printing of HA / PCL composite tissue engineering scaffolds. *Advanced Industrial and Engineering Polymer Research*, 2(4):196–202, Oct. 2019.

[64] S. John, J. Sirohi, G. Wang, and N. M. Wereley. Comparison of Piezoelectric, Magnetostrictive, and Electrostrictive Hybrid Hydraulic Actuators. *Journal of Intelligent Material Systems and Structures*, 18(10):1035–1048, Oct. 2007.

[65] D. R. Jones, M. Schonlau, and W. J. Welch. Efficient Global Optimization of ExpensiveBlack-Box Functions. *Journal of Global Optimization*, 13(4):455–492, 1998.

[66] M. Kadic, T. Bückmann, N. Stenger, M. Thiel, and M. Wegener. On the practicability of pentamode mechanical metamaterials. *Applied Physics Letters*, 100(19):191901, May 2012.

[67] K. Kandasamy, K. R. Vysyaraju, W. Neiswanger, B. Paria, C. R. Collins, J. Schneider, B. Poczos, and E. P. Xing. Tuning hyperparameters without grad students: Scalable and robust bayesian optimisation with dragonfly. *Journal of Machine Learning Research*, 21(81):1–27, 2020.

[68] K. C. Kao. Electric Polarization and Relaxation. In *Dielectric Phenomena in Solids*, pages 41–114. Elsevier, 2004.

[69] M. Kimura, A. Ando, D. Maurya, and S. Priya. Lead Zirconate Titanate-Based Piezoceramics. In *Advanced Piezoelectric Materials*, pages 95–126. Elsevier, 2017.

[70] N. Knudde, J. van der Herten, T. Dhaene, and I. Couckuyt. GPflowOpt: A Bayesian Optimization Library using TensorFlow. 2017.

[71] R. Kornbluh, R. Pelrine, J. Eckerle, and J. Joseph. Electrostrictive polymer artificial muscle actuators. In *Proceedings. 1998 IEEE International Conference on Robotics and Automation*, pages 2147–2154, Leuven, Belgium, 1998. IEEE.

[72] I. Krakovský, T. Romijn, and A. Posthuma de Boer. A few remarks on the electrostriction of elastomers. *Journal of Applied Physics*, 85(1):628–629, Jan. 1999.

[73] I. K. Kuder, A. F. Arrieta, W. E. Raither, and P. Ermanni. Variable stiffness material and structural concepts for morphing applications. *Progress in Aerospace Sciences*, 63:33–55, Nov. 2013.

[74] K. A. Kydralieva, G. I. Dzhardimalieva, A. A. Yurishcheva, and S. J. Jorobekova. Nanoparticles of Magnetite in Polymer Matrices: Synthesis and Properties. *Journal of Inorganic and Organometallic Polymers and Materials*, 26(6):1212–1230, Nov. 2016.

[75] M. Labet and W. Thielemans. Synthesis of polycaprolactone: a review. *Chemical Society Reviews*, 38(12):3484, 2009.

[76] J. Leng, X. Lan, Y. Liu, and S. Du. Shape-memory polymers and their composites: Stimulus methods and applications. *Progress in Materials Science*, 56(7):1077–1135, Sept. 2011.

[77] J. Leng, H. Lu, Y. Liu, W. M. Huang, and S. Du. Shape-Memory Polymers—A Class of Novel Smart Materials. *MRS Bulletin*, 34(11):848–855, Nov. 2009.

[78] F. Levassort, M. Lethiecq, R. Desmare, and Tran-Huu-Hue. Effective electroelastic moduli of 3-3(0-3) piezocomposites. *IEEE Transactions on Ultrasonics, Ferroelectrics and Frequency Control*, 46(4):1028–1034, July 1999.

[79] F. Li, L. Jin, Z. Xu, and S. Zhang. Electrostrictive effect in ferroelectrics: An alternative approach to improve piezoelectricity. *Applied Physics Reviews*, 1(1):011103, Mar. 2014.

[80] Q. Li and Q. Wang. Ferroelectric Polymers and Their Energy-Related Applications. *Macromolecular Chemistry and Physics*, 217(11):1228–1244, June 2016.

[81] T.-C. Lim. Anisotropic and negative thermal expansion behavior in a cellular microstructure. *Journal of Materials Science*, 40(12):3275–3277, June 2005.

[82] T. C. Lim. A Negative Hygroscopic Expansion Material. *Materials Science Forum*, 928:277–282, Aug. 2018.

[83] T.-C. Lim. Composite metamaterial with sign-switchable coefficients of hygroscopic, thermal and pressure expansions. *Advanced Composites and Hybrid Materials*, 2(4):657–669, Dec. 2019.

[84] C. Liu, H. Qin, and P. T. Mather. Review of progress in shape-memory polymers. *Journal of Materials Chemistry*, 17(16):1543, 2007.

[85] H. Liu, Y.-S. Ong, X. Shen, and J. Cai. When gaussian process meets big data: A review of scalable gps, 2018.

[86] Y. Liu, H. Du, L. Liu, and J. Leng. Shape memory polymers and their composites in aerospace applications: a review. *Smart Materials and Structures*, 23(2):023001, Feb. 2014.

[87] Y. Liu, L. Liu, Z. Zhang, and J. Leng. Dielectric elastomer film actuators: characterization, experiment and analysis. *Smart Materials and Structures*, 18(9):095024, Sept. 2009.

[88] G. Loor and G. Gonzalez-Stawinski. Pulsatile vs. continuous flow in ventricular assist device therapy. *Best Practice & Research Clinical Anaesthesiology*, 26(2):105–115, June 2012.

[89] A. J. Lovinger. Ferroelectric Polymers. *Science*, 220(4602):1115–1121, June 1983.

[90] M. Álvarez and N. Lawrence. Computationally efficient convolved multiple output gaussian processes. *Journal of Machine Learning Research*, 12:1459–1500, 05 2011.

[91] C. Löwe, X. Zhang, and G. Kovacs. Dielectric Elastomers in Actuator Technology. *Advanced Engineering Materials*, 7(5):361–367, May 2005.

[92] L. R. Meza, S. Das, and J. R. Greer. Strong, lightweight, and recoverable three-dimensional ceramic nanolattices. *Science*, 345(6202):1322–1326, Sept. 2014.

[93] S. M. Mirvakili and I. W. Hunter. Artificial Muscles: Mechanisms, Applications, and Challenges. *Advanced Materials*, 30(6), Feb. 2018.

[94] J. Mockus. *Bayesian Approach to Global Optimization: Theory and Applications*, volume 37 of *Mathematics and Its Applications*. Springer Netherlands, Dordrecht, 1989.

[95] J. Mohd Jani, M. Leary, A. Subic, and M. A. Gibson. A review of shape memory alloy research, applications and opportunities. *Materials & Design (1980-2015)*, 56:1078–1113, Apr. 2014.

[96] S. O. R. Moheimani and A. J. Fleming. *Piezoelectric transducers for vibration control and damping*. Advances in industrial control. Springer, London, 2006.

[97] G. Montavon, G. B. Orr, and K.-R. Müller, editors. *Neural Networks: Tricks of the Trade: Second Edition*. Lecture Notes in Computer Science. Springer Berlin Heidelberg, Berlin, Heidelberg, 2012.

[98] Munasir and R. P. Kusumawati. Synthesis and Characterization of Fe3O4@rGO Composite with Wet-Mixing (ex-situ) Process. *Journal of Physics: Conference Series*, Feb. 2019.

[99] D. M. Murphy, T. W. Murphey, and P. A. Gierow. Scalable Solar-Sail Subsystem Design Concept. *Journal of Spacecraft and Rockets*, 40(4):539–547, July 2003.

[100] A. Nespoli, S. Besseghini, S. Pittaccio, E. Villa, and S. Viscuso. The high potential of shape memory alloys in developing miniature mechanical devices: A review on shape memory alloy mini-actuators. *Sensors and Actuators A: Physical*, 158(1):149–160, Mar. 2010.

[101] C. K. Ng, K. K. Saxena, R. Das, and E. I. Saavedra Flores. On the anisotropic and negative thermal expansion from dual-material re-entrant-type cellular metamaterials. *Journal of Materials Science*, 52(2):899–912, Jan. 2017.

[102] Z. G. Nicolaou and A. E. Motter. Mechanical metamaterials with negative compressibility transitions. *Nature Materials*, 11(7):608–613, July 2012.

[103] C. Nwankpa, W. Ijomah, A. Gachagan, and S. Marshall. Activation Functions: Comparison of trends in Practice and Research for Deep Learning. *arXiv:1811.03378*, Nov. 2018.

[104] H. Obeid, A. Clément, S. Fréour, F. Jacquemin, and P. Casari. On the identification of the coefficient of moisture expansion of polyamide-6: Accounting differential swelling strains and plasticization. *Mechanics of Materials*, 118:1–10, Mar. 2018.

[105] J. P. Olberding and S. M. Deban. Effects of temperature and force requirements on muscle work and power output. *The Journal of Experimental Biology*, 220(11):2017–2025, June 2017.

[106] T. Onishi, S. K. Saha, A. Delgado-Montero, D. R. Ludwig, T. Onishi, E. B. Schelbert, D. Schwartzman, and J. Gorcsan. Global Longitudinal Strain and Global Circumferential Strain by Speckle-Tracking Echocardiography and Feature-Tracking Cardiac Magnetic Resonance Imaging: Comparison with Left Ventricular Ejection Fraction. *Journal of the American Society of Echocardiography*, 28(5):587–596, May 2015.

[107] O. E. Ozbulut, S. Hurlebaus, and R. Desroches. Seismic Response Control Using Shape Memory Alloys: A Review. *Journal of Intelligent Material Systems and Structures*, 22(14):1531–1549, Sept. 2011.

[108] D. Packwood. *Bayesian Optimization for Materials Science*, volume 3 of *SpringerBriefs in the Mathematics of Materials*. Springer Singapore, Singapore, 2017.

[109] R. Pelrine, R. Kornbluh, J. Joseph, R. Heydt, Q. Pei, and S. Chiba. High-field deformation of elastomeric dielectrics for actuators. *Materials Science and Engineering: C*, 11(2):89–100, Nov. 2000.

[110] R. E. Pelrine, R. D. Kornbluh, and J. P. Joseph. Electrostriction of polymer dielectrics with compliant electrodes as a means of actuation. *Sensors and Actuators A: Physical*, 64(1):77–85, Jan. 1998.

[111] K. Petcharoen and A. Sirivat. Electrostrictive properties of thermoplastic polyurethane elastomer: Effects of urethane type and soft–hard segment composition. *Current Applied Physics*, 13(6):1119–1127, Aug. 2013.

[112] L. Puig, A. Barton, and N. Rando. A review on large deployable structures for astrophysics missions. *Acta Astronautica*, 67(1-2):12–26, July 2010.

[113] Y. Qiu, E. Zhang, R. Plamthottam, and Q. Pei. Dielectric Elastomer Artificial Muscle: Materials Innovations and Device Explorations. *Accounts of Chemical Research*, 52(2):316–325, Feb. 2019.

[114] K. S. Ramadan, D. Sameoto, and S. Evoy. A review of piezoelectric polymers as functional materials for electromechanical transducers. *Smart Materials and Structures*, 23(3), Mar. 2014.

[115] C. E. Rasmussen and C. K. I. Williams. *Gaussian processes for machine learning*. Adaptive computation and machine learning. MIT Press, Cambridge, Mass, 2006.

[116] L. Rasmussen, editor. *Electroactivity in Polymeric Materials*. Springer US, 2012.

[117] D. Restrepo, N. D. Mankame, and P. D. Zavattieri. Phase transforming cellular materials. *Extreme Mechanics Letters*, 4:52–60, Sept. 2015.

[118] E. T. Roche, M. A. Horvath, I. Wamala, A. Alazmani, S.-E. Song, W. Whyte, Z. Machaidze, C. J. Payne, J. C. Weaver, G. Fishbein, J. Kuebler, N. V. Vasilyev, D. J. Mooney, F. A. Pigula, and C. J. Walsh. Soft robotic sleeve supports heart function. *Science Translational Medicine*, 9(373), Jan. 2017.

[119] E. T. Roche, R. Wohlfarth, J. T. B. Overvelde, N. V. Vasilyev, F. A. Pigula, D. J. Mooney, K. Bertoldi, and C. J. Walsh. A Bioinspired Soft Actuated Material. *Advanced Materials*, 26(8):1200–1206, Feb. 2014.

[120] G. A. Roth. Global, Regional, and National Burden of Cardiovascular Diseases for 10 Causes, 1990 to 2015. *Journal of the American College of Cardiology*, 70(1):1–25, July 2017.

[121] A. Saltelli. Making best use of model evaluations to compute sensitivity indices. *Computer Physics Communications*, 145(2):280–297, May 2002.

[122] A. Saltelli, editor. *Sensitivity analysis in practice: a guide to assessing scientific models*. Wiley, Hoboken, NJ, 2004.

[123] A. Saltelli, editor. *Global sensitivity analysis: the primer*. John Wiley, Chichester, England ; Hoboken, NJ, 2008.

[124] A. Savine and L. B. G. Andersen. *Modern computational finance: AAD and parallel simulations with professional implementation in C++*. Wiley, Hoboken, New Jersey, 2019.

[125] T. A. Schaedler, A. J. Jacobsen, A. Torrents, A. E. Sorensen, J. Lian, J. R. Greer, L. Valdevit, and W. B. Carter. Ultralight Metallic Microlattices. *Science*, 334(6058):962–965, Nov. 2011.

[126] A. R. Schulman, T. P. Martens, P. J. Christos, M. J. Russo, G. M. Comas, F. H. Cheema, T. M. Naseem, R. Wang, K. A. Idrissi, S. H. Bailey, and Y. Naka. Comparisons of infection complications between continuous flow and pulsatile flow left ventricular assist devices. *The Journal of Thoracic and Cardiovascular Surgery*, 133(3):841–842, Mar. 2007.

[127] E. Schulz, M. Speekenbrink, and A. Krause. A tutorial on Gaussian process regression: Modelling, exploring, and exploiting functions. *Journal of Mathematical Psychology*, 85:1–16, Aug. 2018.

[128] M. Seeger. Gaussian Processes for Machine Learning. *International Journal of Neural Systems*, 14(02):69–106, Apr. 2004.

[129] M. SEEGER. GAUSSIAN PROCESSES FOR MACHINE LEARNING. *International Journal of Neural Systems*, 14(02):69–106, Apr. 2004.

[130] M. Shahinpoor. A review of patents on implantable heart-compression/assist devices and systems. *Recent Patents on Biomedical Engineeringe*, 3(1):54–71, Jan. 2010.

[131] S. Shalev-Shwartz and S. Ben-David. *Understanding Machine Learning: From Theory to Algorithms*. Cambridge University Press, Cambridge, 2014.

[132] S. Shanmuganathan and S. Samarasinghe. *Artificial neural network modelling*. Springer Berlin Heidelberg, New York, NY, 2016.

[133] S. Sharma. Activation functions in neural networks. *Towards Data Science*, 6, 2017.

[134] Y. M. Shkel and D. J. Klingenberg. Material parameters for electrostriction. *Journal of Applied Physics*, 80(8):4566–4572, Oct. 1996.

[135] O. A. Smiseth, H. Torp, A. Opdahl, K. H. Haugaa, and S. Urheim. Myocardial strain imaging: how useful is it in clinical decision making? *European Heart Journal*, 37(15):1196–1207, Apr. 2016.

[136] W. Smith. The role of piezocomposites in ultrasonic transducers. In *Proceedings., IEEE Ultrasonics Symposium*, pages 755–766, Montreal, Que., Canada, 1989. IEEE.

[137] E. Snelson and Z. Ghahramani. Sparse gaussian processes using pseudo-inputs. In Y. Weiss, B. Schölkopf, and J. C. Platt, editors, *Advances in Neural Information Processing Systems 18*, pages 1257–1264. MIT Press, 2006.

[138] J. Snoek, H. Larochelle, and R. P. Adams. Practical Bayesian Optimization of Machine Learning Algorithms. *arXiv:1206.2944*, Aug. 2012.

[139] I. Sobol. Uniformly distributed sequences with an additional uniform property. *USSR Computational Mathematics and Mathematical Physics*, 16(5):236–242, Jan. 1976.

[140] N. Srinivas, A. Krause, S. M. Kakade, and M. Seeger. Gaussian Process Optimization in the Bandit Setting: No Regret and Experimental Design. *IEEE Transactions on Information Theory*, 58(5):3250–3265, May 2012. arXiv: 0912.3995.

[141] O. Stohlman and S. Pellegrino. Shape Accuracy of a Joint-Dominated Deployable Mast. In *51st AIAA/ASME/ASCE/AHS/ASC Structures, Structural Dynamics, and Materials Conference*, Orlando, Florida, Apr. 2010. American Institute of Aeronautics and Astronautics.

[142] A. Stoll, M. Mayer, G. J. Monkman, and M. Shamonin. Evaluation of highly compliant magneto-active elastomers with colossal magnetorheological response. *Journal of Applied Polymer Science*, 131(2), Jan. 2014.

[143] L. Sun, W. M. Huang, C. C. Wang, Y. Zhao, Z. Ding, and H. Purnawali. Optimization of the shape memory effect in shape memory polymers. *Journal of Polymer Science Part A: Polymer Chemistry*, 49(16):3574–3581, Aug. 2011.

[144] Y. Tadesse. Electroactive polymer and shape memory alloy actuators in biomimetics and humanoids. San Diego, California, USA, Apr. 2013.

[145] S. Takahashi, A. Ochi, M. Yonezawa, T. Yano, T. Hamatsuki, and I. Fukui. Internal electrode piezoelectric ceramic actuator. *Ferroelectrics*, 50(1):181–190, Nov. 1983.

[146] T. Tancogne-Dejean and D. Mohr. Stiffness and specific energy absorption of additively-manufactured metallic BCC metamaterials composed of tapered beams. *International Journal of Mechanical Sciences*, 141:101–116, June 2018.

[147] P. A. Tipler and G. Mosca. *Physics for scientists and engineers: standard*. W.H. Freeman, New York, NY, 6th ed edition, 2008.

[148] M. Titsias. Variational learning of inducing variables in sparse gaussian processes. In D. van Dyk and M. Welling, editors, *Proceedings of the Twelth International Conference on Artificial Intelligence and Statistics*, volume 5 of *Proceedings of Machine Learning Research*, pages 567–574, Hilton Clearwater Beach Resort, Clearwater Beach, Florida USA, 16–18 Apr 2009. PMLR.

[149] P. Tozzi, A. Michalis, D. Hayoz, D. Locca, and L. K. von Segesser. Artificial muscle for end-stage heart failure. *ASAIO Journal*, page 1, Feb. 2012.

[150] D. R. Trumble, W. E. McGregor, R. C. P. Kerckhoffs, and L. K. Waldman. Cardiac assist with a twist: Apical torsion as a means to improve failing heart function. *Journal of Biomechanical Engineering*, 133(10), Oct. 2011.

[151] J. V. Tu. Advantages and disadvantages of using artificial neural networks versus logistic regression for predicting medical outcomes. *Journal of Clinical Epidemiology*, 49(11):1225–1231, Nov. 1996.

[152] K. Uchino. Piezoelectric composite materials. In *Advanced Piezoelectric Materials*, pages 318–346. Elsevier, 2010.

[153] K. Uchino. The Development of Piezoelectric Materials and the New Perspective. In *Advanced Piezoelectric Materials*, pages 1–92. Elsevier, 2017.

[154] P. Virtanen, R. Gommers, T. E. Oliphant, M. Haberland, T. Reddy, D. Cournapeau, E. Burovski, P. Peterson, W. Weckesser, J. Bright, S. J. van der Walt, M. Brett, J. Wilson, K. J. Millman, N. Mayorov, A. R. J. Nelson, E. Jones, R. Kern, E. Larson, C. J. Carey, İ. Polat, Y. Feng, E. W. Moore, J. VanderPlas, D. Laxalde, J. Perktold, R. Cimrman, I. Henriksen, E. A. Quintero, C. R. Harris, A. M. Archibald, A. H. Ribeiro, F. Pedregosa, P. van Mulbregt, and SciPy 1.0 Contributors. SciPy 1.0: Fundamental Algorithms for Scientific Computing in Python. *Nature Methods*, 17:261–272, 2020.

[155] T. Wang, M. Farajollahi, Y. S. Choi, I.-T. Lin, J. E. Marshall, N. M. Thompson, S. Kar-Narayan, J. D. W. Madden, and S. K. Smoukov. Electroactive polymers for sensing. *Interface Focus*, 6(4):20160026, Aug. 2016.

[156] Z. Wang and S. Jegelka. Max-value Entropy Search for Efficient Bayesian Optimization. *arXiv:1703.01968*, Jan. 2018.

[157] Y.-j. Wei, N. Silikas, Z.-t. Zhang, and D. C. Watts. The relationship between cyclic hygroscopic dimensional changes and water sorption/desorption of self-adhering and new resin-matrix composites. *Dental Materials*, 29(9):e218–e226, Sept. 2013.

[158] Y. J. Weitsman. Effects of Fluids on Polymeric Composites—A Review. In *Comprehensive Composite Materials*, pages 369–401. Elsevier, 2000.

[159] WHO. Cardiovascular Diseases, May 2017.

[160] M. Wissler and E. Mazza. Electromechanical coupling in dielectric elastomer actuators. *Sensors and Actuators A: Physical*, 138(2):384–393, Aug. 2007.

[161] C. Wujun, L. Yaozhi, F. Gongyi, G. Jinghai, and D. Shilin. Design Conception and Deployment Simulation for a Highly Synchronized Extendable/Retractable Space Mast. *International Journal of Space Structures*, 16(4):261–269, Dec. 2001.

[162] X. Xia, A. Afshar, H. Yang, C. M. Portela, D. M. Kochmann, C. V. Di Leo, and J. R. Greer. Electrochemically reconfigurable architected materials. *Nature*, 573(7773):205–213, Sept. 2019.

[163] F. Xie, L. Huang, Y. Liu, and J. Leng. Modified shape memory cyanate polymers with a wide range of high glass transition temperatures. page 834210, San Diego, California, Apr. 2012.

[164] G. Yang, G. Yao, W. Ren, G. Akhras, J. P. Szabo, and B. K. Mukherjee. The strain response of silicone dielectric elastomer actuators. page 134, San Diego, CA, May 2005.

[165] T. Yingchoncharoen, S. Agarwal, Z. B. Popović, and T. H. Marwick. Normal Ranges of Left Ventricular Strain: A Meta-Analysis. *Journal of the American Society of Echocardiography*, 26(2):185–191, Feb. 2013.

[166] N. Yogamalar, S. Kalpana, V. Senthil, and A. Chithambararaj. Ferroelectrics for photocatalysis. In *Multifunctional Photocatalytic Materials for Energy*, pages 307–324. Elsevier, 2018.

[167] A. A. Young and B. R. Cowan. Evaluation of left ventricular torsion by cardiovascular magnetic resonance. *Journal of Cardiovascular Magnetic Resonance*, 14(1):49, Dec. 2012.

[168] X. Yu, J. Zhou, H. Liang, Z. Jiang, and L. Wu. Mechanical metamaterials associated with stiffness, rigidity and compressibility: A brief review. *Progress in Materials Science*, 94:114–173, May 2018.

[169] X. Yuan, S. Changgeng, G. Yan, and Z. Zhenghong. Application review of dielectric electroactive polymers (DEAPs) and piezoelectric materials for vibration energy harvesting. *Journal of Physics: Conference Series*, Sept. 2016.

[170] Q. M. Zhang. Giant Electrostriction and Relaxor Ferroelectric Behavior in Electron-Irradiated Poly(vinylidene fluoride-trifluoroethylene) Copolymer. *Science*, (5372):2101–2104, June 1998.

[171] Z. Zhang, L. Liu, J. Fan, K. Yu, Y. Liu, L. Shi, and J. Leng. New silicone dielectric elastomers with a high dielectric constant. San Diego, California, Mar. 2008.

[172] C. Zhu, R. H. Byrd, P. Lu, and J. Nocedal. Algorithm 778: L-BFGS-b. *ACM Transactions on Mathematical Software*, 23(4):550–560, Dec. 1997.

A

SUPPLEMENTARY MACHINE LEARNING DATA

This appendix contains supplementary figures which help with understanding of the model inaccuracies as well as additional space design sections not included in the main report.

A

A.1. MODEL ACCURACY

As mentioned before each of the machine learning models presented a different accuracy and mean errors, all of which were deemed appropriate for the conceptual analysis. In the case of the longitudinal strain and radial deformation models the mean squared error came mostly from multiple insignificant imprecisions in estimation of the outcomes (please see fig. A.1 and A.2) while in the case of the rotation model some significant mistakes were spotted as shown in fig. A.3.

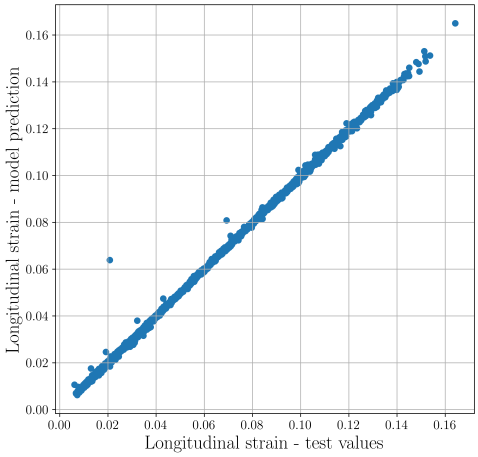

Figure A.1: Predicted vs actual value graph of longitudinal strain at the tip of the longerons

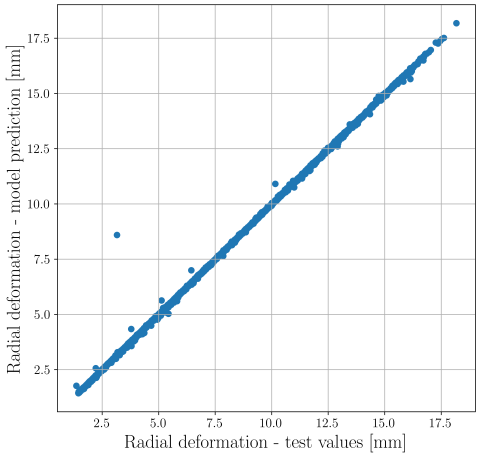

Figure A.2: Predicted vs actual value graph of radial deformation at the tip of the longerons

Both radial deformation and longitudinal strain model prediction vs actual value comparisons show missing values near the right top corner which corresponds to the highest values of both deformations. This is most likely a result of too scarce Sobol sampling, however such high strains belong to the range of infeasible ones because of longeron clashing effect. Therefore lack of coverage of this design space piece does not affect the results to a significant extent.

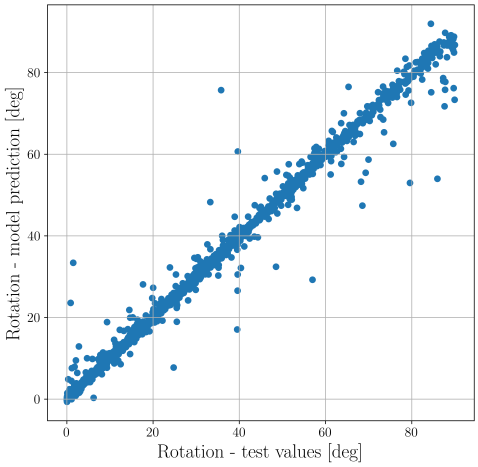

Figure A.3: Predicted vs actual value graph of rotation between the apex and base of the structure

The mispredictions in the rotation model do not seem to be bound to any region of the design space and appear to be just a few random mistakes which could be fixed by addition of more datapoints to the base and/or optimization of neural network hyperparameters.

A

A.2. SUPPLEMENTARY DESIGN SPACE PROJECTIONS

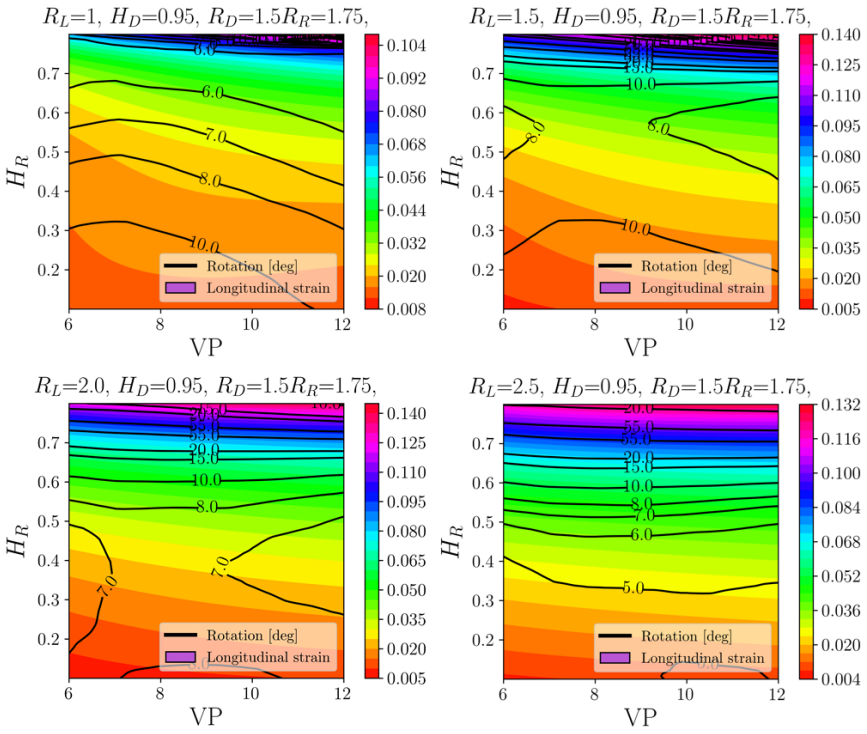

Figure A.4: Mean longitudinal strain and rotation values presented as functions of number of longerons, ring height and longeron radius

Figure A.5 represents the sections of design space which show the region close to optimal as predicted with Bayesian optimization. It can be seen that with relative diagonal mounting height between 0.9 and 1 as well as 7 longerons the ring can be mounted lower at around 65% of the structure's height instead of 80% and with thick longerons and low ring radius longitudinal strains close to optimal (0.067−0.7) can be attained . Such a configuration could be utilized if the sturdiness of the basic one is deemed too low.

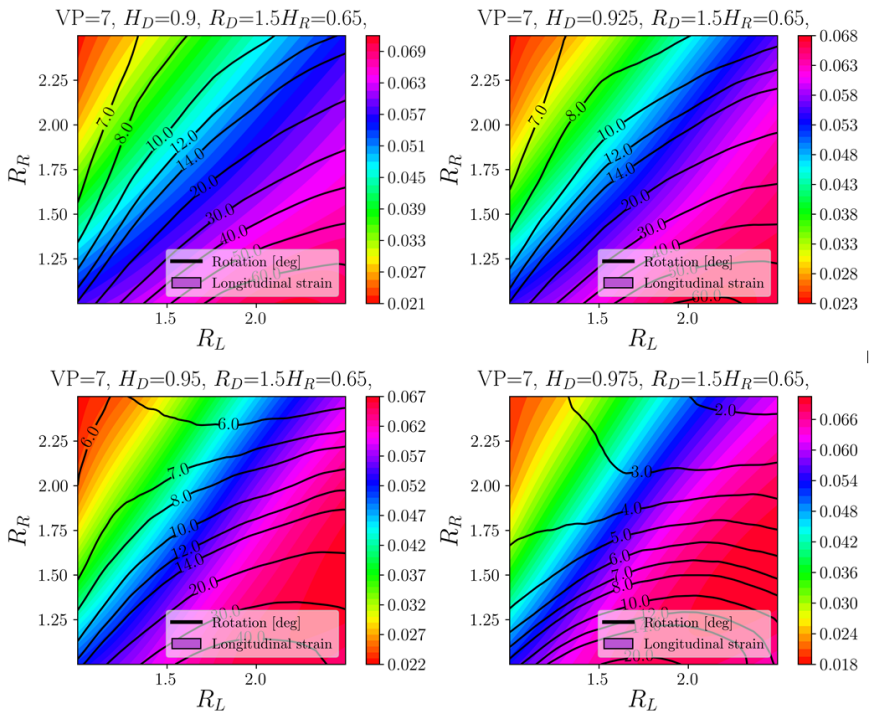

Figure A.5: Mean longitudinal strain and rotation values presented as functions of ring radius, diagonal height and longeron radius

B

CONVERGENCE AND FULL OPTIMIZATION MODEL

B.1. 7 PARAMETER OPTIMIZATION

This appendix contains parameters and results of the all - parameter optimization process. Table B.1 contains the most optimal parameters and figure B.1 shows the geometry visualization. Table B.2 presents the achievable values which are only insignificantly higher than those achieved with 4 parameter optimization in the case of longitudinal strain (7.4% instead of 7.2%) at local strain required being 8.24% instead of 7.2% and the rotation being 72°. This leads to the objective function being only 0.01 mm lower which is not justified by the higher required local strain and additional unnecessary rotation.

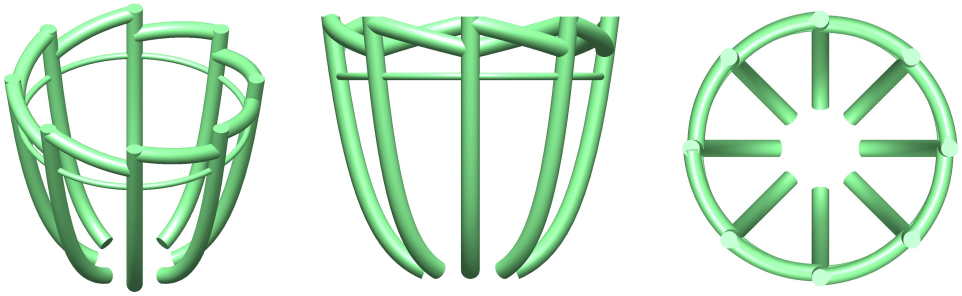

(a) Projected view (b) Side view (c) Top view

Figure B.1: CAD model of the structure optimized with all parameters as described in table B.1

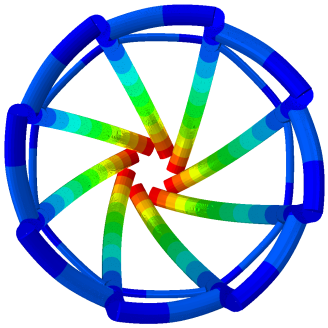

(a) Top view

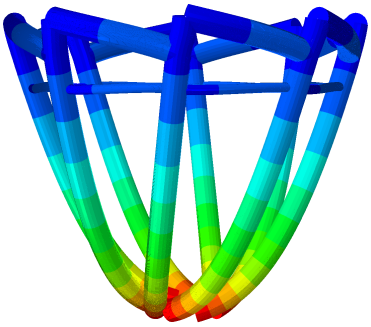

(b) Side view

Figure B.2: Visualisation of deformed optimal configuration obtained with 7 parameter Bayesian optimization. The geometry is described in table B.1.

Table B.1: Quantities of interest and required local strain for the all - parameter optimization

Parameter	R_L	$Polygon$	H_D	R_D	H_R	R_R
Value	2.5 mm	8	0.9	2.5 mm	0.8	1.0 mm

Table B.2: Parameters of the fully optimized configuration

Quantity	Long strain	Local strain	Rotation
Value	7.4%	8.24%	72 deg

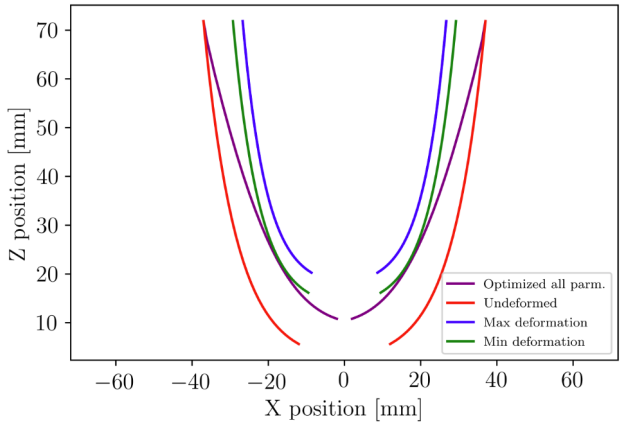

Figure B.3: X-Z plane section of the design optimized with 7 parameters

As shown in fig. B.2 this configuration results in slight clashing longerons which would require their trimming at the ends in order to avoid mechanical damage and unpredicted deformations. This design, however may be slightly sturdier than the one with 7 longerons described in chapter 4 due to thicker diagonals. On the other hand this might be an issue due to thicker joints and tests should be performed to quantify the deviation of such design from the theoretical predictions.

Above figure B.3 presents the section of the configuration which is insignificantly different from the one optimized with just 4 parameters. It suffers from the same issues as the other geometry and does not provide tangible improvements which would justify the higher required local strains/magnetic fields.

B.2. CONVERGENCE

Interestingly, the convergence of the optimization process based on 7 parameters instead of one with just 4 with the rest of them being fixed happened faster, around the 50th iteration. In the case of the optimization process with regards only to ring height and radius as well as longeron radius and local strain it took around 200 iterations to reach the near optimal value. Such can partially be explained with difference in starting points or difficulty in finding optimum within the design space with some of the parameters being fixed. Optimization of the configuration with contractible longerons approaches the optimum after 800^{th} iteration which seems to be a result of a wider range of attainable objective function values. The achieved value of $4.6mm$ is limited by the extent to which the longerons can contract.

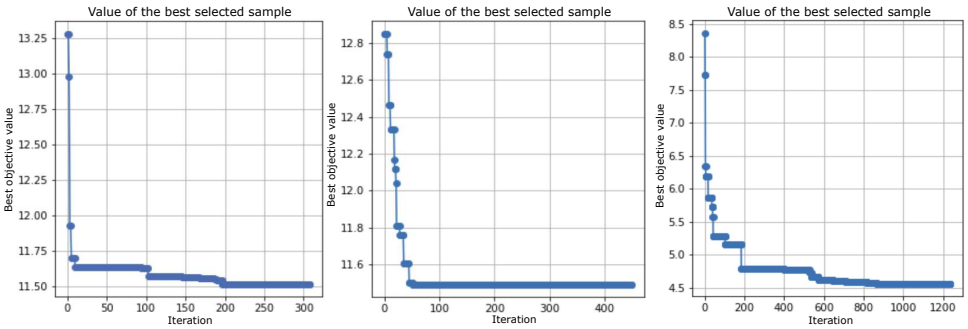

(a) 4-parameter optimization convergence

(b) 7-parameter optimization convergence

(c) Contractible longeron configuration optimization convergence

Figure B.4: Convergence plots for optimization Approaches 1 and 2 with 4 and 7 parameters respectively as well as the one for configuration with contractible longerons